# On the Radon transform of sampled functions

A thesis presented

by

Manuela Alexandra S. Pereira Vasconcelos

to

The Division of Engineering and Applied Sciences
in partial fulfillment of the requirements
for the degree of

Doctor of Philosophy
in the subject of

Engineering Sciences

Harvard University
Cambridge, Massachusetts

June 2003

**Manuela Alexandra S. Pereira Vasconcelos**

**Prof. Roger W. Brockett**

## On the Radon transform of sampled functions

### Abstract

We address the characterization of the Radon transform of piecewise constant functions on a pixel lattice. A closed-form expression is derived for the Radon transform of any pixelated function and the pixelated line analyzed in detail. The latter is shown to have three properties that lead to a Radon transform substantially different from that of the idealized line: bounded support, non-zero width, and pixelization. Bounded support results in two sets (the admissible and the intersecting set) that fully characterize the support of the range function, while non-zero width shapes its amplitude to be continuously decaying, from the maximum value, at a rate $1/\sin(\Delta\theta)$ (where $\Delta\theta$ is the distance to the angle associated with the maximum).

These observations enable the derivation of the narrow strip approximation (NSA) to the Radon transform of the pixelated line. This is an upper-bound on the true Radon transform which is shown to be tight, in the sense that inequalities become equalities, when the ratio between pixel and image size goes to zero. The NSA is a simple model of the range function that, unlike the frequently used Dirac delta, accounts for the three properties mentioned above. In result, it allows both theoretical and algorithmic advances to the problem of line detection. On the theoretical side, it is shown that the traditional strategy of line detection by thresholding is fundamentally flawed, as it is intrinsically unable to reach accurate parameter estimates for spatially localized lines. On the algorithmic side, an analysis-by-synthesis line detection algorithm is proposed and shown to be substantially more accurate than thresholding methods.

Finally, we characterize various statistical properties of the range function: its probability density function, mean, variance, and sample mean. Once again this leads to advances in both theory and algorithms: 1) a proof of existence of a fundamental law that characterizes the amplitudes of the Radon transform, and 2) an optimal, in the minimum probability of error sense, algorithm for estimating the number of lines in an image.

*To my mother and in memory of my father.*

# Acknowledgments

I would like to thank several people that, in different ways, made this work possible.

My advisor, Prof. Roger Brockett. His passion for science, strong belief in rigor and first principles, and constant challenges have been a never ending source of awe and inspiration. It is rarely in life that one has the opportunity to closely interact with, and learn from, deep thinkers. I truly feel fortunate to have had such an opportunity.

The members of my doctoral committee, Profs. Aleksander Kavcic, Vahid Tarokh, and Navin Khaneja have provided insightful comments that have improved the quality of this manuscript. Navin and I go a long way together, since the time we both started at Harvard. More than a colleague, he has been a true friend that I have learned to respect and admire.

The fellow and former members of the Harvard Robotics Lab have created an environment that was always fun, friendly, and a source of numerous brainstorming sessions that helped mature the main ideas of this thesis. I would specially like to acknowledge the friendship and support of Hongyi Li, and the early encouragement from Nanayaa Twum-Danso, Walter Baker, Dimitrios Hristu, and Kristi Morgansen. There are of course many more names, too many to distinguish individually. So I thank all of them for six great years: Tammy Hepps, Mark Hoefer, Stan Jurga, Sam Pfister, Magnus Egerstedt, Michael Brody, Andrew Damons, Benjamin Peirce, Michael McElroy, Jian Zou, Su Ying Quek, Jason Adaska, Mohamed Ali Belabbas, Drew Carlson, Abdol-Reza Mansouri, and Mark Byrd. Finally, none of this would have worked without the friendship of Kathleen Lafrance.

Outside HRL, there are several people that I was lucky to meet at Harvard: Carolann Brockett, Soundouss Bouhia, Minh Nguyen, and Susan Wieczorek; as well as a great community of Cambridge/Boston friends: Paulo Ferreira, José Camões, Luiz Quaresma, Inês Byrne and Miguel Castro, Inês Sousa, Francisco Veloso, Júlia Allen and Luís Miguel Silveira, Jorge Gonçalves, José Tavares, Hermínio Rico, Rodrigo Miragaia, Sara Maia, Tiago Ribeiro, José Duarte, Sofia Berto and Miguel Villas-Boas, Ricardo Schiappa, Francisca Leite, José Carlos Monteiro, Ana Canas da Silva, Cláudia Drumond, João Paulo Ferreira,

Maggie and José Tribolet, David August and Anne Smith, Sarah Wilkenson and Yuri Ivanov.

My friends in Portugal for the great times when I go back: Paula Morais and Miguel Barroso, Cristina Grande, Sílvia and Paula Barrias, Teresa and Joana Andrade, Rita Mântua and Paulo Guedes, Nair Taveira, José Manuel Cabral, Pedro Cardoso, Isabel Freitas, and my goddaughter Joana.

Being away from the people that I care most for was the hardest challenge of graduate school. They were, nevertheless, always present. I feel blessed to have been raised by two people that relentlessly inspired me to always pursue my dreams. My mother is a living example of courage, determination, kindness, and unconditional love for her kids. Mommy and Daddy, this thesis is dedicated to you! My sister Terezinha and brother André together with Paulo, Afonso, and Terezinha have always had a special place in my heart, and I truly miss the joy of being with them everyday.

During my graduate studies, I was lucky enough to see my family grow by a number of exceptional people. To the Vasconcelos family: Assunção and Manuel, Pedro, Rita and Catarina, Ricardo, and Verinha, thanks for the love and support, and whole heartily embracing me in the family.

My beloved daughters, Francisca and Benedita, whose smile at the end of the day always made the hardships of theorem proving seem so irrelevant. There are moments in life where life itself turns for the better, and I was lucky enough to have two.

My husband, Nuno, for his unconditional support, caring, and love. Nuno, thanks for always believing that I could do it. There is no way I could have done it without you! I am really fortunate to have shared the two moments above with you!

This work was supported by subcontract from Brown University,'Vision Strategies and ATR Performance: a Mathematical Statistical Formulation and Critique', 655 21255, under prime of ATR ARO MURI DAAH04-96-BAA5.

# Contents

# List of Figures

# List of Tables

# Chapter 1

# Introduction

The ability to build machines with perceptual abilities that mimic those of humans has been a long-standing goal in science and in engineering. One critical problem for the attainment of this goal is the development of a theory for computer vision that will enable machines to understand visual stimulae, e.g. a video sequence produced by a digital camera, a still image taken from an airplane, or a collection of images covering different perspectives of a scene in the natural world. The potential applications are numerous, and the impact would be significant. In fact, vision systems are a crucial requirement for many problems in robotics (Blake and Yuille (1992)), advanced surveillance systems (Kumar et al. (1995)), the management of large image archives (Smeulders et al. (2000)), computer graphics (Heeger and Bergen (1995)), etc. In recent decades, significant progress has been achieved in some sub-areas of the vision problem. The most notable is probably a solid understanding of the geometric aspects of image capture (Faugeras (1993); Hartley and Zisserman (2000)), i.e. the projection of a scene in the 3D world to the 2D image plane. Besides geometry, areas such as object recognition (Ullman (2000); Hallinam et al. (1999)), or the recovery of 3D structure from various cues (Tomasi and Kanade (1992); Soatto and Brockett (1998)) have also seen significant advances. However, it is uncontroversial to say that a unified and coherent theory for vision is, to date, not available.

One source of difficulty is the fact that vision is not always addressed in a mathematically principled way. In fact, it is uncommon to find, in the vision literature, provable guarantees that vision algorithms actually accomplish what they were designed to do. When provided, such guarantees only apply to components of the problem and are commonly interspersed with heuristics at implementation time. Due to this, most algorithms tend to be applicable

in a few, narrow, domains and are usually not very robust. On the other hand, most mathematical efforts that address vision problems have been carried out under hypotheses that are too distant from reality to result in algorithms of practical value. This is, in part, a consequence of the difficulty of the vision problem and, in part, a consequence of the lack of mathematical appeal of some of the issues that have to be addressed to make vision practical. The problem addressed in this thesis, the detection of geometric structures in images, is a good example of the set of problem which fall in the gap between 1) what is reasonably understood through practice and experimentation but lacks a solid theoretical foundation, and 2) the remarkably elegant mathematical concepts that provide deep understanding but disregard components of great practical significance.

In the vision literature, the standard algorithm for detecting geometric structures is the so-called Hough transform (HOUGH (1962); ILLINGWORTH AND KITTLER (1988)): a heuristic which consists of 1) fitting all the possible parameterizations of the structure of interest to the image, 2) counting the number of pixels where the fit is accurate, and 3) declaring the parameterization with more votes the winner. Despite a lack of strong mathematical foundation, the Hough transform is one of the most successful algorithms for problems such as line detection and widely used in practical applications. There are, however, many aspects in which its successful application is more of an art form than science. For example, it is usually quite difficult to prevent false positives when the target structures have significantly different sizes. To overcome this problem, the Hough transform is usually combined with other heuristic steps, normally involving various image processing operators, to the point where any serious characterization of which is doing what becomes intractable.

Mathematically, the Hough transform is an approximation of the Radon transform, first introduced by Johann Radon in (RADON (1917)). Unlike the Hough transform, the Radon transform is a formally studied mathematical construct whose properties are well understood (HELGASON (1999)). It has assumed an important role in mathematics in recent years because of various imaging modalities that, in effect, measure a Radon transform (DEANS (1983)). In computer vision, the situation is something of the reverse. The sensor gives a function on the plane, or a subset of the plane, and the Radon transform is used as a detector of lines or line segments. Its suitability for this task is uniquely determined by the fact that an idealized line is mapped into an impulse plus some "background" function. The crucial practical limitation here is, however, the word 'idealized'. In the real world, images are acquired by digital sensors and the continuous light surface that impinges of

these sensors is sampled according to a pre-defined pixel lattice. It follows that the idealized concept of a line as an infinite 1D subspace of the 2D plane is replaced by the concept of a line as a finite collection of pixels that have non-vanishing support.

To a first-order approximation, it should be reasonable to expect that, when the pixel size is much smaller than the line length, the idealized line would provide a good model for the true pixel collection. Under this model, simply thresholding the amplitude of the range function of the Radon transform would be sufficient to detect lines. However, when this argument is tested on real imagery, it does not take long to realize that the Radon transform of the idealized model is a very poor approximation to the Radon transform of the pixelated line. This somewhat surprising observation casts doubt on the applicability of most known theoretical results on the Radon transform to computer vision problems. This is the problem addressed by this thesis, whose central goal is to provide a rigorous understanding of how pixelization affects the Radon transform. Of course, once such a characterization is available, it becomes significantly easier to criticize the existing strategies for line detection and develop better algorithms. While the main goal of the thesis is not the problem of line detection per se, various new insights are derived on the performance of current solutions and some new solutions are proposed.

The thesis includes various novel contributions. In chapter 2, we start by discussing the Radon transform and review some previously known aspects, such as its basic properties, and the range functions for various canonical structures including the line and the pixel. We also introduce two structures that are usually not found in the literature - the strip, which is a line with positive width, and the pixelated function - and derive their Radon transforms. In chapter 3, we introduce the pixel lattice, formalize the concept of a pixelated line, and derive an exact expression for its Radon transform. This happens to be quite different from the impulse plus "background" function associated with the idealized line model. Instead, the Radon transform of the pixelated line is a convolution of many elementary functions, and continuously decays (as a function of line angle) from its maximum value. It is then shown that, under some simplifying assumptions, the Hough transform of the line is an approximation to this expression. Unfortunately, this approximation is not particularly insightful and does not lend itself to simpler analytical manipulation than the true expression. It is therefore not clear that there is any advantage in studying the Hough transform and we do not do so in the remainder of the thesis.

Instead, chapter 4 addresses one issue that has significant impact on the shape of the Radon transform: the finite nature of pixel lattices. While on $\mathbb{R}^2$ two non-parallel lines

will always intersect, the same does not hold on a bounded subset of $\mathbb{R}^2$. Hence, the "background" function of unbounded support associated with the idealized line becomes a function supported on the set of all lines that it intersects. We denote this set as the intersecting set of the line, and study its properties. It happens that this set can also be characterized analytically and, unlike the amplitude of the Radon transform, is not significantly affected by pixelization. In fact, we show that the intersecting set of the line, the strip, and the pixelated line are all very similar. This is a result of practical significance since the precise characterization of the intersecting set of the pixelated line appears to be quite difficult. It also completes the rigorous characterization of a series of models that can be used to approximate the (computationally intractable) Radon transform of the pixelated line.

In chapter 5, we start to consider the practical implications of the theoretical characterization of the previous chapters. We create a taxonomy of models that approximate the pixelated line and which successively account for more of the features that characterize it (bounded support, non-zero width, and pixelization). It is shown that these successive approximations provide an analytical justification for several variations on the widely used strategy of line detection by thresholding of the Radon amplitude. More importantly, this exercise provides 1) a precise understanding of when the assumption that pixels have point-support is acceptable and 2) proofs that this assumption can lead to significant errors (false positives) under the standard thresholding strategy. The main result is a theorem akin to the uncertainty principle of Fourier analysis (where simultaneous localization in time and space are impossible) for the size of the region of support of the Radon transform: the uncertainty of line orientation estimates recovered by thresholding is lower bounded by a quantity inversely proportional to the window size. Since small windows are necessary to localize the recovered lines, this means that the thresholding strategy imposes an intrinsic trade-off between false positives and spatial localization.

This limitation motivates a search for a different line detection strategy. Building on the results of the previous chapters, we show that the Radon transform of the pixelated line is tightly bounded by a function that 1) is constant in a small neighborhood of the peak value, 2) has a simple dependence on the line angle in the remainder of the intersecting set, and 3) is zero elsewhere. This leads to another interesting contribution of the thesis: a new parametric model for the Radon transform of a pixelated line that is quite easy to manipulate, both analytically and computationally. We use this model as the basis for a new analysis-by-synthesis procedure for line detection: given the number of pixelated lines

in the image, the parameters of the longest line are determined by finding the largest value of the Radon amplitude (analysis step), the parametric estimate of the associated Radon transform is synthesized (synthesis step), subtracted from the original Radon transform, and the process iterated. The resulting algorithm is extremely fast, involves no magic numbers (other than the number of lines in the image), and performs remarkably well when compared to the standard thresholding strategies. This is due to its ability to completely discount the Radon transform of all previously detected lines at each new detection step.

In chapter 6, we turn our attention to the statistical characterization of the Radon transform. We assume a simple measure, or prior, on the space of image lines which, in turn, induces a measure on the amplitude of the range function of the Radon transform. Closed-form expressions are derived for the probability density function of the latter, as well as various statistics including the mean, variance, and the conditional likelihood function for its sample mean, given the number of pixelated lines. This leads to another interesting contribution of the thesis, a proof of existence for a statistical law that governs the amplitude of the Radon transform. The existence of such a law, for various transformations commonly used in vision, has been the subject of extensive debate in the recent literature (Bell and Sejnowski (1995); Olshausen and Field (1996); Huang and Mumford (1999); Portilla and Simoncelli (2000); Grenander and Srivastava (2001)). We present a derivation from first principles that, to the best of our knowledge, was previously unavailable for the Radon transform.

This statistical law also happens to have interesting practical ramifications. In particular, we show that 1) it depends only on a set parameters that can be pre-computed, and 2) leads to a simple linear dependence of the first- and second-order statistics of the range function on these parameters. In the context of applications, this ability to pre-compute all parameters implies very efficient statistical inference procedures. We demonstrate this property by deriving an optimal algorithm, in the minimum probability of error sense, for the estimation of the number of lines in a pixelated edge map that has very low computational complexity. This algorithm enables the application of analysis-by-synthesis line detection analysis to local image neighborhoods. The result of integrating the two algorithms is a procedure capable of accurately detecting lines without compromise of spatial localization. We provide various examples of spatially localized line detection on challenging natural scenes.

# Chapter 2

# The Radon transform

In this chapter, we discuss the Radon transform and derive some of its properties. Even though the Radon transform has previously been applied to various image processing tasks, it is still not well understood how it is affected by pixelization. The problem is that images are not continuous functions, but piecewise constant functions, since image intensity is constant within each image pixel. By assuming that pixels have infinitesimal area, it is possible to think of images as continuous functions but it is expected that this will introduce errors. However, there has not been, to date, an effort to characterize rigorously what these errors may be.

In this chapter, we begin to address this problem by studying the effects of pixelization on the Radon transform. After deriving some of the basic properties of the latter, we derive the Radon transform of a sequence of models of increasing complexity, each introducing an extra feature, leading to the pixelated function. We start by the line which, having infinite length and zero width, is the simplest abstraction for the pixelated line. We then introduce the line segment, the restriction of the line to a bounded subset of the plane and, therefore, a more realistic model for images. Next, we consider lines with non-vanishing width, that we refer to as strips. The extension to the pixel, which is basically a strip of finite length, is then shown to be quite simple. The pixelated function is next defined as a weighted sum of pixels, and shown to be equivalent to the convolution of the pixel indicator function with a train of delta functions. Making use of the basic properties of the Radon transform, it is then straightforward to show that the Radon transform of the pixelated function is a sum of many modulations of the Radon transform of the pixel.

The study of this sequence of models is interesting in two ways. First, because it leads to a closed-form expression to the Radon transform of the pixelated function. Second, and

more important for the remainder of this thesis, because it provides insight on how each of the different features of the pixelated line (non-zero width, bounded support, pixelization) affects its Radon transform. This sets up a foundation for the following chapters.

## 2.1 The Radon transform

We start by establishing our notation. If $A$ is a finite set, we denote its cardinality by $|A|$. If $A$ and $B$ are two finite sets with cardinality $|A|$ and $|B|$, respectively, there are $|B|^{|A|}$ distinct maps from $A$ into $B$. As is standard in mathematics, we denote the set of all such maps by $B^A$. We will use this exponential notation even when we deal with infinite sets.

A line $\boldsymbol{l}$ in $\mathbb{R}^2$ can be parameterized by

$$b = \boldsymbol{\xi}(\theta) \cdot \boldsymbol{x} = x \cos\theta + y \sin\theta, \tag{2.1}$$

where $\boldsymbol{x} = (x, y) \in \mathbb{R}^2$, $b$ is the distance to the origin along the line perpendicular to $\boldsymbol{l}$, and $\boldsymbol{\xi}(\theta) = (\cos\theta, \sin\theta)$ is a unit vector indicating the direction of this line, as is illustrated in Figure 2.1. For brevity, we will refer to $\boldsymbol{\xi}(\theta)$ as $\boldsymbol{\xi}$, the argument $\theta$ being ommited unless otherwise explicitely specified. Furthermore, due to this one to one relationship between $\boldsymbol{\xi}$ and $\theta$, we will use the two indiscriminately, e.g. we will refer to a line as both $\boldsymbol{l} = (b, \boldsymbol{\xi}) \in \mathbb{R} \times \mathbb{S}$ and $\boldsymbol{l} = (b, \theta) \in \mathbb{R} \times [0, \pi]$.

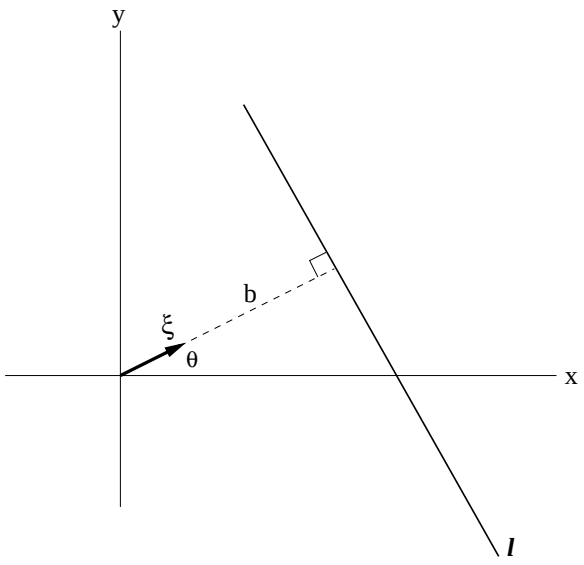


Figure 2.1: Parameterization of a line $\boldsymbol{l} = (b, \boldsymbol{\xi})$.

**Definition 2.1.** Following Radon (RADON (1917)), the *2D continuous Radon transform* is a kernel transformation defined by

$$\mathcal{R} : \mathbb{R}^{\mathbb{R}^2} \to \mathbb{R}^{\mathbb{R}\times\mathbb{S}}$$

$$\mathcal{R}[f](b, \boldsymbol{\xi}) = \int_{\mathbb{R}^2} f(\boldsymbol{x})\delta(b - \boldsymbol{\xi}\cdot\boldsymbol{x})d\boldsymbol{x}, \tag{2.2}$$

where $f$ is a function defined in some domain of $\mathbb{R}^2$.

It can be shown (DEANS (1983); JAIN (1989)) that the properties listed in Table 2.1 follow from this definition.

| | |
|---|---|
| **linearity** | $\mathcal{R}[c_1 f + c_2 g](b, \boldsymbol{\xi}) = c_1\mathcal{R}[f](b, \boldsymbol{\xi}) + c_2\mathcal{R}[g](b, \boldsymbol{\xi})$, where $c_1$, $c_2$ are constants. |
| **linear transformation** | $\mathcal{R}[f(\mathbf{y})](b, \boldsymbol{\xi}) = \frac{\lvert\det \mathbf{A}\rvert}{\lVert\mathbf{A}^T\boldsymbol{\xi}\rVert}\mathcal{R}[f(\boldsymbol{x})]\left(\frac{b}{\lVert\mathbf{A}^T\boldsymbol{\xi}\rVert}, \frac{\mathbf{A}^T\boldsymbol{\xi}}{\lVert\mathbf{A}^T\boldsymbol{\xi}\rVert}\right)$, where $\mathbf{y} = \mathbf{A}^{-1}\boldsymbol{x}$. |
| **shifting** | $\mathcal{R}[f(\boldsymbol{x} - \mathbf{a})](b, \boldsymbol{\xi}) = \mathcal{R}[f(\boldsymbol{x})](b - \boldsymbol{\xi}\cdot\mathbf{a}, \boldsymbol{\xi})$ |
| **convolution** | $\mathcal{R}[f * g](b, \boldsymbol{\xi}) = \mathcal{R}[f](b, \boldsymbol{\xi}) * \mathcal{R}[g](b, \boldsymbol{\xi})$, where $*$ denotes the convolution operator. |
| **derivatives** | $\mathcal{R}[\mathsf{L}f](b, \boldsymbol{\xi}) = \mathsf{L}\left(\xi_1\frac{\partial}{\partial d}, \xi_2\frac{\partial}{\partial d}\right)\mathcal{R}[f](b, \boldsymbol{\xi})$, where $\boldsymbol{\xi} = (\xi_1, \xi_2), \mathsf{L} = \left(\frac{\partial}{\partial x}, \frac{\partial}{\partial y}\right)$ |

Table 2.1: Some properties of the Radon transform.

**Corollary 2.1.** *The following properties hold for symmetric functions*

$$f(x, y) = f(x, -y) \quad \Leftrightarrow \quad \mathcal{R}[f(x)](b, \theta) = \mathcal{R}[f(x)](-b, \pi - \theta) \tag{2.3}$$

$$f(x, y) = f(-x, y) \quad \Leftrightarrow \quad \mathcal{R}[f(x)](b, \theta) = \mathcal{R}[f(x)](b, \pi - \theta) \tag{2.4}$$

$$f(x, y) = f(-x, -y) \quad \Leftrightarrow \quad \mathcal{R}[f(x)](b, \theta) = \mathcal{R}[f(x)](-b, \theta). \tag{2.5}$$

*Proof :* The properties are special cases of the linear transformation property. ∎

**Corollary 2.2.** *Consider the affine transformation* $\mathbf{A} = \mathbf{T_d} \circ \mathbf{M}$, *where*

$$\mathbf{M} : \mathbb{R}^2 \to \mathbb{R}^2$$

*is an invertible matrix, and*

$$\mathbf{T_d} : \mathbb{R}^2 \to \mathbb{R}^2$$

$$\mathbf{T}_{\mathbf{d}}(\boldsymbol{x}) = \boldsymbol{x} - \mathbf{d}$$

*a translation by* $\mathbf{d}$. *Then, if* $\mathbf{y} = \mathbf{A}(\boldsymbol{x}) = \mathbf{M}\boldsymbol{x} - \mathbf{d}$,

$$\mathcal{R}[f(\mathbf{y})](b, \boldsymbol{\xi}) = \frac{|\det \mathbf{M}^{-1}|}{\|(\mathbf{M}^{-1})^T \boldsymbol{\xi}\|} \mathcal{R}[f(\boldsymbol{x})] \left( \frac{b - (\mathbf{M}^{-1})^T \boldsymbol{\xi} \cdot \mathbf{d}}{\|(\mathbf{M}^{-1})^T \boldsymbol{\xi}\|}, \frac{(\mathbf{M}^{-1})^T \boldsymbol{\xi}}{\|(\mathbf{M}^{-1})^T \boldsymbol{\xi}\|} \right). \tag{2.6}$$

*In particular, when* $\mathbf{M} = \mathbf{R}_\theta$ *and* $\mathbf{R}_\theta$ *is a rotation by* $\theta$, *then*

$$\mathcal{R}[f(\mathbf{y})](b, \boldsymbol{\xi}) = \mathcal{R}[f(\boldsymbol{x})](b - \boldsymbol{\xi} \cdot \mathbf{d}, \mathbf{R}_{-\theta}^T \boldsymbol{\xi}). \tag{2.7}$$

*Proof:* Let $\mathbf{z} = \mathbf{M}\boldsymbol{x}$. By the linear transformation property of the Radon transform

$$\mathcal{R}[f(\mathbf{z})](b, \boldsymbol{\xi}) = \frac{|\det \mathbf{M}^{-1}|}{\|\boldsymbol{\zeta}\|} \mathcal{R}[f(\boldsymbol{x})] \left( \frac{b}{\|\boldsymbol{\zeta}\|}, \frac{\boldsymbol{\zeta}}{\|\boldsymbol{\zeta}\|} \right),$$

where $\boldsymbol{\zeta} = (\mathbf{M}^{-1})^T \boldsymbol{\xi}$. Since $\mathbf{y} = \mathbf{z} - \mathbf{d}$, (2.6) follows from the shifting property. When $\mathbf{M} = \mathbf{R}_\theta$, $\mathbf{R}_\theta^{-1} = \mathbf{R}_{-\theta}$, $\mathbf{R}_{-\theta}^T \boldsymbol{\xi}$ is a unit vector, and (2.7) follows. ∎

As will become evident in the following sections, it is often the case that the Radon transform of a geometric shape with arbitrary pose is significantly more complicated to compute than that of the same shape in a canonical pose (e.g. centered on the origin). When the two poses can be related by an affine transformation, Corollary 2.2 might be used to simplify the computations.

So far we have studied generic properties of the Radon transform. In the remainder of this chapter, we derive closed-form expressions for the Radon transform of functions that play an important role in line detection.

## 2.2 The Radon transform of the delta function

**Lemma 2.1.** *The Radon transform of the Dirac delta function centered at* $\boldsymbol{x} = \boldsymbol{x}_0$ *is*

$$\mathcal{R}[\delta(\boldsymbol{x} - \boldsymbol{x}_0)](b, \boldsymbol{\xi}) = \delta(b - \boldsymbol{x}_0 \cdot \boldsymbol{\xi}, \boldsymbol{\xi}). \tag{2.8}$$

*Proof:* The lemma follows from the definition of the Radon transform and the properties of the Dirac delta function, since

$$\mathcal{R}[\delta(\boldsymbol{x} - \boldsymbol{x}_0)](b, \boldsymbol{\xi}) = \int \delta(\boldsymbol{x} - \boldsymbol{x}_0)\, \delta(b - \boldsymbol{\xi} \cdot \boldsymbol{x})\, d\boldsymbol{x} = \delta(b - \boldsymbol{x}_0 \cdot \boldsymbol{\xi}, \boldsymbol{\xi}).$$

∎

## 2.3 The Radon transform of the line indicator function

**Definition 2.2.** The *support set of a line* $\boldsymbol{l} = (b, \boldsymbol{\xi})$ is the set

$$\mathcal{S}(\boldsymbol{l}) = \{\boldsymbol{x} \in \mathbb{R}^2 \,|\, b = \boldsymbol{\xi} \cdot \boldsymbol{x}\}. \tag{2.9}$$

If $\mathcal{X} \subset \mathbb{R}^2$ and $|\mathcal{S}(\boldsymbol{l}) \cap \mathcal{X}| > 1$, the line $\boldsymbol{l}$ is said to be supported by $\mathcal{X}$.

The Radon transform $\mathcal{R}[f](\boldsymbol{l})$ can be seen as the projection of $f$ onto $\mathcal{S}(\boldsymbol{l})$. The following function plays a central role in line detection.

**Definition 2.3.** The *line indicator function* of line $\boldsymbol{l}$ is the binary map

$$\mathcal{L} : \mathbb{R}^2 \to \{0, 1\}$$

$$\mathcal{L}[\boldsymbol{l}](\boldsymbol{x}) = \mathbf{1}_{\mathcal{S}(\boldsymbol{l})}(\boldsymbol{x}) = \begin{cases} 1 & \text{if } \boldsymbol{x} \in \mathcal{S}(\boldsymbol{l}), \\ 0 & \text{otherwise.} \end{cases} \tag{2.10}$$

To derive the Radon transform of $\mathcal{L}[\boldsymbol{l}](\boldsymbol{x})$, we rely on the following intermediate results.

**Lemma 2.2.** *If* $\boldsymbol{x} = (x, y)^T$, $\boldsymbol{\xi}(\theta) = (\cos\theta, \sin\theta)^T$, *and* $\mathbf{M} = [\mathbf{m}_1\ \mathbf{m_2}]$, *where* $\mathbf{m}_1$ *and* $\mathbf{m_2}$ *are two-dimensional column vectors, then*

$$\boldsymbol{\xi} \cdot \mathbf{M}\boldsymbol{x} = (\boldsymbol{\xi} \cdot \mathbf{m}_1, \boldsymbol{\xi} \cdot \mathbf{m}_2)^T \cdot \boldsymbol{x}. \tag{2.11}$$

*When* $\mathbf{M} = \mathbf{R}_{\theta_0}$, *this equation reduces to*

$$\boldsymbol{\xi} \cdot \mathbf{R}_{\theta_0}\boldsymbol{x} = \boldsymbol{\xi}(\theta - \theta_0) \cdot \boldsymbol{x}. \tag{2.12}$$

*Proof:* The first result follows from

$$\begin{aligned} \boldsymbol{\xi} \cdot \mathbf{M}\boldsymbol{x} &= \boldsymbol{\xi} \cdot (\mathbf{m}_1 x + \mathbf{m}_2 y) \\ &= \boldsymbol{\xi} \cdot \mathbf{m}_1 x + \boldsymbol{\xi} \cdot \mathbf{m}_2 y \\ &= (\boldsymbol{\xi} \cdot \mathbf{m}_1, \boldsymbol{\xi} \cdot \mathbf{m}_2)^T \cdot \boldsymbol{x}. \end{aligned}$$

If $\mathbf{M} = \mathbf{R}_{\theta_0}$, then

$$\begin{aligned} \boldsymbol{\xi} \cdot \mathbf{m}_1 &= \cos\theta\cos\theta_0 + \sin\theta\sin\theta_0 \\ &= \cos(\theta - \theta_0) \\ \boldsymbol{\xi} \cdot \mathbf{m}_2 &= -\cos\theta\sin\theta_0 + \sin\theta\cos\theta_0 \\ &= \sin(\theta - \theta_0) \end{aligned}$$

leading to the second result. ∎

**Lemma 2.3.** *If* $\boldsymbol{l} = (b_l, \theta_l)$ *and* $\boldsymbol{l}' = (0,0)$, *then*

$$\mathcal{R}\{\mathcal{L}[\boldsymbol{l}](\boldsymbol{x})\}(b,\theta) = \mathcal{R}\{\mathcal{L}[\boldsymbol{l}'](\boldsymbol{x})\}(b - b_l\cos(\theta-\theta_l), \theta-\theta_l). \tag{2.13}$$

*Proof:* Consider the linear transformation $\mathbf{A} = T_{-b_l\boldsymbol{\xi}(\theta_l)} \circ \mathbf{R}_{\theta_l}$, define $\mathbf{z} = \mathbf{A}(\boldsymbol{x})$ and note that

$$\begin{aligned}
\mathcal{L}[\boldsymbol{l}](\mathbf{z}) &= \mathcal{L}[\boldsymbol{l}](\mathbf{A}(\boldsymbol{x})) \\
&= \mathbf{1}_{\{b_l - \boldsymbol{\xi}(\theta_l)\cdot\mathbf{A}(\boldsymbol{x})=0\}}(\boldsymbol{x}) \\
&= \mathbf{1}_{\{b_l - \boldsymbol{\xi}(\theta_l)\cdot[\mathbf{R}_{\theta_l}\boldsymbol{x} + b_l\boldsymbol{\xi}(\theta_l)]=0\}}(\boldsymbol{x}) \\
&= \mathbf{1}_{\{b_l - \boldsymbol{\xi}(\theta_l)\cdot b_l\boldsymbol{\xi}(\theta_l) = \boldsymbol{\xi}(\theta_l)\cdot\mathbf{R}_{\theta_l}\boldsymbol{x}\}}(\boldsymbol{x}) \\
&= \mathbf{1}_{\{0=\boldsymbol{\xi}(0)\cdot\boldsymbol{x}\}}(\boldsymbol{x}) \\
&= \mathcal{L}[\boldsymbol{l}'](\boldsymbol{x}),
\end{aligned}$$

where we have used (2.12). It follows from Corollary 2.2 that

$$\begin{aligned}
\mathcal{R}\{\mathcal{L}'[\boldsymbol{l}](\mathbf{x})\}(b,\boldsymbol{\xi}) &= \mathcal{R}\{\mathcal{L}[\boldsymbol{l}](\mathbf{z})\}(b,\boldsymbol{\xi}) \\
&= \mathcal{R}\{\mathcal{L}[\boldsymbol{l}](\boldsymbol{x})\}(b + \boldsymbol{\xi}\cdot b_l\boldsymbol{\xi}(\theta_l), \mathbf{R}^T_{-\theta_l}\boldsymbol{\xi}) \\
&= \mathcal{R}\{\mathcal{L}[\boldsymbol{l}](\boldsymbol{x})\}(b + b_l\cos(\theta-\theta_l), \boldsymbol{\xi}(\theta+\theta_l)).
\end{aligned}$$

leading to (2.13). ∎

**Theorem 2.1.** *The Radon transform of the line indicator function of line* $\boldsymbol{l} = (b_l, \theta_l)$ *is*

$$\mathcal{R}\{\mathcal{L}[\boldsymbol{l}]\}(b,\boldsymbol{\xi}) = \delta(b - b_l, \theta - \theta_l). \tag{2.14}$$

*Proof:* We start by considering the line $\boldsymbol{l}_0 = (0,0)$, or $x = 0$. From the definition of the Radon transform,

$$\mathcal{R}\{\mathcal{L}[\boldsymbol{l}_0]\}(b,\boldsymbol{\xi}) = \int \mathbf{1}_{\{x=0\}}(\boldsymbol{x})\delta(b - \boldsymbol{\xi}\cdot\boldsymbol{x})d\boldsymbol{x}.$$

We next consider two cases. First, when $\theta = 0$,

$$\mathcal{R}\{\mathcal{L}[\boldsymbol{l}_0]\}(b,\boldsymbol{\xi}) = \int\int \mathbf{1}_{\{x=0\}}(x)\delta(b-x)dxdy = \int \mathbf{1}_{\{x=0\}}(b)dy = \begin{cases} \infty & \text{if } b = 0, \\ 0 & \text{if } b \neq 0. \end{cases}$$

Second, when $\theta \neq 0$,

$$\begin{aligned}
\mathcal{R}\{\mathcal{L}[\boldsymbol{l}_0]\}(b,\boldsymbol{\xi}) &= \int\int \mathbf{1}_{\{x=0\}}(x)\delta(b - x\cos\theta - y\sin\theta)dxdy \\
&= \frac{1}{\sin\theta}\int \mathbf{1}_{\{(x=0)\}}(x)\left[\int \delta(b - x\cos\theta - u)du\right]dx \\
&= \frac{1}{\sin\theta}\int \mathbf{1}_{\{(x=0)\}}(x)dx \\
&= 0.
\end{aligned}$$

Hence,

$$\mathcal{R}\{\mathcal{L}[\boldsymbol{l}_0]\}(b,\boldsymbol{\xi}) = \delta(b,\boldsymbol{\xi}),$$

and the theorem follows from Lemma 2.3 since

$$\begin{aligned}
\mathcal{R}\{\mathcal{L}[\boldsymbol{l}](\boldsymbol{x})\}(b,\theta) &= \mathcal{R}\{\mathcal{L}[\boldsymbol{l}_0](\boldsymbol{x})\}(b - b_l\cos(\theta-\theta_l), \theta-\theta_l) \\
&= \delta(b - b_l\cos(\theta-\theta_l), \theta-\theta_l) \\
&= \delta(b-b_l, \theta-\theta_l).
\end{aligned}$$

■

## 2.4 The Radon transform of the line segment indicator function

**Definition 2.4.** A *line segment* $\boldsymbol{g} = (b, \boldsymbol{\xi}, \mathcal{X})$ is the restriction of a line $(b, \boldsymbol{\xi})$ to a closed and bounded region $\mathcal{X}$. It will be denoted simply by *segment*.

**Definition 2.5.** The *support set of a segment* $\boldsymbol{g} = (b, \boldsymbol{\xi}, \mathcal{X})$ is the set

$$\mathcal{S}(\boldsymbol{g}) = \{\boldsymbol{x} \in \mathbb{R}^2 \mid b = \boldsymbol{\xi}\cdot\boldsymbol{x}, \boldsymbol{x} \in \mathcal{X}\}. \tag{2.15}$$

**Definition 2.6.** The *line indicator function* of segment $\boldsymbol{g}$ is the binary map

$$\mathcal{G} : \mathbb{R}^2 \to \{0,1\}$$

$$\mathcal{G}[\boldsymbol{g}](\boldsymbol{x}) = \mathbf{1}_{\mathcal{S}(\boldsymbol{g})}(\boldsymbol{x}) = \begin{cases} 1 & \text{if } \boldsymbol{x} \in \mathcal{S}(\boldsymbol{g}), \\ 0 & \text{otherwise.} \end{cases} \tag{2.16}$$

**Theorem 2.2.** *The Radon transform of the line segment indicator function of segment* $\boldsymbol{g} = (b_l, \theta_l, \mathcal{X})$ *is*

$$\mathcal{R}\{\mathcal{G}[\boldsymbol{g}]\}(b,\boldsymbol{\xi}) = \mathbf{1}_{\{b=b_l,\theta=\theta_l\}}(b,\boldsymbol{\xi})\,\mathfrak{L}(\boldsymbol{g}), \tag{2.17}$$

*where*

$$\mathfrak{L}(\boldsymbol{g}) = \int_{\mathcal{X}\cap\mathcal{S}(\boldsymbol{g})} d\boldsymbol{x}. \tag{2.18}$$

*is the length of segment* $\boldsymbol{g}$.

*Proof:* From the definition of the Radon transform,

$$\begin{aligned}
\mathcal{R}\{\mathcal{G}[\boldsymbol{g}]\}(b,\boldsymbol{\xi}) &= \int \mathbf{1}_{\{b_l=\boldsymbol{x}\cdot\boldsymbol{\xi},\boldsymbol{x}\in\mathcal{X}\}}(\boldsymbol{x})\delta(b-\boldsymbol{\xi}\cdot\boldsymbol{x})\,d\boldsymbol{x} \\
&= \int_{\mathcal{X}} \mathbf{1}_{\{b_l=\boldsymbol{x}\cdot\boldsymbol{\xi}\}}(\boldsymbol{x})\delta(b-\boldsymbol{\xi}\cdot\boldsymbol{x})\,d\boldsymbol{x} \\
&= \begin{cases} \mu\left(\mathcal{X}\cap\mathcal{S}(\boldsymbol{g})\right) & \text{if } (b,\boldsymbol{\xi}) = (b_l,\boldsymbol{\xi}_l) \\ 0 & \text{otherwise.} \end{cases}
\end{aligned}$$

and the theorem follows. ∎

## 2.5 The Radon transform of the strip indicator function

**Definition 2.7.** A *strip* $\boldsymbol{s} = (b,\boldsymbol{\xi},w)$ is a line with a positive finite width $w$.

**Definition 2.8.** The *support set of a strip* $\boldsymbol{s} = (b,\boldsymbol{\xi},w)$ is the set

$$\mathcal{S}(\boldsymbol{s}) = \left\{\boldsymbol{x}\in\mathbb{R}^2 \,\middle|\, |b-\boldsymbol{\xi}\cdot\boldsymbol{x}| < \frac{w}{2}\right\}. \tag{2.19}$$

**Definition 2.9.** The *strip indicator function* of strip $\boldsymbol{s}$ is the binary map

$$\mathcal{B}:\mathbb{R}^2\to\{0,1\}$$

$$\mathcal{B}[\boldsymbol{s}](\boldsymbol{x}) = \mathbf{1}_{\mathcal{S}(\boldsymbol{s})}(\boldsymbol{x}) = \begin{cases} 1 & \text{if } \boldsymbol{x}\in\mathcal{S}(\boldsymbol{s}), \\ 0 & \text{otherwise.} \end{cases} \tag{2.20}$$

**Lemma 2.4.** *If* $\boldsymbol{s} = (b_s,\theta_s,w)$ *and* $\boldsymbol{s}' = (0,0,w)$, *then*

$$\mathcal{R}\{\mathcal{B}[\boldsymbol{s}](\boldsymbol{x})\}(b,\theta) = \mathcal{R}\{\mathcal{B}[\boldsymbol{s}'](\boldsymbol{x})\}(b-b_s\cos(\theta-\theta_s),\theta-\theta_s). \tag{2.21}$$

*Proof:* The proof is similar to that of Lemma 2.4. If $\mathbf{A} = T_{-b_s\boldsymbol{\xi}(\theta_s)}\circ\mathbf{R}_{\theta_s}$, and $\mathbf{z} = \mathbf{A}\boldsymbol{x}$, a derivation identical to that of the lemma can be used to show that $\mathcal{B}[\boldsymbol{s}](\mathbf{z}) = \mathcal{B}[\boldsymbol{s}'](\boldsymbol{x})$. Combining with Corollary 2.2 leads to (2.21). ∎

**Theorem 2.3.** *The Radon transform of the strip indicator function of strip* $\boldsymbol{s} = (b_s, \theta_s, w_s)$ *is*

$$\mathcal{R}\{\mathcal{B}[\boldsymbol{s}]\}(b, \boldsymbol{\xi}) = \begin{cases} \infty & \text{if } |b - b_s| \leq \frac{w_s}{2}, \theta = \theta_s \\ 0 & \text{if } |b - b_s| > \frac{w_s}{2}, \theta = \theta_s \\ \frac{w_s}{|\sin(\theta - \theta_s)|} & \text{if } \theta \neq \theta_s. \end{cases} \tag{2.22}$$

*Proof:* We start by considering the strip $\boldsymbol{s}_0 = (0, 0, w)$. From the definition of the Radon transform,

$$\begin{aligned} \mathcal{R}\{\mathcal{B}[\boldsymbol{s}_0]\}(b, \boldsymbol{\xi}) &= \int \mathbf{1}_{\left\{|x| < \frac{w}{2}\right\}}(\boldsymbol{x}) \delta(b - \boldsymbol{\xi} \cdot \boldsymbol{x})\, d\boldsymbol{x} \\ &= \int_{-\frac{w}{2}}^{\frac{w}{2}} \int_{-\infty}^{\infty} \delta(b - x\cos\theta - y\sin\theta)\, dxdy. \end{aligned}$$

We next consider two cases. First, when $\theta = 0$,

$$\begin{aligned} \mathcal{R}\{\mathcal{B}[\boldsymbol{s}_0]\}(b, \boldsymbol{\xi}) &= \int_{-\frac{w}{2}}^{\frac{w}{2}} \int_{-\infty}^{\infty} \delta(b - x)\, dxdy \\ &= \int_{-\infty}^{\infty} \mathbf{1}_{\left\{|b| < \frac{w}{2}\right\}}(b)\, dy \\ &= \begin{cases} \infty & \text{if } |b| \leq \frac{w}{2}, \\ 0 & \text{otherwise.} \end{cases} \end{aligned}$$

Second, when $\theta \neq 0$, consider the change of variables $u = y|\sin\theta|$ and $v = x|\cos\theta|$. If $\theta \leq \frac{\pi}{2}$,

$$\begin{aligned} \mathcal{R}\{\mathcal{B}[\boldsymbol{s}_0]\}(b, \boldsymbol{\xi}) &= \int_{-\frac{w}{2}|\cos\theta|}^{\frac{w}{2}|\cos\theta|} \int_{-\infty}^{\infty} \frac{1}{|\cos\theta\sin\theta|} \delta(b - u - v)\, dudv \\ &= \frac{1}{|\cos\theta\sin\theta|} \int_{-\frac{w}{2}|\cos\theta|}^{\frac{w}{2}|\cos\theta|} dv \\ &= \frac{w}{|\sin\theta|}. \end{aligned}$$

If $\theta \geq \frac{\pi}{2}$,

$$\begin{aligned} \mathcal{R}\{\mathcal{B}[\boldsymbol{s}_0]\}(b, \boldsymbol{\xi}) &= \int_{-\frac{w}{2}|\cos\theta|}^{\frac{w}{2}|\cos\theta|} \int_{-\infty}^{\infty} \frac{1}{|\cos\theta\sin\theta|} \delta(b + u + v)\, dudv \\ &= \frac{w}{|\sin\theta|}. \end{aligned}$$

Hence,

$$\mathcal{R}\{\mathcal{B}[\boldsymbol{s}_0]\}(b, \boldsymbol{\xi}) = \begin{cases} \infty & \text{if } |b| \leq \frac{w}{2}, \theta = 0 \\ 0 & \text{if } |b| > \frac{w}{2}, \theta = 0 \\ \frac{w}{|\sin\theta|} & \text{if } \theta \neq 0, \end{cases}$$

and the theorem follows from Lemma 2.4. ∎

## 2.6 The Radon transform of the pixel indicator function

**Definition 2.10.** A *pixel* $\boldsymbol{p} = (p_x, p_y, w, h)$ is a rectangular region with middle point $(p_x, p_y)$, width $w$, and height $h$.

**Definition 2.11.** The *support set of a pixel* $\boldsymbol{p} = (p_x, p_y, w, h)$ is the set

$$\mathcal{S}(\boldsymbol{p}) = \left\{ (x, y) \in \mathbb{R}^2 \,\middle|\, |x - p_x| \leq \frac{w}{2}, |y - p_y| \leq \frac{h}{2} \right\}. \tag{2.23}$$

**Definition 2.12.** The *pixel indicator function* of pixel $\boldsymbol{p}$ is the binary map

$$\mathcal{P} : \mathbb{R}^2 \to \{0, 1\}$$

$$\mathcal{P}[\boldsymbol{p}](\boldsymbol{x}) = \mathbf{1}_{\mathcal{S}(\boldsymbol{p})}(\boldsymbol{x}) = \begin{cases} 1 & \text{if } \boldsymbol{x} \in \mathcal{S}(\boldsymbol{p}), \\ 0 & \text{otherwise.} \end{cases} \tag{2.24}$$

**Lemma 2.5.** *If* $\boldsymbol{p} = (p_x, p_y, w, h)$ *and* $\boldsymbol{p}_0 = (0, 0, w, h)$, *then*

$$\mathcal{R}\{\mathcal{P}[\boldsymbol{p}](\boldsymbol{x})\}(b, \boldsymbol{\xi}) = \mathcal{R}\{\mathcal{P}[\boldsymbol{p}_0](\boldsymbol{x})\}(b - \boldsymbol{\xi} \cdot (p_x, p_y), \boldsymbol{\xi}). \tag{2.25}$$

*Proof:* Consider the linear transformation $\mathbf{z} = T_{(p_x, p_y)}(\boldsymbol{x})$, where $T_{(p_x, p_y)}(\boldsymbol{x})$ is as defined in Lemma 2.3. Then, by the shifting property of the Radon transform,

$$\mathcal{R}\{\mathcal{P}[\boldsymbol{p}_0](\mathbf{z})\}(b, \boldsymbol{\xi}) = \mathcal{R}\{\mathcal{P}[\boldsymbol{p}_0](\boldsymbol{x})\}(b - \boldsymbol{\xi} \cdot (p_x, p_y), \boldsymbol{\xi}).$$

Since, for any $\boldsymbol{x} \in \mathcal{S}(\mathbf{p})$,

$$|x - p_x| \leq \frac{w}{2} \quad \text{and} \quad |y - p_y| \leq \frac{h}{2}$$

and $\mathbf{z} = \boldsymbol{x} - (p_x, p_y)$, it follows that

$$|z_x| \leq \frac{w}{2} \quad \text{and} \quad |z_y| \leq \frac{h}{2}.$$

Hence, $\boldsymbol{x} \in \mathcal{S}(\boldsymbol{p})$ if and only if $\mathbf{z} \in \mathcal{S}(\boldsymbol{p}_0)$ and, therefore, $\mathcal{P}[\boldsymbol{p}_0](\mathbf{z}) = \mathcal{P}[\boldsymbol{p}](\boldsymbol{x})$. ∎

**Remark 2.1.** An alternative proof can be derived from the following interpretation of the indicator function $\mathcal{P}[\boldsymbol{p}]$

$$\mathcal{P}[\boldsymbol{p}](\boldsymbol{x}) = \mathcal{P}[\boldsymbol{p}_0](\boldsymbol{x} - (p_x, p_y)) = \mathcal{P}[\boldsymbol{p}_0](\boldsymbol{x}) * \delta(\boldsymbol{x} - (p_x, p_y)). \tag{2.26}$$

The lemma follows from the convolution property and Lemma 2.1. The interpretation of (2.26) will be useful for the derivation of some future results.

**Lemma 2.6.** *The Radon transform of the pixel indicator function of pixel* $\boldsymbol{p}_0 = (0, 0, w, h)$ *is*

$$\mathcal{R}\{\mathcal{P}[\boldsymbol{p}_0]\}(b, \boldsymbol{\xi}) = \begin{cases} \frac{h}{|\cos\theta|} & \text{if } 0 \le |b| \le \frac{1}{2}(w|\cos\theta| - h\sin\theta), \\ \frac{\frac{1}{2}(w|\cos\theta| + h\sin\theta) - |b|}{|\cos\theta|\sin\theta} & \text{if } \frac{1}{2}|w|\cos\theta| - h\sin\theta| < |b| \le \frac{1}{2}(w|\cos\theta| + h\sin\theta), \\ \frac{w}{\sin\theta} & \text{if } 0 \le |b| \le \frac{1}{2}(h\sin\theta - w|\cos\theta|). \end{cases} \tag{2.27}$$

*Proof:* Since $\mathcal{P}[\boldsymbol{p}_0](x, y) = \mathcal{P}[\boldsymbol{p}_0](x, -y) = \mathcal{P}[\boldsymbol{p}_0](-x, y) = \mathcal{P}[\boldsymbol{p}_0](-x, -y)$, from the symmetry properties (2.3)-(2.5), it follows that

$$\mathcal{R}\{\mathcal{P}[\boldsymbol{p}_0]\}(b, \theta) = \mathcal{R}\{\mathcal{P}[\boldsymbol{p}_0]\}(-b, \pi - \theta) = \mathcal{R}\{\mathcal{P}[\boldsymbol{p}_0]\}(b, \pi - \theta) = \mathcal{R}\{\mathcal{P}[\boldsymbol{p}_0]\}(-b, \theta). \tag{2.28}$$

We start by considering $b \ge 0$ and $\theta \in [0, \frac{\pi}{2}]$. From the definition of the Radon transform,

$$\begin{aligned} \mathcal{R}\{\mathcal{P}[\boldsymbol{p}_0]\}(b, \boldsymbol{\xi}) &= \int \mathbf{1}_{\left\{|x| < \frac{w}{2}, |y| < \frac{h}{2}\right\}}(\boldsymbol{x}) \delta(b - \boldsymbol{\xi} \cdot \boldsymbol{x})\, d\boldsymbol{x} \\ &= \int_{-\frac{w}{2}}^{\frac{w}{2}} \int_{-\frac{h}{2}}^{\frac{h}{2}} \delta(b - x\cos\theta - y\sin\theta)\, dxdy. \end{aligned}$$

We next consider three cases. First, when $\theta = 0$,

$$\begin{aligned} \mathcal{R}\{\mathcal{P}[\boldsymbol{p}_0]\}(b, \boldsymbol{\xi}) &= \int_{-\frac{w}{2}}^{\frac{w}{2}} \int_{-\frac{h}{2}}^{\frac{h}{2}} \delta(b - x)\, dxdy \\ &= \int_{-\frac{h}{2}}^{\frac{h}{2}} \mathbf{1}_{\left\{|b| < \frac{w}{2}\right\}}(b)\, dy \\ &= \begin{cases} h & \text{if } |b| \le \frac{w}{2}, \\ 0 & \text{otherwise.} \end{cases} \end{aligned}$$

Second, when $\theta = \frac{\pi}{2}$,

$$\begin{aligned} \mathcal{R}\{\mathcal{P}[\boldsymbol{p}_0]\}(b, \boldsymbol{\xi}) &= \int_{-\frac{w}{2}}^{\frac{w}{2}} \int_{-\frac{h}{2}}^{\frac{h}{2}} \delta(b - y)\, dxdy \\ &= \int_{-\frac{w}{2}}^{\frac{w}{2}} \mathbf{1}_{\left\{|b| < \frac{h}{2}\right\}}(b)\, dx \\ &= \begin{cases} w & \text{if } |b| \le \frac{h}{2}, \\ 0 & \text{otherwise.} \end{cases} \end{aligned}$$

Finally, when $\theta \in \left(0, \frac{\pi}{2}\right)$, making $u = y \sin\theta$ and $v = x\cos\theta$

$$\begin{aligned}
\mathcal{R}\{\mathcal{P}[\boldsymbol{p}_0]\}(b,\boldsymbol{\xi}) &= \int_{-\frac{w}{2}\cos\theta}^{\frac{w}{2}\cos\theta}\int_{-\frac{h}{2}\sin\theta}^{\frac{h}{2}\sin\theta} \frac{1}{\cos\theta\sin\theta}\delta(b-u-v)dudv \\
&= \frac{1}{\cos\theta\sin\theta}\int_{-\frac{w}{2}\cos\theta}^{\frac{w}{2}\cos\theta} \mathbf{1}_{\{|b-v|\leq\frac{h}{2}\sin\theta\}}(v)dv \\
&= \frac{1}{\cos\theta\sin\theta}\int_{\max(-\frac{w}{2}\cos\theta, b-\frac{h}{2}\sin\theta)}^{\min(\frac{w}{2}\cos\theta, b+\frac{h}{2}\sin\theta)} dv,
\end{aligned}$$

which, after some algebra, can be written as

$$\mathcal{R}\{\mathcal{P}[\boldsymbol{p}_0]\}(b,\boldsymbol{\xi}) = \begin{cases} \frac{h}{\cos\theta} & \text{if } 0 \leq b \leq \frac{1}{2}(w\cos\theta - h\sin\theta), \\ \frac{\frac{1}{2}(w\cos\theta + h\sin\theta) - b}{\cos\theta\sin\theta} & \text{if } \frac{1}{2}|w\cos\theta - h\sin\theta| < b \leq \frac{1}{2}(w\cos\theta + h\sin\theta), \\ \frac{w}{\sin\theta} & \text{if } 0 \leq b \leq \frac{1}{2}(h\sin\theta - w\cos\theta). \end{cases}$$

Notice that the two first cases can be obtained by making $\theta = 0$ and $\theta = \frac{\pi}{2}$ in this equation, implying that this equation is valid for all $(b,\theta) \in \mathbb{R}^+ \times \left[0, \frac{\pi}{2}\right]$. The lemma follows from the combination with the equalities of (2.28). ∎

Figure 2.2 presents surface and contour plots of the Radon transform of pixel $\boldsymbol{p}_0 = (0,0,1,1)$. While, to a first-order approximation, the transform can be approximated by a binary function, this can introduce non-negligible error for the values of $(b,\theta)$ associated with the pixel diagonals (where the amplitude of the Radon transform reaches the value $\sqrt{2}$).

**Theorem 2.4.** *The Radon transform of the pixel indicator function of pixel* $\boldsymbol{p} = (p_x, p_y, w, h)$ *is*

$$\mathcal{R}\{\mathcal{P}[\boldsymbol{p}_0]\}(b,\boldsymbol{\xi}) = \begin{cases} \frac{h}{|\boldsymbol{\xi}|\cdot\mathbf{e}_x} & \textit{if } 0 \leq d \leq \frac{1}{2}|\boldsymbol{\xi}|\cdot\mathbf{v}, \\ \frac{\frac{1}{2}|\boldsymbol{\xi}|\cdot\mathbf{u} - d}{(|\boldsymbol{\xi}|\cdot\mathbf{e}_x)(|\boldsymbol{\xi}|\cdot\mathbf{e}_y)} & \textit{if } \frac{1}{2}||\boldsymbol{\xi}|\cdot\mathbf{v}| < d \leq \frac{1}{2}|\boldsymbol{\xi}|\cdot\mathbf{u}, \\ \frac{w}{|\boldsymbol{\xi}|\cdot\mathbf{e}_y} & \textit{if } 0 \leq d \leq -\frac{1}{2}|\boldsymbol{\xi}|\cdot\mathbf{v}. \end{cases} \tag{2.29}$$

*where* $\mathbf{c}_p = (p_x, p_y)^T$, $\mathbf{e}_x = (1,0)^T$, $\mathbf{e}_y = (0,1)^T$, $\mathbf{u} = (w,h)^T$, *and* $\mathbf{v} = (w,-h)^T$, $|\boldsymbol{\xi}| = (|\cos(\theta)|, \sin(\theta))^T$ *and* $d = |b - \boldsymbol{\xi}\cdot\mathbf{c}_p|$.

*Proof:* Denoting $\mathbf{e}_x = (1,0)^T$, $\mathbf{e}_y = (0,1)^T$, $\mathbf{u} = (w,h)^T$, and $\mathbf{v} = (w,-h)^T$, (2.27) can also be written as

$$\mathcal{R}\{\mathcal{P}[\boldsymbol{p}_0]\}(b,\boldsymbol{\xi}) = \begin{cases} \frac{h}{|\boldsymbol{\xi}|\cdot\mathbf{e}_x} & \text{if } 0 \leq |b| \leq \frac{1}{2}|\boldsymbol{\xi}|\cdot\mathbf{v}, \\ \frac{\frac{1}{2}|\boldsymbol{\xi}|\cdot\mathbf{u} - |b|}{(|\boldsymbol{\xi}|\cdot\mathbf{e}_x)(|\boldsymbol{\xi}|\cdot\mathbf{e}_y)} & \text{if } \frac{1}{2}||\boldsymbol{\xi}|\cdot\mathbf{v}| < |b| \leq \frac{1}{2}|\boldsymbol{\xi}|\cdot\mathbf{u}, \\ \frac{w}{|\boldsymbol{\xi}|\cdot\mathbf{e}_y} & \text{if } 0 \leq |b| \leq -\frac{1}{2}|\boldsymbol{\xi}|\cdot\mathbf{v}. \end{cases}$$

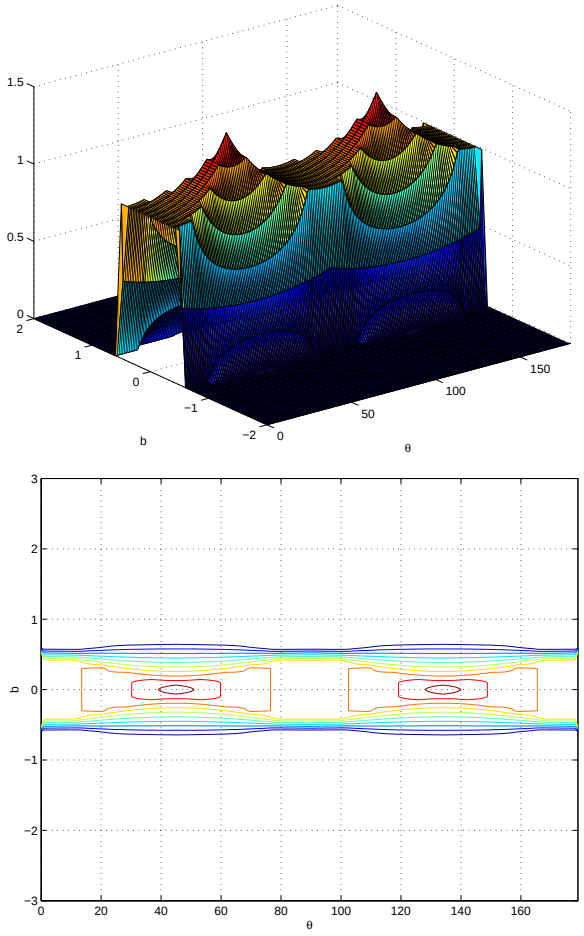


Figure 2.2: Surface (top) and contour (bottom) plots of the Radon transform of the pixel indicator function of pixel $\boldsymbol{p}_0 = (0, 0, w, h)$ with $w = h = 1$.

The theorem follows from Lemma 2.5. ■

Figure 2.3 presents surface and contour plots of the Radon transform of the indicator function of pixel $\boldsymbol{p} = (1, -1, 1, 1)$. The figure is quite intuitive in light of Remark 2.1, Lemma 2.1, and the convolution property of Table 2.1. Since the transform of the convolution is the convolution of transforms and the transform of the delta function is a sinusoid, it follows, from Remark 2.1, that the Radon transform of $\mathcal{P}[\boldsymbol{p}]$ is the modulation of a sinusoid by the Radon transform of $\mathcal{P}[\boldsymbol{p}_0]$.

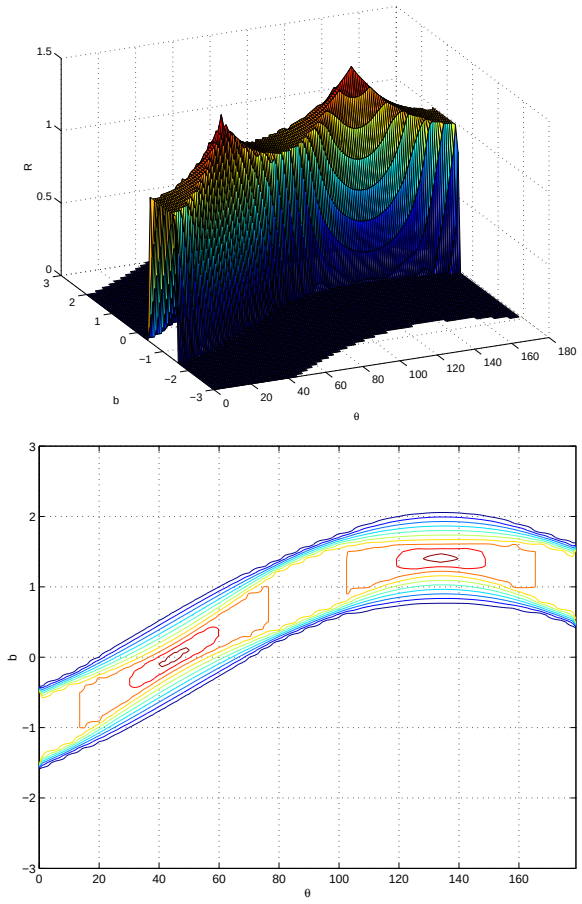


Figure 2.3: Surface (top) and contour (bottom) plots of the Radon transform of the indicator function of pixel $\boldsymbol{p} = (p_x, p_y, w, h)$ with $(p_x, p_y) = (1, -1)$ and $w = h = 1$.

## 2.7 The Radon transform of a pixelated function

**Definition 2.13.** A *lattice* is a discrete subgroup of $\mathbb{R}^2$ of the form

$$\mathcal{L} = \{\boldsymbol{x} \in \mathbb{R}^2 \,|\, \boldsymbol{x} = m\,\mathbf{a} + n\,\mathbf{b}, m, n \in \mathbb{Z}\}.$$

The pair of generating vectors $(\mathbf{a}, \mathbf{b})$ is called the *lattice basis*.

It follows from that definition that, associated to each pixel with width $w$ and height $h$, there is a lattice

$$\mathcal{L}_{w,h} = \{\boldsymbol{x} \in \mathbb{R}^2 \,|\, \boldsymbol{x} = m\,w\,\mathbf{e}_x + n\,h\,\mathbf{e}_y, m, n \in \mathbb{Z}\},$$

where, as before, $\mathbf{e}_x = (1, 0)$ and $\mathbf{e}_y = (0, 1)$. *Pixel lattices* are the support of pixelated functions.

**Definition 2.14.** If $f$ is a mapping

$$f : \mathcal{L}_{w,h} \to \mathbb{R},$$

the *pixelated function* associated with $f$ is the mapping

$$f_p : \mathbb{R}^2 \to \mathbb{R}$$

$$f_p(\boldsymbol{x}) = \sum_{i \,|\, \boldsymbol{p}_i \in \mathcal{L}_{w,h}} a_i \mathcal{P}[\boldsymbol{p}_i](\boldsymbol{x}) \tag{2.30}$$

where $a_i = f(\boldsymbol{p}_i)$ and $\mathcal{P}[\boldsymbol{p}_i](\boldsymbol{x})$ is the pixel indicator function of pixel $\boldsymbol{p}_i$ (2.24).

There are many examples of pixelated functions. In the context of this thesis, the most interesting one is the set of digital images, which are pixelated functions with range space $\mathbb{Z}^+$. The following theorem provides an expression for the Radon transform of a pixelated function.

**Theorem 2.5.** *The Radon transform of the pixelated function (2.30) is*

$$\mathcal{R}[f_p(\boldsymbol{x})](b, \boldsymbol{\xi}) = \sum_{i \,|\, \boldsymbol{p}_i \in \mathcal{L}_{w,h}} a_i \mathcal{R}\{\mathcal{P}[\boldsymbol{p}_0](\boldsymbol{x})\}(b - (p_{ix}, p_{iy}) \cdot \boldsymbol{\xi}, \boldsymbol{\xi}) \tag{2.31}$$

*with* $\mathcal{R}\{\mathcal{P}[\boldsymbol{p}_0](\boldsymbol{x})\}(b, \boldsymbol{\xi})$ *as given by (2.27).*

*Proof:* From (2.26) and, as before, denoting $\boldsymbol{p}_0 = (0, 0, w, h)$ and $\boldsymbol{p}_i = (p_{ix}, p_{iy}, w, h)$

$$\begin{aligned}
\mathcal{R}\{f_p(\boldsymbol{x}))\}(b, \boldsymbol{\xi}) &= \mathcal{R}\left\{ \sum_{i \,|\, \boldsymbol{p}_i \in \mathcal{L}_{w,h}} a_i \mathcal{P}[\boldsymbol{p}_0](\boldsymbol{x}) * \delta(\boldsymbol{x} - (p_{ix}, p_{iy})) \right\}(b, \boldsymbol{\xi}) \\
&= \sum_{i \,|\, \boldsymbol{p}_i \in \mathcal{L}_{w,h}} a_i \mathcal{R}\{\mathcal{P}[\boldsymbol{p}_0](\boldsymbol{x}) * \delta(\boldsymbol{x} - (p_{ix}, p_{iy}))\}(b, \boldsymbol{\xi}) \\
&= \mathcal{R}\left\{\mathcal{P}[\boldsymbol{p}_0](\boldsymbol{x})\right\}(b, \boldsymbol{\xi}) * \sum_{i \,|\, \boldsymbol{p}_i \in \mathcal{L}_{w,h}} a_i \mathcal{R}\left\{\delta(\boldsymbol{x} - (p_{ix}, p_{iy}))\right\}(b, \boldsymbol{\xi}) \\
&= \mathcal{R}\{\mathcal{P}[\boldsymbol{p}_0](\boldsymbol{x})\}(b, \boldsymbol{\xi}) * \sum_{i \,|\, \boldsymbol{p}_i \in \mathcal{L}_{w,h}} a_i \delta(b - (p_{ix}, p_{iy}) \cdot \boldsymbol{\xi}, \boldsymbol{\xi}),
\end{aligned}$$

where we have used the linearity and convolution properties of the Radon transform and Lemma 2.1. The theorem follows from the convolution property of the delta function. ∎

## 2.8 Smoothing

The effect, in Radon space, of smoothing a function $f(\boldsymbol{x})$ follows trivially from the convolution property.

**Notation 2.1.** If $h$ is a low-pass filter, $f * h$ is called the *smoothing* of $f$ by $h$.

**Lemma 2.7.** *The Radon transform of the smoothing of $f$ by $h$ is*

$$\mathcal{R}[f * h](b, \boldsymbol{\xi}) = \mathcal{R}[f](b, \boldsymbol{\xi}) * \mathcal{R}[h](b, \boldsymbol{\xi}). \tag{2.32}$$

*Proof :* The lemma is a trivial consequence of the convolution property of the Radon transform. ∎

**Corollary 2.3.** *The Radon transform of the smoothing of the line indicator function of the line $\boldsymbol{l} = (b_l, \theta_l)$ by $h$ is*

$$\mathcal{R}\{\mathcal{L}[\boldsymbol{l}] * h\}(b, \theta) = \mathcal{R}[h](b - b_l, \theta - \theta_l). \tag{2.33}$$

*Proof:* The corollary follows from (2.14), (2.32), and the convolution properties of the Dirac delta function. ∎

One commonly used smoothing filter is the Gaussian. The next lemma characterizes its Radon transform.

**Lemma 2.8.** *The Radon transform of a two-dimensional Gaussian with mean* $\boldsymbol{\mu} = (\mu_x, \mu_y)$ *and covariance* $\boldsymbol{\Sigma} = diag(\sigma_x, \sigma_y)$

$$\rho(x,y) = \frac{1}{2\pi\sigma_x\sigma_y} e^{-\frac{(x-\mu_x)^2}{2\sigma_x^2} - \frac{(y-\mu_y)^2}{2\sigma_y^2}}$$

*is*

$$\mathcal{R}[\rho(x,y)](b,\boldsymbol{\xi}) = \frac{1}{\sqrt{2\pi}s} e^{-\frac{(b-\mu_b)^2}{s^2}}, \tag{2.34}$$

*where*

$$\begin{aligned} s^2 &= \sigma_x^2 \cos^2\theta + \sigma_y^2 \sin^2\theta \\ \mu_b &= \mu_x \cos\theta + \mu_y \sin\theta. \end{aligned}$$

*Proof:* Let $\rho_1(x,y) = \frac{1}{2\pi} e^{-\frac{x^2}{2} - \frac{y^2}{2}}$, then

$$\mathcal{R}[\rho_1(x,y)](b,\boldsymbol{\xi}) = \int\int \frac{1}{2\pi} e^{-\frac{x^2}{2} - \frac{y^2}{2}} \, \delta(b - \xi_1 x - \xi_2 y)\, dxdy.$$

Consider the orthogonal linear transformation

$$\begin{bmatrix} u \\ v \end{bmatrix} = \mathbf{R}_\theta \begin{bmatrix} x \\ y \end{bmatrix},$$

with $\mathbf{R}_\theta$ as in (2.7). Using this change of variables,

$$\begin{aligned} \mathcal{R}[\rho_1(x,y)](b,\boldsymbol{\xi}) &= \int\int \frac{1}{2\pi} e^{-\frac{u^2}{2} - \frac{v^2}{2}} \, \delta(b-u)\, dudv \\ &= \frac{e^{-b^2}}{\sqrt{2\pi}} \int \frac{1}{\sqrt{2\pi}} e^{-\frac{v^2}{2}}\, dv \\ &= \frac{1}{\sqrt{2\pi}}\, e^{-b^2}. \end{aligned}$$

Now, notice that

$$\rho(\boldsymbol{x}) = \frac{1}{\sqrt{2\pi}\sigma_x\sigma_y}\, \rho_1(\boldsymbol{\Sigma}^{-1}\, \boldsymbol{x} - \boldsymbol{\mu})$$

and, by Corollary 2.2,

$$\mathcal{R}[\rho(x,y)](b,\boldsymbol{\xi}) = \frac{1}{\sqrt{2\pi}\sigma_x\sigma_y} \frac{|\det \boldsymbol{\Sigma}|}{\|\boldsymbol{\Sigma}\,\boldsymbol{\xi}\|} \mathcal{R}[\rho_1(x,y)] \left( \frac{b - \boldsymbol{\Sigma}\,\boldsymbol{\xi}\cdot\boldsymbol{\mu}}{\|\boldsymbol{\Sigma}\,\boldsymbol{\xi}\|}, \frac{\boldsymbol{\Sigma}\,\boldsymbol{\xi}}{\|\boldsymbol{\Sigma}\,\boldsymbol{\xi}\|} \right),$$

and the lemma follows. ∎

# Chapter 3

# The Radon transform of a pixelated edge map

In this chapter, we focus our attention on the set of pixelated lines. We start by characterizing this set through the derivation of a pair of conditions which are necessary and sufficient for a line to be one of its members. We then define the pixelated line associated with a line $\boldsymbol{l}$ as the set of pixels that are intersected by $\boldsymbol{l}$. Next, we derive exact expressions for some of the quantities of interest to the characterization of the pixelated line, e.g. its supporting set and the Radon transform of its indicator function. It is shown that these functions are a sum of many other elementary functions. This has the unfortunate consequence that the resulting expressions tend to be computationally intractable, and motivates a search for bounds that can provide an equally useful characterization at much lower computational complexity. We show that tight upper- and lower-bounds of low computational complexity can indeed be derived for both quantities.

The remainder of the chapter addresses the characterization of pixelated edge maps. We start by introducing the edge indicator function which classifies lines into one of two classes: edges and non-edges. The pixelated edge map is the set of all pixelated lines that are associated with edges. We derive the Radon transforms for both the individual indicator functions and the edge map. Finally, we introduce an approximation to the Radon transform of the pixel, the separable approximation, that reduces the Radon transform of the edge map to the corresponding Hough transform. This shows that the Hough transform is really an approximation to the Radon transform. It becomes clear that the former does not eliminate the most important causes of the computational complexity of the latter, and it is unclear that there might be any benefit in studying it.

## 3.1 The set of lines supported by $\mathcal{L}_{w,h}$

The following definition follows from Definition 2.2.

**Definition 3.1.** A line $\boldsymbol{l}$ is said to be *supported* by $\mathcal{L}_{w,h}$ if there are at least two points

$$\boldsymbol{x}_1, \boldsymbol{x}_2 \in \mathcal{L}_{w,h} \text{ such that } \boldsymbol{x}_1, \boldsymbol{x}_2 \in \mathcal{S}(\boldsymbol{l}).$$

The set of all lines supported by $\mathcal{L}_{w,h}$ is denoted by $\mathcal{SL}_{w,h}$.

The following theorem characterizes $\mathcal{SL}_{w,h}$.

**Theorem 3.1.** *$\boldsymbol{l} \in \mathcal{SL}_{w,h}$ if and only if the following conditions hold*

**i)** *$\boldsymbol{l}$ has slope $m = q\frac{h}{w}, q \in \mathbb{Q}$,*

**ii)** *there exists $(k, l)$ such that the point $(lw, kh) \in \mathcal{S}(\boldsymbol{l})$.*

*Proof:* Consider a line $\boldsymbol{l} \in \mathcal{SL}_{w,h}$. By the definition of $\mathcal{SL}_{w,h}$, there is one point $\boldsymbol{x} \in \mathcal{L}_{w,h}$ such that $\boldsymbol{x} \in \mathcal{S}(\boldsymbol{l})$. Since, by definition of $\mathcal{L}_{w,h}$, $\boldsymbol{x} = (mw, nh), m, n \in \mathbb{Z}$, condition **ii)** is satisfied by simply setting $l = m$ and $k = n$. Still by the definition of $\mathcal{SL}_{w,h}$, there is a second point $\boldsymbol{x}' \in \mathcal{L}_{w,h}$ such that $\boldsymbol{x}' \in \mathcal{S}(\boldsymbol{l})$. Denote the second point by $\boldsymbol{x}' = (l'w, k'h)$. The two points $\boldsymbol{x}$ and $\boldsymbol{x}'$ define $\boldsymbol{l}$ by the following equation

$$y = \frac{k' - k}{l' - l}\,\frac{h}{w}\,x + b,$$

where, since $y = kh$ when $x = lw$,

$$b = kh - \frac{k' - k}{l' - l}\,lh.$$

Denoting $\alpha = k' - k$ and $\beta = l' - l$, we have

$$y = \frac{\alpha}{\beta}\,\frac{h}{w}\,x + \left(k - \frac{\alpha}{\beta}\,l\right)h,$$

and the slope of $\boldsymbol{l}$ is

$$m = \frac{\alpha}{\beta}\,\frac{h}{w} = q\,\frac{h}{w}$$

where, since $\alpha, \beta \in \mathbb{Z}$, $q \in \mathbb{Q}$, therefore satisfying condition **i)**.

Conversely, when condition **ii)** holds, to show that $\boldsymbol{l} \in \mathcal{SL}_{w,h}$, it suffices to find another point $\boldsymbol{x}' \in \mathcal{L}_{w,h}$ such that $\boldsymbol{x}' \in \mathcal{S}(\boldsymbol{l})$. ¿From **i)**, given that $\boldsymbol{l}$ has slope $m = q\frac{h}{w}, q \in \mathbb{Q}$, we can write $m = \frac{\alpha}{\beta}\frac{h}{w}, \alpha, \beta \in \mathbb{Z}$. Furthermore, because **ii)** holds,

$$b = \left(h - \frac{\alpha}{\beta}\,l\right)h$$

leading to

$$y = \frac{\alpha}{\beta}\frac{h}{w}\,x + \left(k - \frac{\alpha}{\beta}\,l\right) h$$

and

$$x = (l+\beta)\,w \Leftrightarrow y = (k+\alpha)\,h.$$

Since $[(l+\beta)\,w, (k+\alpha)\,h] \in \mathcal{L}_{w,h}$, it follows that $\boldsymbol{l} \in \mathcal{SL}_{w,h}$. ∎

## 3.2 Pixelated lines

**Definition 3.2.** The set of pixels intersected by a line supported by $\mathcal{L}_{w,h}$ is denoted as a *pixelated line*.

**Definition 3.3.** The *pixel set* of a line $\boldsymbol{l}$ supported by $\mathcal{L}_{w,h}$ is

$$\mathcal{PS}(\boldsymbol{l}) = \{\boldsymbol{p} \,|\, (p_x, p_y) \in \mathcal{L}_{w,h}, \mathcal{S}(\boldsymbol{l}) \cap \mathcal{S}(\boldsymbol{p}) \neq \emptyset\} \tag{3.1}$$

and the pixelated line $\boldsymbol{l}_p$ associated with $\boldsymbol{l}$ is

$$\boldsymbol{l}_p = \bigcup_{i \,|\, \boldsymbol{p}_i \in \mathcal{PS}(\boldsymbol{l})} \boldsymbol{p}_i. \tag{3.2}$$

The set of all pixelated lines on $\mathcal{L}_{w,h}$ is denoted by $\mathcal{PL}_{w,h}$.

This definition is illustrated in Figure 3.1.

**Corollary 3.1.** *The pixelated line $\boldsymbol{l}_p$ associated with line $\boldsymbol{l}$ has support set*

$$\mathcal{S}(\boldsymbol{l}_p) = \bigcup_{i \,|\, \boldsymbol{p}_i \in \mathcal{PS}(\boldsymbol{l})} \mathcal{S}(\boldsymbol{p}_i) \tag{3.3}$$

*and indicator function*

$$\mathcal{X} : \mathbb{R}^2 \to \{0, 1\}$$

$$\mathcal{X}[\boldsymbol{l}_p](\boldsymbol{x}) = \mathbf{1}_{\mathcal{S}(\boldsymbol{l}_p)}(\boldsymbol{x}) = \sum_{i \,|\, \boldsymbol{p}_i \in \mathcal{PS}(\boldsymbol{l})} \mathcal{P}[\boldsymbol{p}_i](\boldsymbol{x}). \tag{3.4}$$

*Proof:* The corollary is a straightforward consequence of (3.2). ∎

The exact expression for the support set of the pixelated line is not easy to express in a compact form, i.e. a form that, unlike (3.3), does not involve the enumeration of all pixels. The following lemma shows that it is possible to derive two bounds that satisfy this property.

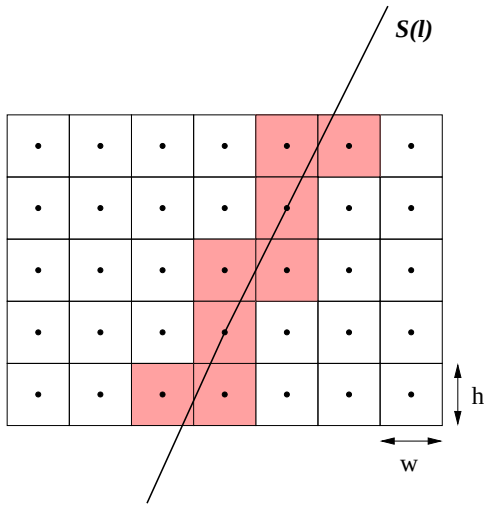


Figure 3.1: The shaded set is the pixelated line $\boldsymbol{l}_p$ associated with line $\boldsymbol{l}$.

**Lemma 3.1.** *The support set of the pixelated line $\boldsymbol{l}_p$ associated with line $\boldsymbol{l} = (b, \theta)$ satisfies the following relations*

$$\mathcal{S}(s_{in}(\boldsymbol{l})) \subset \mathcal{S}(\boldsymbol{l}_p) \subset \mathcal{S}(s_{out}(\boldsymbol{l})) \tag{3.5}$$

*where $s_{in}$ and $s_{out}$ are strips with parameters $s_{in}(\boldsymbol{l}) = \left(b, \theta, \frac{1}{2d(\theta)}\right)$ and $s_{out}(\boldsymbol{l}) = (b, \theta, d(\theta))$, and*

$$d(\theta) = \begin{cases} \sqrt{w^2+h^2}\cos\left(\theta - \arctan\frac{h}{w}\right) & \text{if } \theta \leq \frac{\pi}{2} \\ \sqrt{w^2+h^2}\cos\left(\pi - \theta - \arctan\frac{h}{w}\right) & \text{if } \theta > \frac{\pi}{2}. \end{cases} \tag{3.6}$$

*Proof:* Consider Figure 3.2 which depicts a pixel $\boldsymbol{p} \in \mathcal{S}(\boldsymbol{l}_p)$ and the line $\boldsymbol{l} = (b, \theta)$ (for the cases in which $\theta \leq \frac{\pi}{2}$ and $\theta > \frac{\pi}{2}$). Clearly, any strip with parameters $(b, \theta, d(\theta))$ that covers the pixel $\boldsymbol{p}$ must include all lines between $\boldsymbol{l}_1$ and $\boldsymbol{l}_2$. Assuming that the distance between the intersection of $\boldsymbol{l}$ and the main diagonal of the pixel is at a distance $\alpha$ from the furthest corner, it follows that $d(\theta)$ must be greater than $\alpha\cos\beta$, where $\beta$ is as indicated in the figure, i.e.

$$d(\theta) \geq \begin{cases} \alpha\cos\left(\theta - \arctan\frac{h}{w}\right) & \text{if } \theta \leq \frac{\pi}{2} \\ \alpha\cos\left(\pi - \theta - \arctan\frac{h}{w}\right) & \text{if } \theta > \frac{\pi}{2}. \end{cases}$$

Since, by definition, $\boldsymbol{l}$ is supported by $\mathcal{L}_{w,h}$, there must be at least two pixels for which the intersection point is the pixel center (and therefore mid-point of the main diagonal). This is the case in which $\alpha$ is minimum, with $\alpha = \frac{1}{2\sqrt{w^2+h^2}}$, leading to the lower bound of (3.5). Similarly, the upper bound follows from the fact that $\alpha \leq \sqrt{w^2+h^2}$. ∎

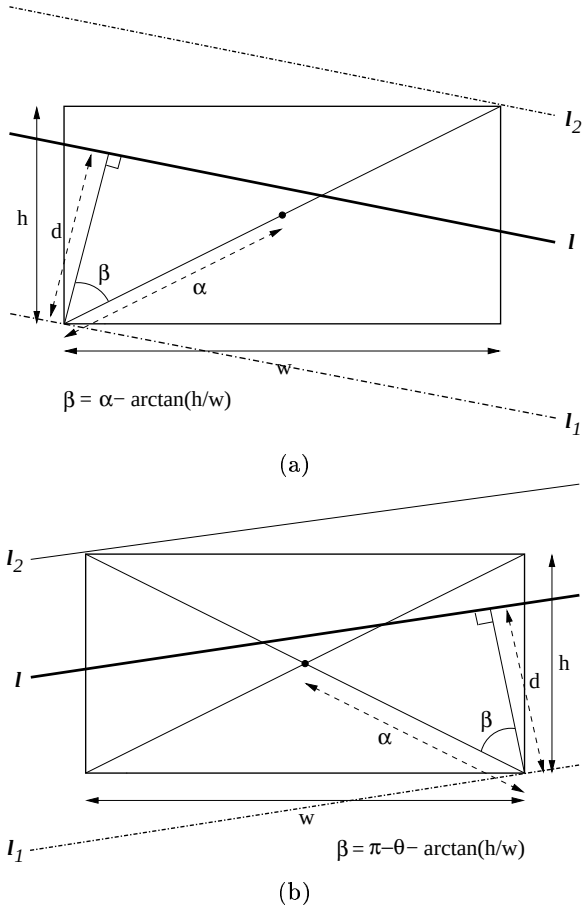


Figure 3.2: A pixel $\boldsymbol{p}$ contained in the pixelated line $\boldsymbol{l}_p$ and the associated line $\boldsymbol{l} = (b, \theta)$. (a) $\theta \leq \frac{\pi}{2}$, (b) $\theta > \frac{\pi}{2}$.

These two bounds on the support set of pixelated line lead to two simple bounds on the Radon transform of its indicator function. To show this, we first prove a generic result relating the Radon transforms of a set and any of its subsets.

**Lemma 3.2.** *Consider two sets $\mathcal{A}$ and $\mathcal{B}$ such that $\mathcal{B} \subset \mathcal{A}$ and the corresponding indicator functions $\mathbf{1}_{\{\mathcal{A}\}}(\boldsymbol{x})$ and $\mathbf{1}_{\{\mathcal{B}\}}(\boldsymbol{x})$. Then, $\forall (b, \boldsymbol{\xi})$,*

$$\mathcal{R}\left[\mathbf{1}_{\{\mathcal{B}\}}(\boldsymbol{x})\right](b, \boldsymbol{\xi}) \leq \mathcal{R}\left[\mathbf{1}_{\{\mathcal{A}\}}(\boldsymbol{x})\right](b, \boldsymbol{\xi}). \tag{3.7}$$

*Proof :* The lemma follows from the definition of the Radon transform since

$$\begin{aligned}
\mathcal{R}[\mathbf{1}_{\{\mathcal{A}\}}(\boldsymbol{x})](b, \boldsymbol{\xi}) &= \int_{\mathbb{R}^2} \mathbf{1}_{\{\mathcal{A}\}}(\boldsymbol{x}) \delta(b - \boldsymbol{\xi} \cdot \boldsymbol{x}) d\boldsymbol{x} \\
&= \int_{\mathcal{B}} \delta(b - \boldsymbol{\xi} \cdot \boldsymbol{x}) d\boldsymbol{x} + \int_{\mathcal{A} \cap \mathcal{B}^c} \delta(b - \boldsymbol{\xi} \cdot \boldsymbol{x}) d\boldsymbol{x} \\
&\geq \int_{\mathcal{B}} \delta(b - \boldsymbol{\xi} \cdot \boldsymbol{x}) d\boldsymbol{x} \\
&= \mathcal{R}\left[\mathbf{1}_{\{\mathcal{B}\}}(\boldsymbol{x})\right](b, \boldsymbol{\xi}),
\end{aligned}$$

where we have used the fact that $\int_{\mathcal{A} \cap \mathcal{B}^c} \delta(b - \boldsymbol{\xi} \cdot \boldsymbol{x}) d\boldsymbol{x} \geq 0$. ∎

The combination of the two previous lemmas leads to the following theorem.

**Theorem 3.2.** *The Radon transform of the indicator function of the pixelated line $\boldsymbol{l}_p$ associated with line $\boldsymbol{l} = (b_l, \theta_l)$ satisfies the following conditions.*

i) *If $\theta = \theta_l$,*

$$\mathcal{R}\{\mathcal{X}[\boldsymbol{l}_p](\boldsymbol{x})\}(b, \theta) = \begin{cases} 0 & \text{if } |b - b_l| \geq \frac{d(\theta_l)}{2} \\ \infty & \text{if } |b - b_l| \leq \frac{d(\theta_l)}{4} \end{cases} \tag{3.8}$$

*and*

$$0 < \mathcal{R}\{\mathcal{X}[\boldsymbol{l}_p](\boldsymbol{x})\}(b, \theta) < \infty \text{ if } \frac{d(\theta_l)}{4} \leq |b - b_l| \leq \frac{d(\theta_l)}{2}. \tag{3.9}$$

ii) *If $\theta \neq \theta_l$,*

$$\frac{d(\theta_l)}{2|\sin(\theta - \theta_l)|} \leq \mathcal{R}\{\mathcal{X}[\boldsymbol{l}_p](\boldsymbol{x})\}(b, \theta) \leq \frac{d(\theta_l)}{|\sin(\theta - \theta_l)|}. \tag{3.10}$$

*Proof:* From (3.5) and (3.7) it follows that

$$\mathcal{R}\left[\mathbf{1}_{\{\mathcal{S}(s_{in}(\boldsymbol{l}))\}}(\boldsymbol{x})\right](b, \boldsymbol{\xi}) \leq \mathcal{R}\{\mathcal{X}[\boldsymbol{l}_p](\boldsymbol{x})\}(b, \theta) \leq \mathcal{R}\left[\mathbf{1}_{\{\mathcal{S}(s_{out}(\boldsymbol{l}))\}}(\boldsymbol{x})\right](b, \boldsymbol{\xi})$$

or, using Definition 2.9,

$$\mathcal{R}\{\mathcal{B}[s_{in}(\boldsymbol{l})](\boldsymbol{x})\}(b,\boldsymbol{\xi}) \leq \mathcal{R}\{\mathcal{X}[\boldsymbol{l}_p](\boldsymbol{x})\}(b,\theta) \leq \mathcal{R}\{\mathcal{B}[s_{out}(\boldsymbol{l})](\boldsymbol{x})\}(b,\boldsymbol{\xi}).$$

Hence, from (2.22),

$$\mathcal{R}\{\mathcal{X}[\boldsymbol{l}_p](\boldsymbol{x})\}(b,\theta) \leq \begin{cases} \infty & \text{if } |b-b_l| \leq \frac{d(\theta_l)}{2}, \theta = \theta_l \\ 0 & \text{if } |b-b_l| > \frac{d(\theta_l)}{2}, \theta = \theta_l \\ \frac{d(\theta_l)}{|\sin(\theta-\theta_l)|} & \text{if } \theta \neq \theta_l \end{cases}$$

and

$$\mathcal{R}\{\mathcal{X}[\boldsymbol{l}_p](\boldsymbol{x})\}(b,\theta) \geq \begin{cases} \infty & \text{if } |b-b_l| \leq \frac{d(\theta_l)}{4}, \theta = \theta_l \\ 0 & \text{if } |b-b_l| > \frac{d(\theta_l)}{4}, \theta = \theta_l \\ \frac{d(\theta_l)}{2|\sin(\theta-\theta_l)|} & \text{if } \theta \neq \theta_l, \end{cases}$$

from which the theorem follows. ∎

This theorem shows that, for $\theta \neq \theta_l$, it is possible to bound $\mathcal{R}\{\mathcal{X}[\boldsymbol{l}_p](\boldsymbol{x})\}(b,\theta)$ from above and below by two simple expressions that do not depend on $b$. Figure 3.3 presents the two bounds (divided by $d(\theta_l)$) as a function of $\theta - \theta_l$. Notice that the constraints that they impose on $\mathcal{R}\{\mathcal{X}[\boldsymbol{l}_p](\boldsymbol{x})\}(b,\theta)$ are tight. The constant $d(\theta_l)$ is a scaling factor that re-scales the two bounds depending on the orientation of $\boldsymbol{l}$.

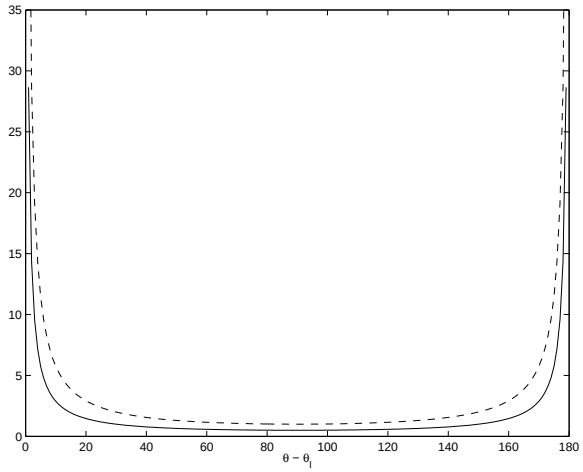


Figure 3.3: Ratio between the bounds of (3.10) and $d(\theta_l)$ as a function of $\theta - \theta_l$.

As the following corollary of Theorem 2.5 shows, it is also possible to derive the exact expression of $\mathcal{R}\{\mathcal{X}[\boldsymbol{l}_p](\boldsymbol{x})\}(b,\theta)$.

**Corollary 3.2.** *The Radon transform of the indicator function of the pixelated line* $\boldsymbol{l}_p$ *associated with line* $\boldsymbol{l}$ *is*

$$\mathcal{R}\{\mathcal{X}[\boldsymbol{l}_p](\boldsymbol{x})\}(b,\boldsymbol{\xi}) = \sum_{i\,|\,\boldsymbol{p}_i \in \mathcal{PS}(\boldsymbol{l})} \mathcal{R}\{\mathcal{P}[\boldsymbol{p}_0](\boldsymbol{x})\}(b-(p_{ix},p_{iy})\cdot\boldsymbol{\xi},\boldsymbol{\xi}) \tag{3.11}$$

*with* $\mathcal{R}\{\mathcal{P}[\boldsymbol{p}_0](\boldsymbol{x})\}(b,\boldsymbol{\xi})$ *as given by (2.27).*

*Proof:* From (2.30) and (3.4), the indicator function of pixelated line $\boldsymbol{l}_p$ is the pixelated function associated with the mapping

$$f : \mathcal{L}_{w,h} \to \{0,1\}$$

$$f(\boldsymbol{p}_i) = \begin{cases} 1 & \text{if } \boldsymbol{p}_i \in \mathcal{PS}(\boldsymbol{l}), \\ 0 & \text{otherwise.} \end{cases}$$

The corollary follows from (2.31). ∎

Since (3.11) requires the enumeration of all pixels in $\mathcal{PS}(\boldsymbol{l})$, it can only be computed when the pixel lattice is bounded. Figure 3.4 presents surface and contour plots for the case of the pixelated line with $\{(p_{ix},p_{iy})|p_{ix}=p_{iy}=p, p\in\{-3,\ldots,3\}\}$ and $w_i = h_i = 1, i = 1,\ldots,7$. As stated by the corollary, the Radon transform of the indicator function of a pixelated line is a sum of functions such as that shown in Figure 2.3, i.e. sinusoids modulated by the Radon transform of $\mathcal{P}[\boldsymbol{p}_0]$.

We next introduce an approximation that provides some insight on the relationship between the Radon transform and a related transform that is frequently used in computer vision: the Hough transform (HOUGH (1962), ILLINGWORTH AND KITTLER (1988)).

## 3.3 The separable approximation

**Definition 3.4.** The *separable approximation* to the Radon transform of the pixel indicator function of pixel $\boldsymbol{p}_0 = (0,0,w,h)$ is

$$\tilde{\mathcal{R}}\{\mathcal{P}[\boldsymbol{p}_0](\boldsymbol{x})\}(b,\boldsymbol{\xi}) = \mathcal{R}\{\mathcal{P}[\boldsymbol{p}_0](\boldsymbol{x})\}(0,\boldsymbol{\xi}) \times \mathbf{1}_{\{|b|\le\min(\frac{w}{2},\frac{h}{2})\}}, \tag{3.12}$$

where

$$\mathcal{R}\{\mathcal{P}[\boldsymbol{p}_0](\boldsymbol{x})\}(0,\boldsymbol{\xi}) = \begin{cases} \frac{w}{\sin\theta} & \text{if } \theta \in \left[\arctan\left(\frac{w}{h}\right), \frac{\pi}{2} + \arctan\left(\frac{w}{h}\right)\right] \\ \frac{h}{|\cos\theta|} & \text{otherwise.} \end{cases} \tag{3.13}$$

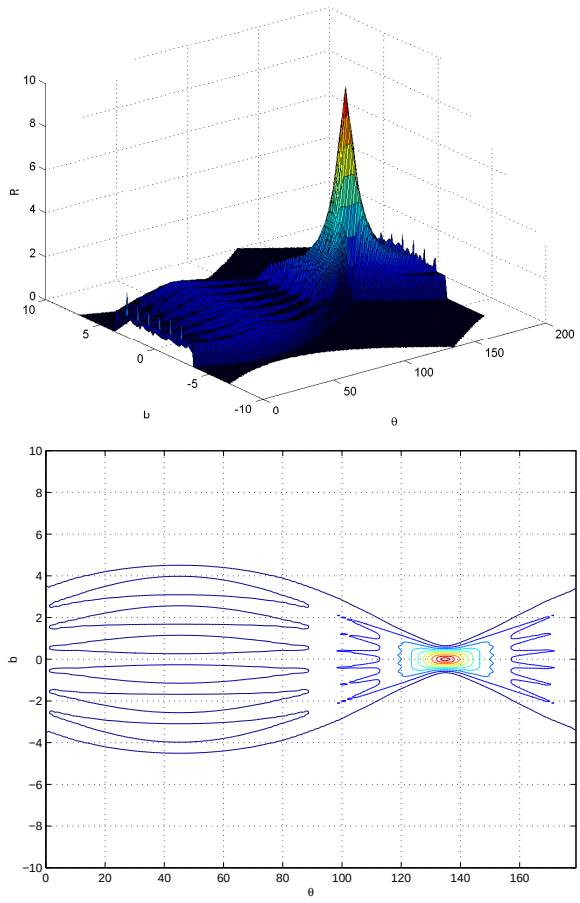


Figure 3.4: Surface (top) and contour (bottom) plots of the Radon transform of the indicator function of pixelated line $\boldsymbol{l}_p$ with $\{(p_{ix}, p_{iy}) \,|\, p_{ix} = p_{iy} = p, p \in \{-3, \ldots, 3\}\}$ and $w_i = h_i = 1, i = 1, \ldots, 7$.

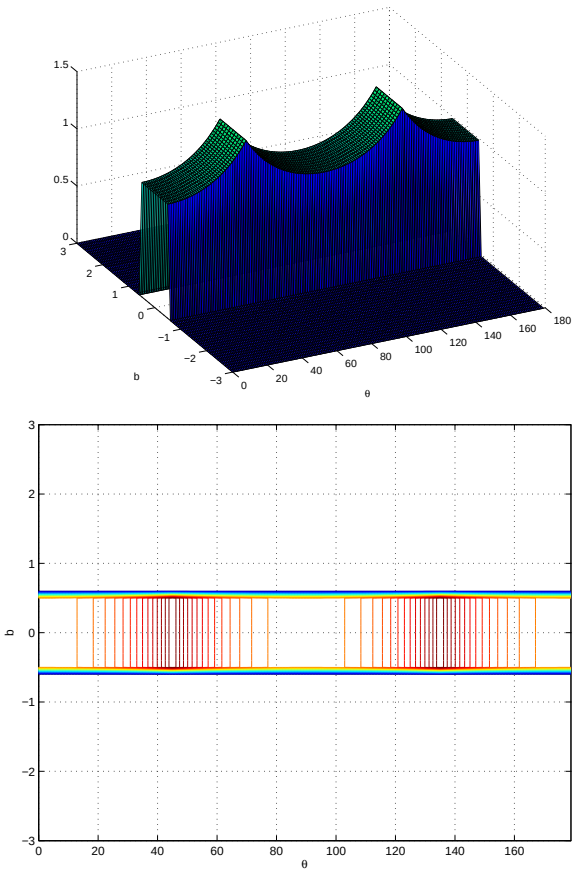


Figure 3.5: Surface (top) and contour (bottom) plots of separable approximation to the Radon transform of the pixel indicator function of pixel $\boldsymbol{p}_0$ when $w = h = 1$.

Figure 3.5 presents surface and contour plots of the approximation for $\boldsymbol{p}_0 = (0, 0, 1, 1)$. It can be seen, by comparing with Figure 2.2, that (3.12) disregards the dependence of $\mathcal{R}\{\mathcal{P}[\boldsymbol{p}_0]\}(b, \boldsymbol{\xi})$ on $b$ in the region where $\frac{1}{2}|w|\cos\theta| - h\sin\theta| < |b| < \frac{1}{2}|w|\cos\theta| - h\sin\theta|$.

**Lemma 3.3.** *Under the separable approximation, the Radon transform of the indicator function of the pixelated line $\boldsymbol{l}_p$ associated with line $\boldsymbol{l}$ is*

$$\tilde{\mathcal{R}}\{\mathcal{X}[\boldsymbol{l}_p](\boldsymbol{x})\}(b, \boldsymbol{\xi}) = \mathcal{R}\{\mathcal{P}[\boldsymbol{p}_0](\boldsymbol{x})\}(0, \boldsymbol{\xi}) \times \mathcal{H}\{\mathcal{X}[\boldsymbol{l}_p](\boldsymbol{x})\}(b, \boldsymbol{\xi}) \tag{3.14}$$

*where, denoting by $\boldsymbol{l}'$ the line parameterized by $(b, \boldsymbol{\xi})$,*

$$\mathcal{H}\{\mathcal{X}[\boldsymbol{l}_p](\boldsymbol{x})\}(b, \boldsymbol{\xi}) = \#\{i \,|\, \boldsymbol{p}_i \in \mathcal{PS}(\boldsymbol{l}) \;\; \textit{and} \;\; \boldsymbol{p}_i \in \mathcal{PS}(\boldsymbol{l}')\} \tag{3.15}$$

*is the Hough transform of $\mathcal{X}[\boldsymbol{l}_p](\boldsymbol{x})$.*

*Proof:* Replacing $\mathcal{R}\{\mathcal{P}[\boldsymbol{l}_0](\boldsymbol{x})\}(b, \boldsymbol{\xi})$ with $\tilde{\mathcal{R}}\{\mathcal{P}[\boldsymbol{l}_0](\boldsymbol{x})\}(b, \boldsymbol{\xi})$ in (3.11) leads to

$$\begin{aligned}
\tilde{\mathcal{R}}\{\mathcal{X}[\boldsymbol{l}_p](\boldsymbol{x})\}(b, \boldsymbol{\xi}) &= \sum_{i \,|\, \boldsymbol{p}_i \in \mathcal{PS}(\boldsymbol{l})} \mathcal{R}\{\mathcal{P}[\boldsymbol{p}_0](\boldsymbol{x})\}(0, \boldsymbol{\xi}) \times \mathbf{1}_{\left\{|b - (p_{ix}, p_{iy})\cdot\boldsymbol{\xi}| \le \min(\frac{w}{2}, \frac{h}{2})\right\}} \\
&= \mathcal{R}\{\mathcal{P}[\boldsymbol{p}_0](\boldsymbol{x})\}(0, \boldsymbol{\xi}) \sum_{i \,|\, \boldsymbol{p}_i \in \mathcal{PS}(\boldsymbol{l})} \mathbf{1}_{\left\{|b - (p_{ix}, p_{iy})\cdot\boldsymbol{\xi}| \le \min(\frac{w}{2}, \frac{h}{2})\right\}}.
\end{aligned}$$

Noticing that $|b - (p_{ix}, p_{iy}) \cdot \boldsymbol{\xi}|$ is the distance from the point $(p_{ix}, p_{iy})$ to the line $\boldsymbol{l}'$, it follows from (2.23) that

$$\mathbf{1}_{\left\{|b - (p_{ix}, p_{iy})\cdot\boldsymbol{\xi}| \le \min(\frac{w}{2}, \frac{h}{2})\right\}} = \begin{cases} 1 & \text{if} \mathcal{S}(\boldsymbol{p}_i) \cap \mathcal{S}(\boldsymbol{l}') \neq \emptyset \\ 0 & \text{otherwise.} \end{cases}$$

Hence, the summation is equal to the number of pixels $\boldsymbol{p}_i$ that belong to both the pixel sets of $\boldsymbol{l}_p$ and $\boldsymbol{l}'$. ∎

## 3.4 Pixelated edge maps

We next introduce the edge indicator function, which divides the set of lines supported by $\mathcal{L}_{w,h}$ into two subsets: the set of edges and the set of non-edges.

**Definition 3.5.** An *edge indicator function* on a lattice $\mathcal{L}_{w,h}$ is a mapping

$$\mathcal{E} : \mathcal{SL}_{w,h} \to \{0, 1\}.$$

A line $\boldsymbol{l} \in \mathcal{SL}_{w,h}$ is said to be an *edge* if $\mathcal{E}(\boldsymbol{l}) = 1$ and a *non-edge* otherwise. The set of all lines classified as edges is denoted by $\mathcal{E}^{-1}(1)$. The pixelated line $\boldsymbol{l}_p$ associated with an edge $\boldsymbol{l}$ is denoted as a *pixelated edge*.

A pixelated edge map is the binary sum of the indicator functions of all pixelated edges.

**Definition 3.6.** The *pixelated edge map* of an edge indicator function $\mathcal{E}$ is the mapping

$$\mathcal{EM}[\mathcal{E}](\boldsymbol{x}) = \bigcup_{i|\boldsymbol{l}_i \in \mathcal{SL}_{w,h}} \mathcal{E}(\boldsymbol{l}_i)\mathcal{X}[(\boldsymbol{l}_i)_p](\boldsymbol{x}). \tag{3.16}$$

The following theorem shows that the Radon transform of $\mathcal{EM}[\mathcal{E}](\mathbf{x})$ is the sum of the modulations of the Radon transform of $\mathcal{P}[\boldsymbol{p}_0]$ by all sinusoids associated with pixels belonging to the pixelated edges defined by $\mathcal{E}$.

**Theorem 3.3.** *The Radon transform of the pixelated edge map of an edge indicator function $\mathcal{E}$ is*

$$\mathcal{R}\{\mathcal{EM}[\mathcal{E}](\boldsymbol{x})\}(b,\boldsymbol{\xi}) = \sum_{i\,|\,\boldsymbol{p}_i \in \mathcal{PS}(\mathcal{E}^{-1}(1))} \mathcal{R}\{\mathcal{P}[\boldsymbol{p}_0](\boldsymbol{x})\}(b - (p_{ix}, p_{iy})\cdot\boldsymbol{\xi}, \boldsymbol{\xi}) \tag{3.17}$$

*where $\mathcal{PS}(\mathcal{E}^{-1}(1)) = \left\{\boldsymbol{p}_i \,\middle|\, \exists\, \boldsymbol{l}_k \in \mathcal{E}^{-1}(1)$ such that $\boldsymbol{p}_i \in \mathcal{PS}(\boldsymbol{l}_k)\right\}$, and $\mathcal{R}\{\mathcal{P}[\boldsymbol{p}_0](\boldsymbol{x})\}(b,\boldsymbol{\xi})$ is defined by (2.27).*

*Proof:* From (3.4) and (3.16) it follows that

$$\mathcal{EM}[\mathcal{E}](\boldsymbol{x}) = \bigcup_{k|\boldsymbol{l}_k \in \mathcal{SL}_{w,h}} \mathcal{E}(\boldsymbol{l}_k) \sum_{i|\boldsymbol{p}_i \in \mathcal{PS}(\boldsymbol{l}_k)} \mathcal{P}[\boldsymbol{p}_i](\boldsymbol{x})$$

and therefore, for $\boldsymbol{x}_0 \in \mathcal{S}(\boldsymbol{p}_l)$, $\mathcal{EM}[\mathcal{E}](\boldsymbol{x}_0) = 1$ if and only if $\boldsymbol{p}_l \in \mathcal{PS}(\boldsymbol{l}_k)$ and $\boldsymbol{l}_k \in \mathcal{E}^{-1}(1)$. This is equivalent to $\mathcal{EM}[\mathcal{E}](\boldsymbol{x}_0) = f(\boldsymbol{p}_l)$, where

$$f(\boldsymbol{p}_l) = \begin{cases} 1 & \text{if } \boldsymbol{p}_l \in \mathcal{PS}(\mathcal{E}^{-1}(1)) \\ 0 & \text{otherwise.} \end{cases}$$

Hence,

$$\mathcal{EM}[\mathcal{E}](\boldsymbol{x}) = \sum_{i|\boldsymbol{p}_i \in \mathcal{L}_{w,h}} f(\boldsymbol{p}_i)\mathcal{P}[\boldsymbol{p}_i](\boldsymbol{x})$$

is a pixelated function and the theorem follows from Theorem 2.5. ∎

Once again, the separable approximation can be used to relate the Radon and Hough transforms of $\mathcal{EM}[\mathcal{E}](\mathbf{x})$.

**Corollary 3.3.** *Under the separable approximation, the Radon transform of the pixelated edge map of an edge indicator function $\mathcal{E}$ is*

$$\tilde{\mathcal{R}}\{\mathcal{EM}[\mathcal{E}](\boldsymbol{x})\}(b,\boldsymbol{\xi}) = \mathcal{R}\{\mathcal{P}[\boldsymbol{p}_0](\boldsymbol{x})\}(0,\boldsymbol{\xi}) \times \mathcal{H}\{\mathcal{EM}[\mathcal{E}](\boldsymbol{x})\}(b,\boldsymbol{\xi}) \tag{3.18}$$

*where, denoting by* $\boldsymbol{l}'$ *the line parameterized by* $(b, \boldsymbol{\xi})$,

$$\mathcal{H}\{\mathcal{EM}[\mathcal{E}](\boldsymbol{x})\}(b, \boldsymbol{\xi}) = \#\{i \,|\, \boldsymbol{p}_i \in \mathcal{PS}(\mathcal{E}^{-1}(1)) \text{ and } \boldsymbol{p}_i \in \mathcal{PS}(\boldsymbol{l}')\} \tag{3.19}$$

*is the Hough transform of* $\mathcal{EM}[\mathcal{E}](\boldsymbol{x})$.

*Proof:* The proof is identical to that of Lemma 3.3. ∎

# Chapter 4

# Bounded lattices and the discrete Radon transform

In this chapter, we consider restrictions of the pixel lattice $\mathcal{L}_{w,h}$ to finite subsets, and introduce the object of major interest for this thesis: the image. We start by considering the effects of sampling the Radon transform (by computing its values over a finite subset of the possible parameterizations), which leads to the definition of the discrete Radon transform. We then study various sets that will be of great interest in subsequent chapters: the admissible set of an image (the set of lines that are supported by the image), and the intersecting sets of the restrictions to the image of a line (which we denote by line segment), a strip (strip segment), and a pixelated line. These are the sets of all lines whose support set has non-empty intersection with the support set of the line segment, strip segment, and pixelated line, respectively. We derive a closed-form expression for the first and tight lower- and upper-bounds for the other two.

## 4.1 The discrete Radon transform

So far we have assumed that 1) the lattice $\mathcal{L}_{w,h}$ is unbounded and 2) the variables $(b, \boldsymbol{\xi})$ can take any value in $\mathbb{R} \times \mathbb{S}$. In the context of this thesis, we are interested in applications of the Radon transform to image processing. This imposes two restrictions. First, because images are finite collections of pixels, we need to consider finite subsets of the lattice $\mathcal{L}_{w,h}$.

**Definition 4.1.** The subset of $\mathcal{L}_{w,h}$ such that

$$-\frac{M}{2} \leq m \leq \frac{M}{2} \text{ and } -\frac{N}{2} \leq n \leq \frac{N}{2} \tag{4.1}$$

is denoted by $\mathcal{L}_{w,h}^{M,N}$ and referred to as the *lattice* of size $(N+1)(M+1)$. The associated collection of pixels is referred to as the *image* of size $(N+1)(M+1)$ and denoted by $\mathcal{I}_{w,h}^{M,N}$

$$\mathcal{I}_{w,h}^{M,N} = [-x_{max}, x_{max}] \times [-y_{max}, y_{max}], \tag{4.2}$$

where

$$x_{max} = \left( \left\lfloor \frac{M}{2} \right\rfloor + \frac{1}{2} \right) w \quad \text{and} \quad y_{max} = \left( \left\lfloor \frac{N}{2} \right\rfloor + \frac{1}{2} \right) h. \tag{4.3}$$

**Remark 4.1.** Definitions 3.5 and 3.6 imply that edges have infinite length and no gaps. In the context of image analysis, this is sensible as long as the analysis is local, i.e. the size of the image region under analysis is smaller than the minimum length of image edge segments. To account for this situation we will consider, in subsequent chapters, sub-images associated with subsets of $\mathcal{L}_{w,h}^{M,N}$. We will, however, rely on the same notation to refer to the image and its sub-image lattices.

Second, it is impossible to compute the Radon transform for all possible line parameterizations. The computation is consequently restricted to a lattice of $(P+1)(Q+1)$ points

$$\mathcal{L}_{b_s,\theta_s}^{PQ} = \left\{ (b,\theta) \in \mathbb{R} \times \Theta \,\middle|\, (b,\theta) = p\, b_s\, \mathbf{e}_b + q\, \theta_s \mathbf{e}_\theta, -\frac{P}{2} \leq p \leq \frac{P}{2}, -\frac{Q}{2} \leq q \leq \frac{Q}{2} \right\},$$

where $\mathbf{e}_b = (1,0)$ and $\mathbf{e}_\theta = (0,1)$. Following the standard practice in signal processing, we rely on a uniform sampling of the $b$ and $\theta$ with

$$\theta_s = \frac{\pi}{Q} \text{ and } b_s = \frac{\sqrt{M^2+N^2}}{P}. \tag{4.4}$$

The restriction of the Radon transform to the set of mappings from pixelated functions defined on $\mathcal{L}_{w,h}^{M,N}$ to functions with domain $\mathcal{L}_{b_s,\theta_s}^{P,Q}$ is the discrete Radon transform.

**Definition 4.2.** Given a pixel lattice $\mathcal{L}_{w,h}^{M,N}$ and a parameter lattice $\mathcal{L}_{b_s,\theta_s}^{P,Q}$, the *2D discrete Radon transform* (DRT) of a pixelated function defined on $\mathcal{L}_{w,h}^{M,N}$ is the mapping

$$\mathcal{R} : \mathcal{PFL}_{w,h}^{M,N} \to \mathbb{R}^{\mathcal{L}_{b_s,\theta_s}^{P,Q}}$$

$$\mathcal{R}_d[f_p(\boldsymbol{x})](b_k, \boldsymbol{\xi}_k) = \sum_{i \,|\, \boldsymbol{p}_i \in \mathcal{L}_{w,h}^{M,N}} f(\boldsymbol{p}_i) \mathcal{R}\{\mathcal{P}[\boldsymbol{p}_0](\boldsymbol{x})\} \left(b_k - (p_{ix}, p_{iy}) \cdot \boldsymbol{\xi}_k, \boldsymbol{\xi}_k\right), \tag{4.5}$$

where $\mathcal{PFL}_{w,h}^{M,N}$ is the set of pixelated functions defined on $\mathcal{L}_{w,h}^{M,N}$, $\mathcal{R}\{\mathcal{P}[\boldsymbol{p}_0](\boldsymbol{x})\}(b, \boldsymbol{\xi})$ is given by (2.27), $\boldsymbol{\xi}_k = (\cos\theta_k, \sin\theta_k)$, and $(b_k, \theta_k) \in \mathcal{L}_{b_s,\theta_s}^{P,Q}$.

It is clear from this definition that the DRT is simply the result of sampling the Radon transform of a pixelated function at the values $(b_k, \boldsymbol{\xi}_k)$, i.e.

$$\mathcal{R}_d[f_p(\boldsymbol{x})](b_k, \boldsymbol{\xi}_k) = \mathcal{R}[f_p(\boldsymbol{x})](b, \boldsymbol{\xi})|_{(b=b_k, \boldsymbol{\xi}=\boldsymbol{\xi}_k)}.$$

Hence, all the results that were previously obtained for the Radon transform are still valid for the DRT. For these reasons, we will drop the $d$ subscript and simply refer to the DRT as $\mathcal{R}[f_p(\boldsymbol{x})](b_k, \boldsymbol{\xi}_k)$.

## 4.2 The intersecting set of a line segment

Among the results of the previous chapters, the most relevant for edge detection is the Radon transform of the pixelated edge map. As shown in Theorem 3.3 and Corollary 3.3, for a given line $\boldsymbol{l}_k = (b_k, \boldsymbol{\xi}_k)$, $\mathcal{R}\{\mathcal{EM}[\mathcal{E}](\boldsymbol{x})\}(\boldsymbol{l}_k)$ is determined by the pixels $\boldsymbol{p}_i$ that simultaneously belong to $\mathcal{PS}(\mathcal{E}^{-1}(1))$ and $\mathcal{PS}(\boldsymbol{l}_k)$. It follows that the only edges which are relevant to $\mathcal{R}\{\mathcal{EM}[\mathcal{E}](\boldsymbol{x})\}(\boldsymbol{l}_k)$ are those that intersect pixels in $\mathcal{PS}(\mathcal{E}^{-1}(1))$. To characterize the set of such edges we start by introducing the set of admissible lines of $\mathcal{I}_{w,h}^{M,N}$.

**Definition 4.3.** The *admissible set* of $\mathcal{I}_{w,h}^{M,N}$ is the set of all lines supported by $\mathcal{I}_{w,h}^{M,N}$.

The following lemma characterizes the admissible set.

**Lemma 4.1.** *The admissible set is the set*

$$\mathcal{A}(x_{max}, y_{max}) = \{(b, \theta) \,\big|\, |b| \leq x_{max}|\cos\theta| + y_{max}|\sin\theta|\}, \tag{4.6}$$

*where $x_{max}$ and $y_{max}$ are given by (4.3).*

*Proof:* Let $\boldsymbol{l} = (b_l, \theta_l)$ be a line supported by $\mathcal{I}_{w,h}^{M,N}$ and consider Figure 4.1 which depicts various lines of angle $\theta_l$ for the following two cases: **i)** $0 \leq \theta_l \leq \frac{\pi}{2}$ and **ii)** $\frac{\pi}{2} \leq \theta_l \leq \pi$. From the definition of support set, the extrema values of $b_l$ that lead to lines supported by $\mathcal{I}_{w,h}^{M,N}$ are those of the lines that contain the corners of $\mathcal{I}_{w,h}^{M,N}$. This means

**i)** the lines that pass through $\pm(x_{max}, y_{max})$,

**ii)** the lines that pass through $\pm(x_{max}, -y_{max})$.

It follows from the line equation that

**i)** $b_l \leq x_{max}\cos\theta_l + y_{max}\sin\theta_l$ and $b_l \geq -x_{max}\cos\theta_l - y_{max}\sin\theta_l$ or equivalently

$$|b_l| \leq x_{max}\cos\theta_l + y_{max}\sin\theta_l.$$

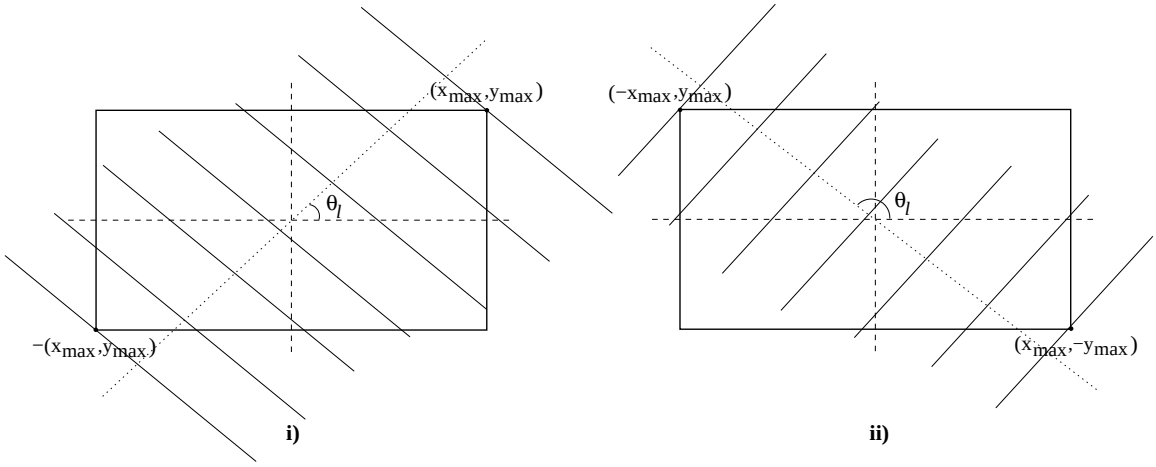


Figure 4.1: Various lines of angle $\theta_l$ for **i)** $0 \leq \theta_l \leq \pi/2$ and **ii)** $\pi/2 \leq \theta_l \leq \pi$.

**ii)** $b_l \leq -x_{max}\cos\theta_l + y_{max}\sin\theta_l$ and $b_l \geq -(-x_{max}\cos\theta_l + y_{max}\sin\theta_l)$ or equivalently

$$|b_l| \leq -x_{max}\cos\theta_l + y_{max}\sin\theta_l.$$

Hence,

$$|b_l| \leq y_{max}|\sin\theta_l| + x_{max}|\cos\theta_l|,$$

and the lemma follows. ∎

**Definition 4.4.** Given a line $\boldsymbol{l} = (b, \boldsymbol{\xi})$ supported by a set $\mathcal{X}$, the *line segment* $\boldsymbol{l}_{|\mathcal{X}}$ associated with $\boldsymbol{l}$ is the restriction of $\boldsymbol{l}$ to $\mathcal{X}$.

One important subset of the admissible set is the intersecting set of a given line segment, which is defined as follows.

**Definition 4.5.** The *intersecting set* of *line segment* $\boldsymbol{l}_{|\mathcal{X}}$ is the set of all lines supported by $\mathcal{X}$ that intersect $\boldsymbol{l}_{|\mathcal{X}}$

$$\mathcal{IS}\left(\boldsymbol{l}_{|\mathcal{X}}\right) = \left\{\boldsymbol{l}' \,\middle|\, \mathcal{S}\left(\boldsymbol{l}_{|\mathcal{X}}\right) \cap \mathcal{S}(\boldsymbol{l}') \neq \emptyset\right\}.$$

In order to characterize this set, we start by introducing a taxonomy for all lines in the admissible set.

**Definition 4.6.** Consider the lines in $\mathcal{A}(x_{max}, y_{max})$. The lines $y = y_{max}$, $y = -y_{max}$,

$x = x_{max}$, and $x = -x_{max}$ are denoted by

$$\begin{aligned} \boldsymbol{h}_l &= (-y_{max}, \pi/2) \\ \boldsymbol{h}_h &= (\ y_{max}, \pi/2) \\ \boldsymbol{v}_l &= (-x_{max},\ \ 0) \\ \boldsymbol{v}_h &= (\ x_{max},\ \ 0). \end{aligned}$$

A line segment associated with a line $\boldsymbol{l} = (b_l, \theta_l) \in \mathcal{A}(x_{max}, y_{max})$ is a *segment of type* I, II, or III if $\boldsymbol{l}$ is an element of the set $\mathcal{R}_{\mathrm{I}}$, $\mathcal{R}_{\mathrm{II}}$, or $\mathcal{R}_{\mathrm{III}}$, respectively, where

$$\mathcal{R}_{\mathrm{I}} = \left\{ \boldsymbol{l} \,\middle|\, \mathcal{S}(\boldsymbol{l}) \cap \mathcal{S}(\boldsymbol{h}_l) \neq \emptyset \text{ and } \mathcal{S}(\boldsymbol{l}) \cap \mathcal{S}(\boldsymbol{h}_h) \neq \emptyset \right\} \tag{4.7}$$

$$\mathcal{R}_{\mathrm{II}} = \left\{ \boldsymbol{l} \,\middle|\, \mathcal{S}(\boldsymbol{l}) \cap \mathcal{S}(\boldsymbol{v}_l) \neq \emptyset \text{ and } \mathcal{S}(\boldsymbol{l}) \cap \mathcal{S}(\boldsymbol{v}_h) \neq \emptyset \right\} \tag{4.8}$$

$$\mathcal{R}_{\mathrm{III}} = \left\{ \boldsymbol{l} \,\middle|\, \boldsymbol{l} \notin \mathcal{R}_{\mathrm{I}} \cup \mathcal{R}_{\mathrm{II}} \right\}. \tag{4.9}$$

The three subsets $\mathcal{R}_{\mathrm{I}}$, $\mathcal{R}_{\mathrm{II}}$, and $\mathcal{R}_{\mathrm{III}}$ partition $\mathcal{A}(x_{max}, y_{max})$ into sets of lines which intersect the horizontal boundaries of $\mathcal{I}_{w,h}^{M,N}$ (type I), the vertical boundaries of $\mathcal{I}_{w,h}^{M,N}$ (type II), and one horizontal and one vertical boundary of $\mathcal{I}_{w,h}^{M,N}$ (type III). They are characterized by the following lemma.

**Lemma 4.2.** *Let $\boldsymbol{l} = (b_l, \theta_l)$ be a line supported by $\mathcal{I}_{w,h}^{M,N}$. Then,*

$$\mathcal{R}_{\mathrm{I}} = \left\{ (b_l, \theta_l) \,\middle|\, |b_l| \leq \left| |x_{max}| \cos\theta_l - y_{max} \sin\theta_l \right|, \theta_l \in [\phi, \pi - \phi] \right\}, \tag{4.10}$$

$$\mathcal{R}_{\mathrm{II}} = \left\{ (b_l, \theta_l) \,\middle|\, |b_l| \leq \left| |x_{max}| \cos\theta_l - y_{max} \sin\theta_l \right|, \theta_l \in [0, \phi] \cup [\pi - \phi, \pi] \right\}, \tag{4.11}$$

$$\mathcal{R}_{\mathrm{III}} = \left\{ (b_l, \theta_l) \,\middle|\, \left| |x_{max}| \cos\theta_l - y_{max} \sin\theta_l \right| \leq |b_l| \leq \left| |x_{max}| \cos\theta_l + y_{max} \sin\theta_l \right| \right\} \tag{4.12}$$

*where*

$$\phi = \arcsin\left(\frac{y_{max}}{D}\right) \quad \textit{and} \quad D = \sqrt{x_{max}^2 + y_{max}^2}. \tag{4.13}$$

*Proof:* Consider $\boldsymbol{l} \in \mathcal{R}_{\mathrm{I}}$. Since $\boldsymbol{l}$ intersects both $\boldsymbol{h}_l$ and $\boldsymbol{h}_h$, $\mathcal{S}(\boldsymbol{l})$ contains two points of the form $(x, y = \pm y_{max})$, $-x_{max} \leq x \leq x_{max}$. It follows, from the line equation, that

$$x = \frac{b_l \mp y_{max} \sin\theta_l}{\cos\theta_l}.$$

and

$$-x_{max} \leq \frac{b_l \mp y_{max} \sin\theta_l}{\cos\theta_l} \leq x_{max},$$

from which

$$\pm y_{max}\sin\theta_l - x_{max}|\cos\theta_l| \leq b_l \leq \pm y_{max}\sin\theta_l + x_{max}|\cos\theta_l|$$

or, equivalently,

$$y_{max}\sin\theta_l - x_{max}|\cos\theta_l| \leq b_l \leq -y_{max}\sin\theta_l + x_{max}|\cos\theta_l|.$$

Hence,

$$|b_l| \leq \left|x_{max}|\cos\theta_l| - y_{max}\sin\theta_l\right|$$

and

$$x_{max}|\cos\theta_l| - y_{max}\sin\theta_l \geq 0 \;\Leftrightarrow\; |\tan\theta_l| \leq \cot\phi \;\Leftrightarrow\; \theta_l \in [\phi, \pi-\phi].$$

Next, consider the case where $\boldsymbol{l} \in \mathcal{R}_{\text{II}}$. In this case, $\boldsymbol{l}$ intersects $\boldsymbol{v}_l$ and $\boldsymbol{v}_h$ and the intersection points are of the form $(x = \pm x_{max}, y), -y_{max} \leq y \leq y_{max}$. Following the procedure above leads to

$$y = \frac{b_l \mp x_{max}\cos\theta_l}{\sin\theta_l}$$

and

$$|b_l| \leq \left|y_{max}\sin\theta_l - x_{max}|\cos\theta_l|\right|$$

with

$$y_{max}\sin\theta_l - x_{max}|\cos\theta_l| \geq 0 \;\Leftrightarrow\; |\tan\theta_l| \geq \cot\phi \;\Leftrightarrow\; \theta_l \in [0, \phi] \cup [\pi-\phi, \pi].$$

Finally, consider the case where $\boldsymbol{l} \in \mathcal{R}_{\text{III}}$. Since $\boldsymbol{l} \notin \mathcal{R}_{\text{I}} \cup \mathcal{R}_{\text{II}}$ and $\mathcal{R}_{\text{III}} \subset \mathcal{A}(x_{max}, y_{max})$, then

$$\left|x_{max}|\cos\theta_l| - y_{max}\sin\theta_l\right| \leq |b_l| \leq \left|x_{max}|\cos\theta_l| + y_{max}\sin\theta_l\right|.$$

■

The intersecting set of $\boldsymbol{l}_{|\mathcal{X}}$ is trivial when $\mathcal{X} = \mathbb{R}^2$: the set of all lines that are not parallel to $\boldsymbol{l}_{|\mathcal{X}}$. However, when $\mathcal{X}$ is a subset of $\mathbb{R}^2$, there may be many lines supported by $\mathcal{X}$ that are not parallel to $\boldsymbol{l}$ and do not intersect $\boldsymbol{l}_{|\mathcal{X}}$. The following lemma characterizes the intersecting set when $\mathcal{X}$ is the image associated with $\mathcal{L}_{w,h}^{M,N}$.

**Theorem 4.1.** *The intersecting set of the line segment* $\boldsymbol{l}_{\left|\mathcal{I}_{w,h}^{M,N}\right.}$, $\boldsymbol{l} = (b_l, \theta_l)$, *is the set*

$$\mathcal{IS}\left(\boldsymbol{l}_{\left|\mathcal{I}_{w,h}^{M,N}\right.}\right) = \{(b,\theta) \,|\, b_{inf}(\theta, b_l, \theta_l) \leq b \leq b_{sup}(\theta, b_l, \theta_l)\}, \tag{4.14}$$

*where*

i)

$$b_{inf}(\theta, b_l, \theta_l) = -x_{max}\left|\frac{\sin(\theta_l - \theta)}{\sin\theta_l}\right| + |b_l|\frac{\sin\theta}{\sin\theta_l} \tag{4.15}$$

$$b_{sup}(\theta, b_l, \theta_l) = x_{max}\left|\frac{\sin(\theta_l - \theta)}{\sin\theta_l}\right| + |b_l|\frac{\sin\theta}{\sin\theta_l} \tag{4.16}$$

$$\textit{if } \boldsymbol{l} \in \mathcal{R}_{\mathsf{I}}. \tag{4.17}$$

ii)

$$b_{inf}(\theta, b_l, \theta_l) = -y_{max}\left|\frac{\sin(\theta_l - \theta)}{\cos\theta_l}\right| + |b_l|\frac{\cos\theta}{\cos\theta_l} \tag{4.18}$$

$$b_{sup}(\theta, b_l, \theta_l) = y_{max}\left|\frac{\sin(\theta_l - \theta)}{\cos\theta_l}\right| + |b_l|\frac{\cos\theta}{\cos\theta_l} \tag{4.19}$$

$$\textit{if } \boldsymbol{l} \in \mathcal{R}_{\mathsf{II}}. \tag{4.20}$$

iii)

$$b_{inf}(\theta, b_l, \theta_l) = -y_{max}\left|\frac{\sin(\theta_l - \theta)}{\cos\theta_l}\right| + |b_l|\frac{\cos\theta}{\cos\theta_l} \tag{4.21}$$

$$b_{sup}(\theta, b_l, \theta_l) = x_{max}\left|\frac{\sin(\theta_l - \theta)}{\sin\theta_l}\right| + |b_l|\frac{\sin\theta}{\sin\theta_l} \tag{4.22}$$

$$\textit{if } \boldsymbol{l} \in \mathcal{R}_{\mathsf{III}} \quad \textit{and} \quad \operatorname{sign}[\sin(\theta_l - \theta)] = \operatorname{sign}[\sin(2\theta_l)]. \tag{4.23}$$

iv)

$$b_{inf}(\theta, b_l, \theta_l) = -x_{max}\left|\frac{\sin(\theta_l - \theta)}{\sin\theta_l}\right| + |b_l|\frac{\sin\theta}{\sin\theta_l} \tag{4.24}$$

$$b_{sup}(\theta, b_l, \theta_l) = y_{max}\left|\frac{\sin(\theta_l - \theta)}{\cos\theta_l}\right| + |b_l|\frac{\cos\theta}{\cos\theta_l} \tag{4.25}$$

$$\textit{if } \boldsymbol{l} \in \mathcal{R}_{\mathsf{III}} \quad \textit{and} \quad \operatorname{sign}[\sin(\theta_l - \theta)] = -\operatorname{sign}[\sin(2\theta_l)]. \tag{4.26}$$

*Proof:* Consider a line $\boldsymbol{l}' = (b, \theta)$ that intersects $\boldsymbol{l} = (b_l, \theta_l)$ at the point $(x, y)$ as illustrated by Figure 4.2. From (2.1),

$$\begin{bmatrix} b_l \\ b \end{bmatrix} = \begin{bmatrix} \cos\theta_l & \sin\theta_l \\ \cos\theta & \sin\theta \end{bmatrix} \begin{bmatrix} x \\ y \end{bmatrix}$$

and, for $\theta_l \neq \theta$,

$$x = b_l\frac{\sin\theta}{\sin(\theta_l - \theta)} - b\frac{\sin\theta_l}{\sin(\theta_l - \theta)}$$

$$y = -b_l\frac{\cos\theta}{\sin(\theta_l - \theta)} + b\frac{\cos\theta_l}{\sin(\theta_l - \theta)}.$$

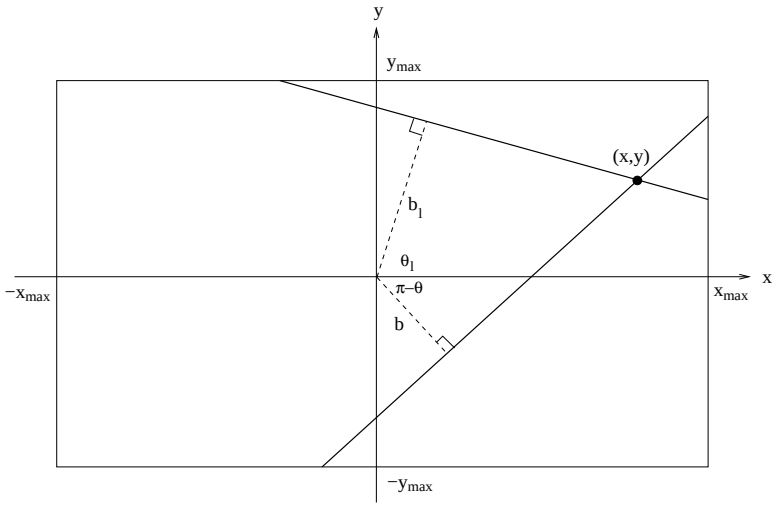


Figure 4.2: Two intersecting lines with parameterizations $(b, \theta)$ and $(b_l, \theta_l)$ that intersect at a point $(x, y)$.

Since the $\mathcal{I}_{w,h}^{M,N}$ is bounded, the intersection point must satisfy the constraints (see Figure 4.2)

$$-x_{max} \le x \le x_{max}$$

$$-y_{max} \le y \le y_{max},$$

where $x_{max}$ and $y_{max}$ are given by (4.3). After some algebraic manipulation, this leads to

$$-x_{max}\left|\frac{\sin(\theta_l-\theta)}{\sin\theta_l}\right| + |b_l|\frac{\sin\theta}{\sin\theta_l} \le \quad b \quad \le x_{max}\left|\frac{\sin(\theta_l-\theta)}{\sin\theta_l}\right| + |b_l|\frac{\sin\theta}{\sin\theta_l} \tag{4.27}$$

$$-y_{max}\left|\frac{\sin(\theta_l-\theta)}{\cos\theta_l}\right| + |b_l|\frac{\cos\theta}{\cos\theta_l} \le \quad b \quad \le y_{max}\left|\frac{\sin(\theta_l-\theta)}{\cos\theta_l}\right| + |b_l|\frac{\cos\theta}{\cos\theta_l}. \tag{4.28}$$

Let

$$\mathsf{A} = -x_{max}\left|\frac{\sin(\theta_l-\theta)}{\sin\theta_l}\right| + |b_l|\frac{\sin\theta}{\sin\theta_l} \qquad \mathsf{C} = x_{max}\left|\frac{\sin(\theta_l-\theta)}{\sin\theta_l}\right| + |b_l|\frac{\sin\theta}{\sin\theta_l}$$

$$\mathsf{B} = -y_{max}\left|\frac{\sin(\theta_l-\theta)}{\cos\theta_l}\right| + |b_l|\frac{\cos\theta}{\cos\theta_l} \qquad \mathsf{D} = y_{max}\left|\frac{\sin(\theta_l-\theta)}{\cos\theta_l}\right| + |b_l|\frac{\cos\theta}{\cos\theta_l}.$$

Then, $\mathsf{A} > \mathsf{B}$ if and only if

$$\begin{aligned} & |\sin(\theta_l-\theta)|\left(\frac{y_{max}}{|\cos\theta_l|} - \frac{x_{max}}{|\sin\theta_l|}\right) \ge |b_l|\frac{\cos\theta\sin\theta_l - \sin\theta\cos\theta_l}{\sin\theta_l\cos\theta_l} \\ \Leftrightarrow \quad & \frac{y_{max}|\sin\theta_l| - x_{max}|\cos\theta_l|}{2|\cos\theta_l\sin\theta_l|} \ge |b_l|\frac{1}{\sin(2\theta_l)}\text{sign}[\sin(\theta_l-\theta)] \\ \Leftrightarrow \quad & y_{max}|\sin\theta_l| - x_{max}|\cos\theta_l| \ge |b_l|\,\text{sign}[\sin(2\theta_l)]\,\text{sign}[\sin(\theta_l-\theta)], \end{aligned}$$

which is equivalent to

$$b_l \geq 0 \quad \text{and} \quad \frac{y_{max}|\sin\theta_l| - x_{max}|\cos\theta_l|}{|b_l|} \geq \text{sign}\left[\frac{\sin(\theta_l - \theta)}{\sin(2\theta_l)}\right] \tag{4.29}$$

or

$$b_l \leq 0 \quad \text{and} \quad \frac{y_{max}|\sin\theta_l| - x_{max}|\cos\theta_l|}{|b_l|} \leq \text{sign}\left[\frac{\sin(\theta_l - \theta)}{\sin(2\theta_l)}\right]. \tag{4.30}$$

Similarly, $\mathsf{C} < \mathsf{D}$ if and only if

$$b_l \geq 0 \quad \text{and} \quad \frac{y_{max}|\sin\theta_l| - x_{max}|\cos\theta_l|}{|b_l|} \leq -\text{sign}\left[\frac{\sin(\theta_l - \theta)}{\sin(2\theta_l)}\right] \tag{4.31}$$

or

$$b_l \leq 0 \quad \text{and} \quad \frac{y_{max}|\sin\theta_l| - x_{max}|\cos\theta_l|}{|b_l|} \geq -\text{sign}\left[\frac{\sin(\theta_l - \theta)}{\sin(2\theta_l)}\right]. \tag{4.32}$$

Therefore, four different cases must be considered.

**i)** $\mathsf{A} > \mathsf{B}$ and $\mathsf{C} < \mathsf{D}$, which implies that $\mathsf{A} \leq b \leq \mathsf{C}$ and, using (4.27), leads to (4.15) and (4.16). Combining (4.29), (4.30), (4.31), and (4.32),

$$b_l \geq 0 \quad \text{and} \quad \frac{y_{max}|\sin\theta_l| - x_{max}|\cos\theta_l|}{|b_l|} \geq 0 \quad \text{and} \quad \left|\frac{y_{max}|\sin\theta_l| - x_{max}|\cos\theta_l|}{b_l}\right| > 1, \tag{4.33}$$

or

$$b_l \leq 0 \quad \text{and} \quad \frac{y_{max}|\sin\theta_l| - x_{max}|\cos\theta_l|}{|b_l|} \leq 0 \quad \text{and} \quad \left|\frac{y_{max}|\sin\theta_l| - x_{max}|\cos\theta_l|}{b_l}\right| > 1. \tag{4.34}$$

Noticing that if $b_l \geq 0$ and $\frac{y_{max}|\sin\theta_l| - x_{max}|\cos\theta_l|}{|b_l|} \geq 0$ or if $b_l \leq 0$ and $\frac{y_{max}|\sin\theta_l| - x_{max}|\cos\theta_l|}{|b_l|} \leq 0$,

$$y_{max}|\sin\theta_l| \geq x_{max}|\cos\theta_l| \Leftrightarrow |\tan\theta_l| \geq \frac{x_{max}}{y_{max}} = \cot\phi, \tag{4.35}$$

(4.17) follows from (4.33), (4.34), and (4.35).

**ii)** $\mathsf{A} < \mathsf{B}$ and $\mathsf{C} > \mathsf{D}$, which implies that $\mathsf{B} \leq b \leq \mathsf{D}$. (4.18), (4.19), and (4.20) follow in a way similar to case **i)**.

**iii)** $\mathsf{A} < \mathsf{B}$ and $\mathsf{C} < \mathsf{D}$, which implies that $\mathsf{B} \leq b \leq \mathsf{C}$ and, using (4.27) and (4.28), leads to (4.21) and (4.22). Also, from (4.29) to (4.32) and after reversal of the appropriate inequalities ($\mathsf{A} < \mathsf{B}$ instead of $\mathsf{A} > \mathsf{B}$),

$$-\left|\frac{y_{max}|\sin\theta_l| - x_{max}|\cos\theta_l|}{b_l}\right| \geq \text{sign}\left[\frac{\sin(\theta_l - \theta)}{\sin(2\theta_l)}\right]$$

or, equivalently,

$$\text{sign}\left[\frac{\sin(\theta_l - \theta)}{\sin(2\theta_l)}\right] = -1 \quad \text{and} \quad \left|\frac{y_{max}|\sin\theta_l| - x_{max}|\cos\theta_l|}{b_l}\right| \leq 1.$$

On the other hand, $b_l$ must be supported by $\mathcal{I}_{w,h}^{M,N}$. Combining (4.2) with Lemma (4.1), leads to (4.23).

**iv)** $\mathsf{A} > \mathsf{B}$ and $\mathsf{C} > \mathsf{D}$, which implies that $\mathsf{A} \leq b \leq \mathsf{D}$. (4.24), (4.25), and (4.26) follow in a way similar to case **iii)**. ∎

## 4.3 The intersecting set of a pixelated line

We next consider the intersecting set of a pixelated line.

**Definition 4.7.** Consider the pixelated line $\boldsymbol{l}_p$ associated with the line $\boldsymbol{l} = (b_l, \theta_l)$ supported by $\mathcal{L}_{w,h}^{M,N}$. The *intersecting set* of $\boldsymbol{l}_p$ on $\mathcal{I}_{w,h}^{M,N}$ is the set of all lines supported by $\mathcal{I}_{w,h}^{M,N}$ that intersect the restriction of $\boldsymbol{l}_p$ to $\mathcal{I}_{w,h}^{M,N}$

$$\mathcal{IS}\left(\boldsymbol{l}_p\big|_{\mathcal{I}_{w,h}^{M,N}}\right) = \left\{\boldsymbol{l}' \,\middle|\, \mathcal{S}\left(\boldsymbol{l}_p\big|_{\mathcal{I}_{w,h}^{M,N}}\right) \cap \mathcal{S}(\boldsymbol{l}') \neq \emptyset\right\}. \tag{4.36}$$

Due to the effects of pixelization, the intersecting set of a pixelated line cannot, in general, be described by a simple closed-form expression. It is, however, possible to derive tight lower- and upper-bounds.

**Theorem 4.2.** *If $\boldsymbol{l}_p$ is the pixelated line associated with line $\boldsymbol{l} = (b_l, \theta_l)$, then the intersecting set of $\boldsymbol{l}_p$, $\mathcal{IS}\left(\boldsymbol{l}_p\big|_{\mathcal{I}_{w,h}^{M,N}}\right)$, satisfies the following relationships*

$$\mathcal{IS}\left(\boldsymbol{l}\big|_{\mathcal{I}_{w,h}^{M,N}}\right) \subset \mathcal{IS}\left(\boldsymbol{l}_p\big|_{\mathcal{I}_{w,h}^{M,N}}\right) \subset \Delta_{w,h}\left[\mathcal{IS}\left(\boldsymbol{l}\big|_{\mathcal{I}_{w,h}^{M,N}}\right)\right], \tag{4.37}$$

*where $\mathcal{IS}\left(\boldsymbol{l}\big|_{\mathcal{I}_{w,h}^{M,N}}\right)$ is the intersecting set of $\boldsymbol{l}\big|_{\mathcal{I}_{w,h}^{M,N}}$, as given by Theorem 4.1, and*

$$\Delta_{w,h}\left[\mathcal{IS}\left(\boldsymbol{l}\big|_{\mathcal{I}_{w,h}^{M,N}}\right)\right] = \left\{(b,\theta) \,\middle|\, b_{inf}(\theta,\boldsymbol{l}) - \sqrt{w^2+h^2} \leq b \leq b_{sup}(\theta,\boldsymbol{l}) + \sqrt{w^2+h^2}\right\}, \tag{4.38}$$

*where $b_{inf}(\cdot)$ and $b_{sup}(\cdot)$ are as defined in Theorem 4.1.*

*Proof:* Consider any line $\boldsymbol{l}'$ supported by $\mathcal{I}_{w,h}^{M,N}$ such that $\boldsymbol{l}' \in \mathcal{IS}\left(\boldsymbol{l}\big|_{\mathcal{I}_{w,h}^{M,N}}\right)$. From (4.14), $\mathcal{S}(\boldsymbol{l}') \cap \mathcal{S}(\boldsymbol{l}) \neq \emptyset$ and, since $\mathcal{S}(\boldsymbol{l}) \subset \mathcal{S}(\boldsymbol{l}_p)$, it follows that $\mathcal{S}(\boldsymbol{l}') \cap \mathcal{S}(\boldsymbol{l}_p) \neq \emptyset$. Hence, $\boldsymbol{l}' \in \mathcal{IS}\left(\boldsymbol{l}_p\big|_{\mathcal{I}_{w,h}^{M,N}}\right)$ from which it follows that $\mathcal{IS}\left(\boldsymbol{l}\big|_{\mathcal{I}_{w,h}^{M,N}}\right) \subset \mathcal{IS}\left(\boldsymbol{l}_p\big|_{\mathcal{I}_{w,h}^{M,N}}\right)$. Next, consider any line $\boldsymbol{l}' = (b,\theta)$ supported by $\mathcal{I}_{w,h}^{M,N}$ such that $\boldsymbol{l}' \in \mathcal{IS}\left(\boldsymbol{l}_p\big|_{\mathcal{I}_{w,h}^{M,N}}\right)$ and note that, from (4.36), there is at least one pixel $\boldsymbol{p} \in \boldsymbol{l}_p$ such that $\mathcal{S}(\boldsymbol{l}') \cap \mathcal{S}(\boldsymbol{p}) \neq \emptyset$. Since, from (3.2), $\mathcal{S}(\boldsymbol{l}) \cap \mathcal{S}(\boldsymbol{p}) \neq \emptyset$,

it is always possible to find a line $\boldsymbol{l}'' = (b', \theta)$ parallel to $\boldsymbol{l}'$ which intersects both $\mathcal{S}(\boldsymbol{l})$ and $\mathcal{S}(\boldsymbol{p})$, i.e.

$$\exists\, \boldsymbol{l}'' = (b', \theta) \in \mathcal{IS}\left(\boldsymbol{l}_{\left|_{\mathcal{I}_{w,h}^{M,N}}\right.}\right) \text{ such that } \mathcal{S}(\boldsymbol{l}'') \cap \mathcal{S}(\boldsymbol{p}) \neq \emptyset.$$

Since $\mathcal{S}(\boldsymbol{p})$ is a rectangle with sides of length $w$ and $h$, it follows that $|b - b'| \leq \sqrt{w^2 + h^2}$ and, from the fact that $b'$ is bounded by (4.14), it follows that $b \in \Delta_{w,h}\left[\mathcal{IS}\left(\boldsymbol{l}_{\left|_{\mathcal{I}_{w,h}^{M,N}}\right.}\right)\right]$. This proves that $\mathcal{IS}\left(\boldsymbol{l}_p{}_{\left|_{\mathcal{I}_{w,h}^{M,N}}\right.}\right) \subset \Delta_{w,h}\left[\mathcal{IS}\left(\boldsymbol{l}_{\left|_{\mathcal{I}_{w,h}^{M,N}}\right.}\right)\right]$. ∎

The following example shows that the upper-bound of (4.37) can be made arbitrarily tight by increasing the size of the lattice.

**Example 4.1.** Consider the lattice $\mathcal{L}_{1,1}^{M,M}$ and the set of lines $\boldsymbol{l}_k = (0, \theta_k)$, where $\theta_k = \frac{\pi}{2} + \arctan\left(1 + \frac{1}{k}\right), k \in \{1, \ldots M\}$, shown in Figure 4.3(a). Since $\frac{\pi}{4} < \theta_k < \frac{\pi}{2}$ for all $k$, the associated pixelated lines all contain the shaded pixel. Noticing that the pixel's upper-left corner has coordinates $\left(-\frac{1}{2}, \frac{3}{2}\right)$, it follows that the set of lines $\boldsymbol{l}'_k$ parallel to $\boldsymbol{l}_k$ that contain the corner point satisfy the equation

$$b'_k = -\frac{1}{2}\cos\theta_k + \frac{3}{2}\sin\theta_k.$$

Denoting by $b_{sup}(\theta_k)$ the supremum of $b$ among all lines parallel to $\boldsymbol{l}_k$ that belong to the intersecting set of the associated pixelated line $(\boldsymbol{l}_k)_p$

$$b_s(\theta_k) = \sup\left\{b \,\middle|\, (b, \theta_k) \in \mathcal{IS}\left((\boldsymbol{l}_k)_p{}_{\left|_{\mathcal{I}_{w,w}^{M,M}}\right.}\right)\right\},$$

if follows that $b_s(\theta_k) = b'_k$. Next we note that, for a line $\boldsymbol{l} = (b, \theta)$, it follows from Theorem 4.1 that $b_{inf}(\boldsymbol{l}, \theta) = b_{sup}(\boldsymbol{l}, \theta) = b$. Since all $\boldsymbol{l}_k$ have $b = 0$, when $\theta' = \theta$, the lower and upper bounds of (4.38) are equal to $\pm\sqrt{2}$. Figure 4.3(b) presents the ratio of $\frac{b_s(\theta_k)}{\sqrt{2}}$ as a function of $k$. Notice how the supremum converges to the upper bound as $k$ increases, showing that the bound is tight. Notice also that, even for relatively small $M$, e.g. $M = 20$ or $M = 40$, the bound provides a good approximation to the supremum.

It is straightforward to show that the ratio between the upper- and lower-bounds of (4.37) converges to one as the lattice size increases. For this, notice from Theorem 4.1 that, given $\boldsymbol{l}$ and $\theta'$, $b_{inf}(\boldsymbol{l}, \theta')$ and $b_{sup}(\boldsymbol{l}, \theta')$ only depend on $M$ and $N$ through $x_{max}$ and $y_{max}$. Since the latter increase linearly with the former, it follows that $b_{inf}(\boldsymbol{l}, \theta')$ and $b_{sup}(\boldsymbol{l}, \theta')$ are monotonically increasing functions of $M$ and $N$. Hence, for constant $w$ and $h$,

$$\lim_{N,M\to\infty} \frac{b_{inf}(\boldsymbol{l}, \theta') - \sqrt{w^2 + h^2}}{b_{inf}(\boldsymbol{l}, \theta')} = \lim_{N,M\to\infty} \frac{b_{sup}(\boldsymbol{l}, \theta') + \sqrt{w^2 + h^2}}{b_{sup}(\boldsymbol{l}, \theta')} = 1.$$

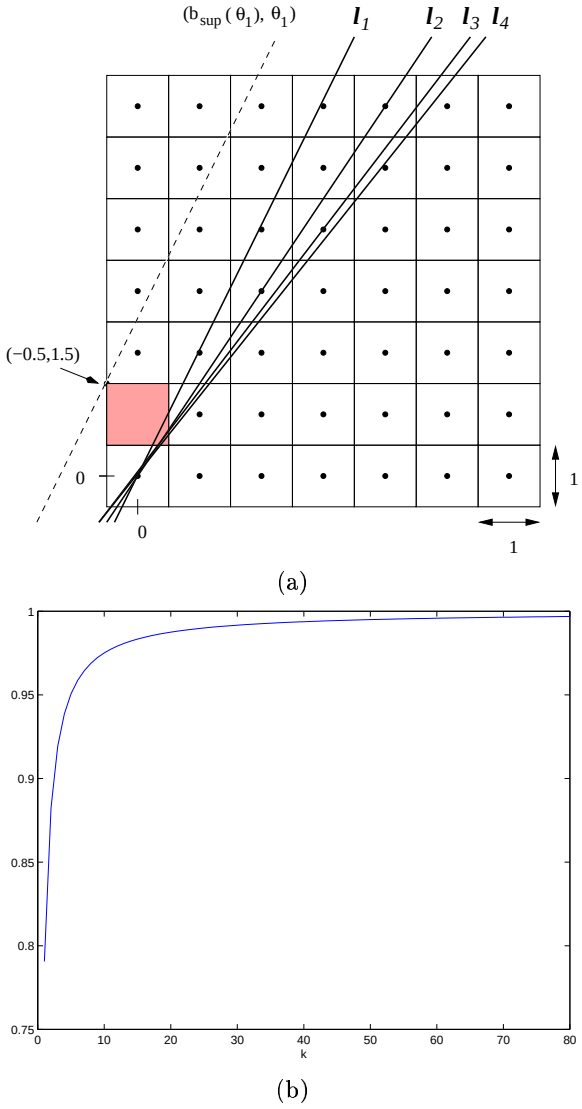


Figure 4.3: The tightness of the upper-bound of (4.37). (a) A collection of lines $\boldsymbol{l}_k$ supported by $\mathcal{L}_{1,1}^{M,M}$, and (b) the ratio between the supremum of $b$ for the intersecting set of each line and the upper-bound given by (4.38) (as a function of $k$).

The next example shows that the bounds are similar even for small values of $N$ and $M$.

**Example 4.2.** Consider the lattice $\mathcal{L}_{1,1}^{M,M}$ and the set of lines $\boldsymbol{l} = (0, \theta)$. Figure 4.4 presents the ratio of the areas of the intersecting sets that bound $\mathcal{IS}\left(\boldsymbol{l}_p|_{\mathcal{I}_{1,1}^{M,M}}\right)$ in (4.37), i.e.

$$R(M) = \frac{\left|\Delta_{w,h}\left[\mathcal{IS}\left(\boldsymbol{l}|_{\mathcal{I}_{1,1}^{M,M}}\right)\right]\right|}{\left|\mathcal{IS}\left(\boldsymbol{l}|_{\mathcal{I}_{1,1}^{M,M}}\right)\right|},$$

as a function of $M$ for $\theta = k\frac{\pi}{16}, k \in \{1, \ldots, 4\}$ (curves corresponding to $\theta$ outside $[0, \frac{\pi}{4}]$ are similar to the ones in this interval and are omitted). Notice that for $M = 40$ the difference between the areas is already smaller than 10% and for $M = 80$ smaller than 5%.

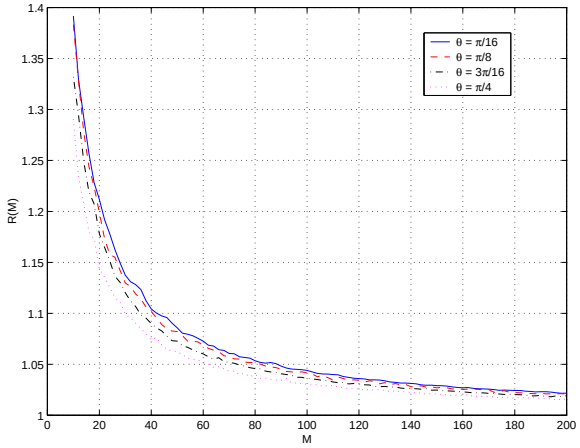


Figure 4.4: Ratio between the areas of the sets that upper- and lower-bound $\mathcal{IS}\left(\boldsymbol{l}_p|_{\mathcal{I}_{1,1}^{M,M}}\right)$, according to (4.37), as a function of the lattice size, for a collection of lines $\boldsymbol{l} = (0, \theta_k), \theta_k \in \left\{\frac{\pi}{16}, \frac{\pi}{8}, 3\frac{\pi}{16}, \frac{\pi}{4}\right\}$.

The results above suggest that, for most values of $M$ and $N$ of practical interest, the intersecting set of the pixelated line $\boldsymbol{l}_p$ is well approximated by the intersecting set of the associated line $\boldsymbol{l}$. This is confirmed by Figure 4.5, where we presents a collection of images containing a pixelated edge, the corresponding Radon transform, and the bounds of Theorem 4.1, for $M = N = 40$. The peak at the center of the Radon transform corresponds to the parameterization of the edge with which the pixelated edge is associated.

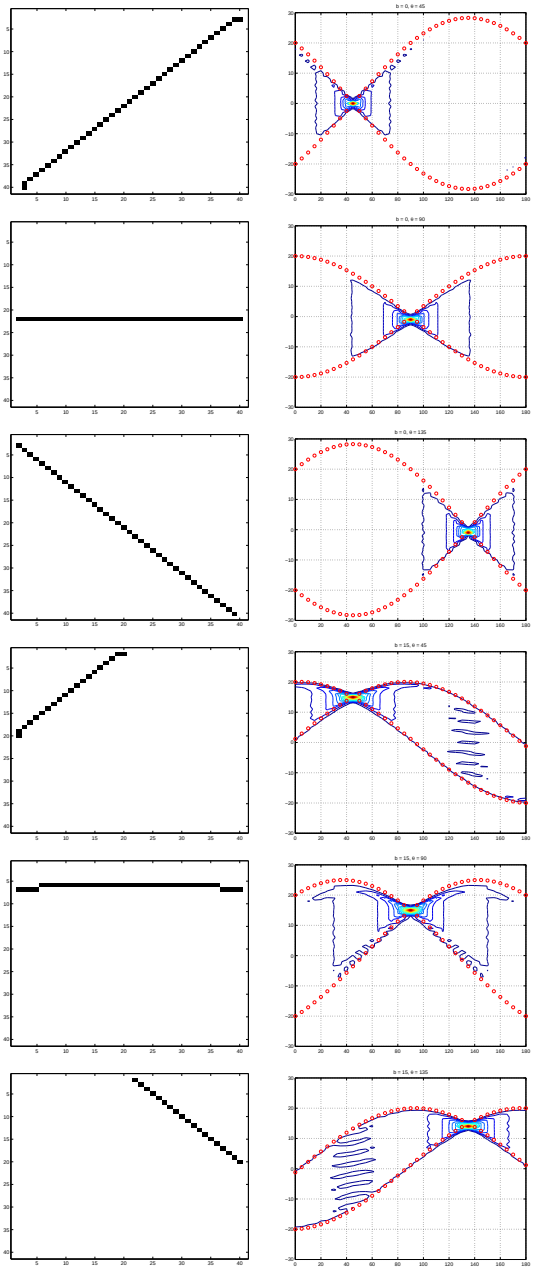

Figure 4.5: A collection of square images containing a pixelated edge (left), and the corresponding isocontours of the amplitude of the Radon transform (right). The circles superimposed on the plots of the Radon transform are the bounds of Theorem 4.1.

## 4.4 The intersecting set of a strip segment

Given the difficulty of deriving a closed-form expression for the intersecting set of a pixelated line it is useful to consider, in addition to this and the intersecting set of the line segment, the intersecting set of the strip segment.

**Definition 4.8.** Given a strip $\boldsymbol{s} = (b, \boldsymbol{\xi}, w)$ supported by a set $\mathcal{X}$, the *strip segment* $\boldsymbol{s}_{|\mathcal{X}}$ is the restriction of $\boldsymbol{s}$ to $\mathcal{X}$.

**Definition 4.9.** The *intersecting set of strip segment* $\boldsymbol{s}_{|\mathcal{X}}$ is the set of all lines supported by $\mathcal{X}$ that intersects $\boldsymbol{s}_{|\mathcal{X}}$

$$\mathcal{IS}(\boldsymbol{s}_{|\mathcal{X}}) = \left\{ \boldsymbol{l}' \,\middle|\, \mathcal{S}(\boldsymbol{s}_{|\mathcal{X}}) \cap \mathcal{S}(\boldsymbol{l}') \neq \emptyset \right\}. \tag{4.39}$$

When $\mathcal{X} = \mathbb{R}^2$, the intersecting set of $\boldsymbol{s}_{|\mathcal{X}}$ is trivial: the set of all lines $\boldsymbol{l}' = (b', \theta')$ that are not parallel to $\boldsymbol{l} = (b, \theta)$ or are parallel but have $|b' - b| \leq \frac{w}{2}$. However, when $\mathcal{X}$ is a subset of $\mathbb{R}^2$, there may be many lines that satisfy these conditions but still do not intersect $\boldsymbol{s}_{|\mathcal{X}}$. We concentrate in the case where $\mathcal{X}$ is the image associated with $\mathcal{L}^{M,N}_{w,h}$, $\mathcal{I}^{M,N}_{w,h}$.

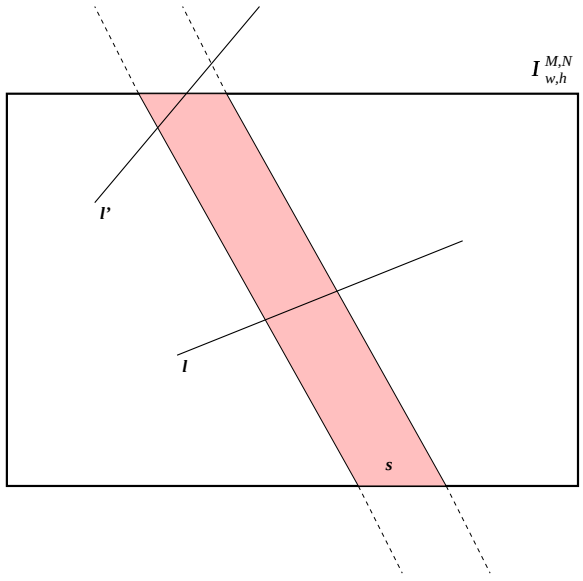


Figure 4.6: Intersection of a line supported in $\mathcal{I}^{M,N}_{w,h}$ and an unbounded strip $\mathbf{s}$: $\boldsymbol{l} \in \mathcal{FIS}\left(\boldsymbol{s}_{|\mathcal{I}^{M,N}_{w,h}}\right)$ and $\boldsymbol{l}' \in \mathcal{PIS}\left(\boldsymbol{s}_{|\mathcal{I}^{M,N}_{w,h}}\right)$.

As illustrated in Figure 4.6, the intersection of a line $\boldsymbol{l}$ supported in $\mathcal{I}_{w,h}^{M,N}$ and an unbounded strip $\boldsymbol{s}$ can be different from the intersection of the line with the restriction of the strip to $\mathcal{I}_{w,h}^{M,N}$. This motivates the sub-division of the intersecting set of a strip segment into two subsets.

**Definition 4.10.** The intersecting set of the strip segment $\boldsymbol{s}_{\big|\mathcal{I}_{w,h}^{M,N}}$ is the union of two sets,

$$\mathcal{IS}\left(\boldsymbol{s}_{\big|\mathcal{I}_{w,h}^{M,N}}\right) = \mathcal{FIS}\left(\boldsymbol{s}_{\big|\mathcal{I}_{w,h}^{M,N}}\right) \bigcup \mathcal{PIS}\left(\boldsymbol{s}_{\big|\mathcal{I}_{w,h}^{M,N}}\right),$$

where

$$\mathcal{FIS}\left(\boldsymbol{s}_{\big|\mathcal{I}_{w,h}^{M,N}}\right) = \left\{\boldsymbol{l} \in \mathcal{IS}(\boldsymbol{s}) \,\middle|\, \mathcal{S}(\boldsymbol{l}) \cap \mathcal{S}(\boldsymbol{s}) \subset \mathcal{I}_{w,h}^{M,N}\right\} \tag{4.40}$$

and

$$\mathcal{PIS}\left(\boldsymbol{s}_{\big|\mathcal{I}_{w,h}^{M,N}}\right) = \left\{\boldsymbol{l} \in \mathcal{IS}(\boldsymbol{s}) \,\middle|\, \mathcal{S}(\boldsymbol{l}) \cap \mathcal{S}(\boldsymbol{s}) \not\subset \mathcal{I}_{w,h}^{M,N}\right\}. \tag{4.41}$$

The set $\mathcal{FIS}\left(\boldsymbol{s}_{\big|\mathcal{I}_{w,h}^{M,N}}\right)$ is referred to as the *fully intersecting set* of $\boldsymbol{s}$ on $\mathcal{I}_{w,h}^{M,N}$, and the set $\mathcal{PIS}\left(\boldsymbol{s}_{\big|\mathcal{I}_{w,h}^{M,N}}\right)$ as the *partially intersecting set* $\boldsymbol{s}$ on $\mathcal{I}_{w,h}^{M,N}$.

The following lemma characterizes the partially intersecting set of a strip segment. It shows that any line in this set must intersect one of the boundaries of $\mathcal{I}_{w,h}^{M,N}$ at a point that belongs to the interior of $\boldsymbol{s}$.

**Lemma 4.3.** *Let $\mathcal{B} = \{\boldsymbol{v}_l, \boldsymbol{v}_h, \boldsymbol{h}_l, \boldsymbol{h}_h\}$ be the set of boundary lines of $\mathcal{I}_{w,h}^{M,N}$. Then, $\boldsymbol{l} \in \mathcal{PIS}\left(\boldsymbol{s}_{\big|\mathcal{I}_{w,h}^{M,N}}\right)$ if and only if*

$$\exists\, \boldsymbol{l}' \in \mathcal{B} \text{ such that } \boldsymbol{l}' \neq \boldsymbol{l} \text{ and } \mathcal{S}(\boldsymbol{l}|_{\boldsymbol{s}_{int}}) \cap \mathcal{S}(\boldsymbol{l}'|_{\boldsymbol{s}_{int}}) \neq \emptyset, \tag{4.42}$$

*where $\boldsymbol{s}_{int}$ is the interior of $\boldsymbol{s}$.*

*Proof:* Assume that (4.42) holds and denote the point of intersection of $\mathcal{S}(\boldsymbol{l}|_{\boldsymbol{s}_{int}})$ and $\mathcal{S}(\boldsymbol{l}'|_{\boldsymbol{s}_{int}})$ by $\boldsymbol{x}$. Since, by definition, this is an interior point of $\boldsymbol{s}$, for small enough $\epsilon$, there is a ball of radius $\epsilon$ around $\boldsymbol{x}$, $B_\epsilon(\boldsymbol{x})$, such that $B_\epsilon(\boldsymbol{x}) \subset \boldsymbol{s}$. Furthermore, since $\boldsymbol{l}'$ bisects this ball, half of it will be outside of $\mathcal{I}_{w,h}^{M,N}$. Since $\boldsymbol{l}$ also bisects $B_\epsilon(\boldsymbol{x})$ and $\boldsymbol{l} \neq \boldsymbol{l}'$, it follows that $\mathcal{S}(\boldsymbol{l}) \cap \left(\mathcal{I}_{w,h}^{M,N}\right)^c \neq \emptyset$, and $\boldsymbol{l} \in \mathcal{PIS}\left(\boldsymbol{s}_{\big|\mathcal{I}_{w,h}^{M,N}}\right)$.

To prove the converse, assume that $\boldsymbol{s} \in \mathcal{PIS}\left(\boldsymbol{s}_{\big|\mathcal{I}_{w,h}^{M,N}}\right)$. Then, $\mathcal{S}(\boldsymbol{l}) \cap \mathcal{S}(\boldsymbol{s}) \cap \left(\mathcal{I}_{w,h}^{M,N}\right)^c \neq \emptyset$. Since $\boldsymbol{l} \in \mathcal{IS}\left(\boldsymbol{s}_{\big|\mathcal{I}_{w,h}^{M,N}}\right)$, it follows from (4.39) that $\mathcal{S}(\boldsymbol{l}) \cap \mathcal{S}(\boldsymbol{s}) \cap \mathcal{I}_{w,h}^{M,N} \neq \emptyset$. Hence, $\boldsymbol{l}$ must cross one of the boundary lines of $\mathcal{I}_{w,h}^{M,N}$ at an interior point of $\boldsymbol{s}$ and (4.42) follows. ■

The following lemma shows that two parallel lines in $\mathcal{PIS}\left(\boldsymbol{s}_{\left|\mathcal{I}_{w,h}^{M,N}\right.}\right)$ which intersect the same boundary of $\mathcal{I}_{w,h}^{M,N}$ in two interior points of $\boldsymbol{s}$ must have similar $b$ parameters.

**Lemma 4.4.** *Consider the strip $\boldsymbol{s} = (b_l, \theta_l, w)$ associated with line $\boldsymbol{l} = (b_l, \theta_l)$ and two parallel lines $\boldsymbol{l}' = (b', \theta)$ and $\boldsymbol{l}'' = (b'', \theta)$ such that $\boldsymbol{l}', \boldsymbol{l}'' \in \mathcal{PIS}\left(\boldsymbol{s}_{\left|\mathcal{I}_{w,h}^{M,N}\right.}\right)$. If the restrictions of the two lines to the interior of $\boldsymbol{s}$, $\boldsymbol{l}'|\boldsymbol{s}_{int}$ and $\boldsymbol{l}''|\boldsymbol{s}_{int}$, intersect the same boundary line $\boldsymbol{b} \in \mathcal{B}$, where $\mathcal{B}$ is as defined in Lemma 4.3, then*

$$|b' - b''| \leq \delta(w, \theta_l, \theta) \tag{4.43}$$

*where*

$$\delta(w, \theta_l, \theta) = \begin{cases} w \left|\frac{\cos\theta}{\cos\theta_l}\right| & \text{if } \boldsymbol{l} \in \mathcal{R}_{\mathrm{I}} \\ w \left|\frac{\sin\theta}{\sin\theta_l}\right| & \text{if } \boldsymbol{l} \in \mathcal{R}_{\mathrm{II}} \\ w \max\left[\left|\frac{\cos\theta}{\cos\theta_l}\right|, \left|\frac{\sin\theta}{\sin\theta_l}\right|\right] & \text{if } \boldsymbol{l} \in \mathcal{R}_{\mathrm{III}}. \end{cases} \tag{4.44}$$

*Proof:* We start by considering a strip $\boldsymbol{s}$ such that $\mathcal{S}(\boldsymbol{s})$ does not include any of the corners of $\mathcal{I}_{w,h}^{M,N}$. Denote the intersection points of $\boldsymbol{l}'|\boldsymbol{s}_{int}$ and $\boldsymbol{l}''|\boldsymbol{s}_{int}$ with $\boldsymbol{b}$ by $\boldsymbol{x}'$ and $\boldsymbol{x}''$, respectively. From the line equations for $\boldsymbol{l}'$ and $\boldsymbol{l}''$, it follows that $\boldsymbol{x}' \cdot (\cos\theta, \sin\theta) = b'$ and $\boldsymbol{x}'' \cdot (\cos\theta, \sin\theta) = b''$, i.e.

$$|b' - b''| = |(\boldsymbol{x}' - \boldsymbol{x}'') \cdot (\cos\theta, \sin\theta)|. \tag{4.45}$$

We next consider the four possible cases for $\boldsymbol{b}$.

i) $\boldsymbol{b} = \boldsymbol{h}_l$ or $\boldsymbol{b} = \boldsymbol{h}_h$: In these cases, $\boldsymbol{x}' = (\alpha', y)$ and $\boldsymbol{x}'' = (\alpha'', y)$, where $-x_{max} \leq \alpha', \alpha'' \leq x_{max}$, and $y = -y_{max}$ if $\boldsymbol{b} = \boldsymbol{v}_l$ and $y = y_{max}$ if $\boldsymbol{b} = \boldsymbol{v}_h$. Hence, from (4.45),

$$|b' - b''| = |\alpha' - \alpha''|\,|\cos\theta| = ||\boldsymbol{x}' - \boldsymbol{x}''||\,|\cos\theta|.$$

Since both $\boldsymbol{x}'$ and $\boldsymbol{x}''$ belong to the segment $\boldsymbol{b} \cap \boldsymbol{s}$, $||\boldsymbol{x}' - \boldsymbol{x}''|| \leq ||\boldsymbol{x}_0 - \boldsymbol{x}_1||$, where $\boldsymbol{x}_0$ and $\boldsymbol{x}_1$ are the extrema of the segment. These are the points where $\boldsymbol{b}$ intersects the boundary lines of the strip, i.e. the lines $\boldsymbol{l}_0 = \left(b_l - \frac{w}{2}, \theta_l\right)$ and $\boldsymbol{l}_1 = \left(b_l + \frac{w}{2}, \theta_l\right)$. Applying the same arguments to these two points results in

$$w = ||\boldsymbol{x}_1 - \boldsymbol{x}_0||\,|\cos\theta_l|,$$

from which it follows that

$$|b' - b''| \leq w \left|\frac{\cos\theta}{\cos\theta_l}\right|. \tag{4.46}$$

**ii)** $\boldsymbol{b} = \boldsymbol{v}_l$ or $\boldsymbol{b} = \boldsymbol{v}_h$: Using the same arguments as those used in **i)** leads, in these cases, to

$$|b' - b''| \leq w \left| \frac{\sin\theta}{\sin\theta_l} \right|. \tag{4.47}$$

We omit the details for brevity.

The lemma follows from the fact that **i)** always holds for lines in $\mathcal{R}_{\text{I}}$, **ii)** always holds for lines in $\mathcal{R}_{\text{II}}$, and both can hold for lines in $\mathcal{R}_{\text{III}}$. Finally, we consider the case in which $\mathcal{S}(\boldsymbol{s})$ contains one or more corners of $\mathcal{I}_{w,h}^{M,N}$. By selecting the boundary $\boldsymbol{b}$ which is intersected by $\boldsymbol{l}'$ and $\boldsymbol{l}''$ and extending $\mathcal{I}_{w,h}^{M,N}$ along $\boldsymbol{b}$ so that $\boldsymbol{b} \cap \boldsymbol{s}$ is contained in the extended window, the results above are still valid (in the extended window). Since restricting the size of the segment $\boldsymbol{b} \cap \boldsymbol{s}$ can only decrease the distances between the lines that intersect the segment, this implies that the results also hold in $\mathcal{I}_{w,h}^{M,N}$ (even though the bounds may be less tight). ■

The following lemma builds on the previous one to establish that, if $\boldsymbol{s}$ is the strip associated with line $\boldsymbol{l}$, any line $\boldsymbol{l}'$ in $\mathcal{PIS}\left(\boldsymbol{s}_{|\mathcal{I}_{w,h}^{M,N}}\right)$ has a parallel line in $\mathcal{IS}(\boldsymbol{l})$ such that the difference between the $b$ parameters of the two lines is bounded above by a quantity that only depends on the width of $\boldsymbol{s}$ and the angles of $\boldsymbol{l}$ and $\boldsymbol{l}'$.

**Lemma 4.5.** *Consider the strip $\boldsymbol{s}$ associated with the line $\boldsymbol{l} = (b_l, \theta_l)$. For any line $\boldsymbol{l}' = (b', \theta')$ such that $\boldsymbol{l}' \in \mathcal{PIS}\left(\boldsymbol{s}_{|\mathcal{I}_{w,h}^{M,N}}\right)$, there is a parallel line $\boldsymbol{l}'' = (b'', \theta')$ such that $\boldsymbol{l}'' \in \mathcal{IS}\left(\boldsymbol{l}_{|\mathcal{I}_{w,h}^{M,N}}\right)$ and $\boldsymbol{l}'' \in \mathcal{PIS}\left(\boldsymbol{s}_{|\mathcal{I}_{w,h}^{M,N}}\right)$. Furthermore,*

$$b'' - \delta(w, \theta_l, \theta') \leq b' \leq b'' + \delta(w, \theta_l, \theta'), \tag{4.48}$$

*where $\delta(w, \theta_l, \theta')$ is as defined in (4.44).*

*Proof:* We start by considering a strip $\boldsymbol{s}$ such that $\mathcal{S}(\boldsymbol{s})$ does not include any of the corners of $\mathcal{I}_{w,h}^{M,N}$. From Lemma 4.3 and the fact that $\boldsymbol{l}' \in \mathcal{PIS}\left(\boldsymbol{s}_{|\mathcal{I}_{w,h}^{M,N}}\right)$, it follows that $\boldsymbol{l}'$ intersects one of the four boundary lines in $\mathcal{I}_{w,h}^{M,N}$ at a point. Denote the boundary line by $\boldsymbol{b}$ and the intersection point by $\boldsymbol{x}' \in \mathcal{S}(\boldsymbol{b}_{|\boldsymbol{s}_{int}})$. On the other hand, from the fact that $\mathcal{S}(\boldsymbol{l}) \subset \mathcal{S}(\boldsymbol{s})$, it follows that $\boldsymbol{l}$ intersects any of the boundary lines that are intersected by $\boldsymbol{s}$, and in particular $\boldsymbol{b}$. Denote the point of intersection by $\boldsymbol{x} \in \mathcal{S}(\boldsymbol{b}_{|\boldsymbol{s}_{int}})$. Since both $\boldsymbol{x}$ and $\boldsymbol{x}'$ are elements of the restriction of $\boldsymbol{b}$ to $\boldsymbol{s}_{int}$, the simple translation of $\boldsymbol{l}'$ along the segment that originates at $\boldsymbol{x}'$ and terminates at $\boldsymbol{x}$ generates a new line that 1) is parallel to $\boldsymbol{l}'$, and 2) intersects $\boldsymbol{l}$ at the $\boldsymbol{x}$. This is the line $\boldsymbol{l}''$. Since $\boldsymbol{l}'' \in \mathcal{PIS}\left(\boldsymbol{s}_{|\mathcal{I}_{w,h}^{M,N}}\right)$ and both $\boldsymbol{l}'_{|\boldsymbol{s}_{int}}$ and $\boldsymbol{l}''_{|\boldsymbol{s}_{int}}$ intersect $\boldsymbol{b}$ it follows from Lemma 4.4 that $|b' - b''| \leq \delta(w, \theta_l, \theta')$.

When $\mathcal{S}(\boldsymbol{s})$ contains one or more corners of $\mathcal{I}_{w,h}^{M,N}$, by selecting the boundary $\boldsymbol{b}$ which is intersected by $\boldsymbol{l}$ and extending $\mathcal{I}_{w,h}^{M,N}$ along $\boldsymbol{b}$ so that $\boldsymbol{b} \cap \boldsymbol{s}$ is contained in the extended window, the results above are still valid (in the extended window). Since restricting the size of the segment $\boldsymbol{b} \cap \boldsymbol{s}$ can only decrease the distances between the lines that intersect the segment, this implies that the results also hold in $\mathcal{I}_{w,h}^{M,N}$ (even though the bounds may be less tight). ∎

The following theorem combines this lemma with what was previously shown for the intersecting set of a line segment, to characterize the intersecting set of the strip segment associated with $\boldsymbol{s} = (b_l, \theta_l, w)$. It shows that the latter is the union of the intersecting set of the line $\boldsymbol{l} = (b_l, \theta_l)$ with a set that extends its boundaries along the $b$ dimension by a quantity that only depends on the angle $\theta$ and the parameters $w$ and $\theta_l$.

**Theorem 4.3.** *Let $\boldsymbol{s} = (b_l, \theta_l, w)$ be the strip associated with the line $\boldsymbol{l} = (b_l, \theta_l)$. A line $\boldsymbol{l}' = (b, \theta)$ belongs to $\mathcal{IS}\left(\boldsymbol{s}_{\left|\mathcal{I}_{w,h}^{M,N}\right.}\right)$ if and only if*

$$b_{inf}(\theta, b_l, \theta_l) - \delta(w, \theta_l, \theta) \leq b \leq b_{sup}(\theta, b_l, \theta_l) + \delta(w, \theta_l, \theta) \tag{4.49}$$

*where $b_{inf}(\cdot)$ and $b_{sup}(\cdot)$ are the lower- and upper-bounds of $\mathcal{IS}\left(\boldsymbol{l}_{\left|\mathcal{I}_{w,h}^{M,N}\right.}\right)$, as defined in Theorem 4.1, and $\delta(\cdot)$ is as defined in (4.44).*

*Proof:* From Definition 4.10, either $\boldsymbol{l} \in \mathcal{FIS}\left(\boldsymbol{s}_{\left|\mathcal{I}_{w,h}^{M,N}\right.}\right)$ or $\boldsymbol{l} \in \mathcal{PIS}\left(\boldsymbol{s}_{\left|\mathcal{I}_{w,h}^{M,N}\right.}\right)$. If $\boldsymbol{l} \in \mathcal{FIS}\left(\boldsymbol{s}_{\left|\mathcal{I}_{w,h}^{M,N}\right.}\right)$, then $\mathcal{S}(\boldsymbol{l}') \cap \mathcal{S}(\boldsymbol{s}) \subset \mathcal{I}_{w,h}^{M,N}$, which implies that $\boldsymbol{l}'$ intersects the boundary lines of $\boldsymbol{s}$, $\left(b_l \pm \frac{w}{2}, \theta_l\right)$, at two points $\boldsymbol{x}_0, \boldsymbol{x}_1 \in \mathcal{I}_{w,h}^{M,N}$. It follows that $\boldsymbol{l}'$ intersects $\boldsymbol{l}$ at a point that also belongs to $\mathcal{I}_{w,h}^{M,N}$ and, consequently, $\boldsymbol{l}' \in \mathcal{IS}\left(\boldsymbol{s}_{\left|\mathcal{I}_{w,h}\right.}^{M,N}\right)$. From Theorem 4.1, $b_{inf}(\theta, b_l, \theta_l) \leq b \leq b_{sup}(\theta, b_l, \theta_l)$ and (4.49) holds.

On the other hand, if $\boldsymbol{l} \in \mathcal{PIS}\left(\boldsymbol{s}_{\left|\mathcal{I}_{w,h}^{M,N}\right.}\right)$ then, from Lemma 4.4,

$$b \geq b_{inf}(\theta, b_l, \theta_l) - \delta(w, \theta_l, \theta)$$

or

$$b \leq b_{sup}(\theta, b_l, \theta_l) + \delta(w, \theta_l, \theta)$$

and (4.49) follows. ∎

Figure 4.7 presents the boundaries of $\mathcal{IS}\left(\boldsymbol{l}_{\left|\mathcal{I}_{1,1}^{40,40}\right.}\right)$ and $\mathcal{IS}\left(\boldsymbol{s}_{\left|\mathcal{I}_{1,1}^{40,40}\right.}\right)$, where $\boldsymbol{l}$ is the line associated with $\boldsymbol{s}$ and $\boldsymbol{s} = (b_l, \theta_l, 1)$, for the values of $(b_l, \theta_l)$ used in Figure 4.5. Also

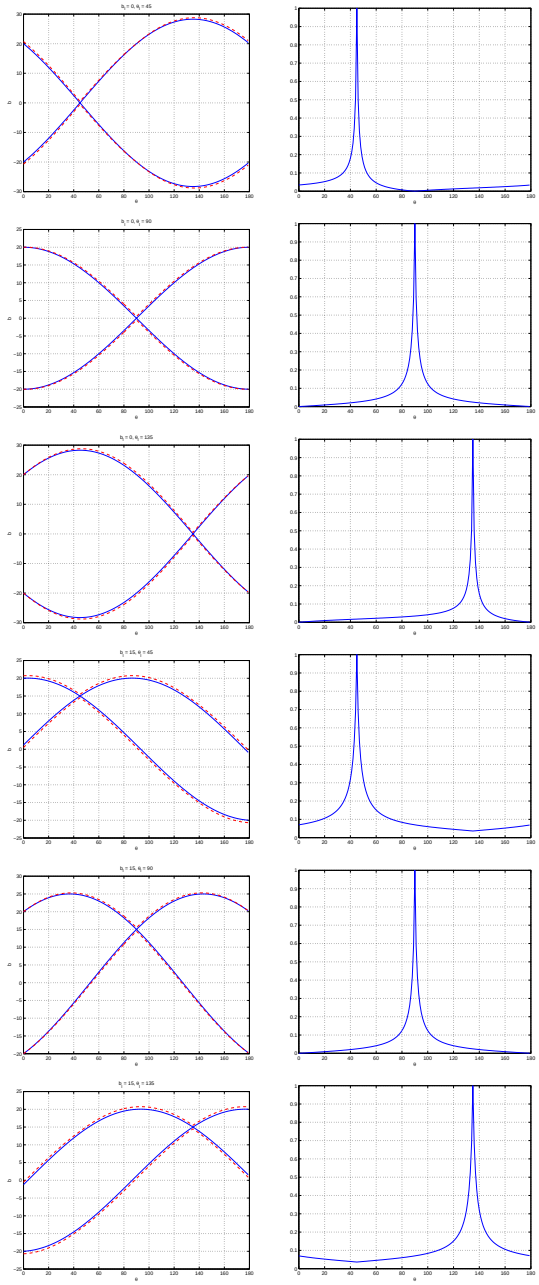

Figure 4.7: Collection of intersecting sets of the strips of unit width associated with the lines presented in Figure 4.5. The intersecting set of each strip segment (associated line) is shown in solid (dashed) on the left of each pair of plots. The plots on the right show the ratio of the width of the band that is not shared by the two intersecting sets to that of the intersecting set of the strip segment, as a function of the angle $\theta$.

shown are the ratios between the width of the band that is not shared by the two intersecting sets, $\mathcal{IS}\left(\boldsymbol{s}\big|_{\mathcal{I}_{1,1}^{40,40}}\right) \cap \mathcal{IS}^c\left(\boldsymbol{l}\big|_{\mathcal{I}_{1,1}^{40,40}}\right)$, and the width of the intersecting set of $\boldsymbol{s}\big|_{\mathcal{I}_{1,1}^{40,40}}$, i.e. $\frac{2\delta(w,\theta_l,\theta)}{b_{sup}(\theta,b_l,\theta_l)-b_{inf}(\theta,b_l,\theta_l)+2\delta(w,\theta_l,\theta)}$. It is clear that the intersecting set of the strip is well approximated by that of the associated line segment, except perhaps when $\theta$ is close to $\theta_l$. This is due to the fact that while for the line the intersecting set collapses to a point when $\theta \to \theta_l$ (two parallel lines do not intersect unless they are the same), the same does not hold for the strip (all lines parallel to $\boldsymbol{l}$ at a distance less than $\frac{w}{2}$ belong to $\mathcal{IS}\left(\boldsymbol{s}\big|_{\mathcal{I}_{w,h}^{M,N}}\right)$).

**Remark 4.2.** It should be emphasized that the intersecting set of a strip segment is not always well approximated by that of a line segment. There are in fact lines for which the width of the former can be significantly larger than that of the latter. Consider, for example, a line $\boldsymbol{l}$ with $\theta_l = \frac{\pi}{2} + \epsilon$ and $b_l$ such that the line intersects the boundary $\boldsymbol{v}_h$ at the point $\boldsymbol{x} = \left(x_{max}, y_{max} + \frac{w}{2}\right)$. By varying $b_l$ and $\epsilon$, it is possible to make $\boldsymbol{l}$ intersect the boundary $\boldsymbol{h}_h$ at any point $\boldsymbol{x} = (\alpha, y_{max}), -x_{max} \leq \alpha < x_{max}$, while keeping the segment that originates at $\boldsymbol{x}$ and terminates at the corner $(x_{max}, y_{max})$ in the interior of $\boldsymbol{s}$. Hence, any line with $\theta = 0$ and $x_{max} - \alpha < b < x_{max}$ will belong to $\mathcal{PIS}\left(\boldsymbol{s}\big|_{\mathcal{I}_{w,h}^{M,N}}\right)$ but not to $\mathcal{IS}\left(\boldsymbol{l}\big|_{\mathcal{I}_{w,h}^{M,N}}\right)$. Thus, by varying the line parameters, it is possible to make the width of $\mathcal{PIS}\left(\boldsymbol{s}\big|_{\mathcal{I}_{w,h}^{M,N}}\right)$ quite large and the width of $\mathcal{IS}\left(\boldsymbol{l}\big|_{\mathcal{I}_{w,h}^{M,N}}\right)$ quite small. In the extreme, the line $\boldsymbol{l}$ can touch only one point of $\mathcal{I}_{w,h}^{M,N}$ while the strip $\boldsymbol{s}$ entirely covers one of its boundaries. Notice, however, that such situations are only possible when $\theta_l$ is very close to either 0 or $\frac{\pi}{2}$ and $b_l$ is near the lower- or upper-bounds for the set of lines supported by $\mathcal{I}_{w,h}^{M,N}$. This is impossible if $\boldsymbol{l} \in \mathcal{R}_{\mathrm{I}} \cup \mathcal{R}_{\mathrm{II}}$, but can happen in $\mathcal{R}_{\mathrm{III}}$. The bounds of (4.49) account for this phenomena since, in $\mathcal{R}_{\mathrm{III}}$, $\delta(w, \theta_l, \theta)$ goes to infinity as $\theta_l$ approaches 0 or $\frac{\pi}{2}$. In these cases, the bounds are obviously not tight.

# Chapter 5

# Deterministic models for the Radon transform of pixelated lines

From the standpoint of engineering applications, the goodness of a model is intrinsically connected to the particular application for which it is considered. Thus, while there is usually no best model in the absolute sense, it is important to understand the advantages or limitations of each model in the context of the desired application and how the model's predictions are affected by different settings for its parameters. The ultimate goal is usually to find the best trade-off between the complexity of the model and its capability to make predictions at a desired level of accuracy.

In the previous chapters, we have discussed various models that can be used to represent a pixelated line (namely the line, line segment, and strip) leading to a collection of approximations to the Radon transform of the pixelated line that trade-off accuracy for computational complexity. In this chapter, we start considering the application of such models to the problem of line detection. We begin by introducing a taxonomy of the models previously discussed and making explicit the assumptions under which they are based. It is then shown that the standard strategy of line detection (thresholding of Radon amplitudes) is well justified under the assumption of the idealized line, but fundamentally flawed for models that more closely replicate the Radon transform of the pixelated line. In particular, we show that the thresholding strategy is intrinsically unable to simultaneously achieve a low false-positive rate and spatial localization of the detected lines.

This motivates a new line detection strategy, derived from the more realistic approximation of the pixelated line by a strip segment. The Radon transform of the latter is proposed as a parametric model for that of the pixelated line, and shown to provide an accurate ap-

proximation at very low computational cost. This is a result of practical significance since it enables the adoption of an analysis-by-synthesis strategy for line detection. Such a strategy would be computationally unfeasible using the exact Radon transform of the pixelated line, and highly ineffective under the less realist models of the idealized line, segment, or even unbounded strip. An analysis-by-synthesis algorithm is designed and shown to achieve significantly better line detection accuracy than any of the thresholding methods.

## 5.1 A taxonomy for the Radon transform of a pixelated line

Table 5.1 presents a summary of the models considered in the previous chapters. These models can be seen as a sequence of approximations to the pixelated line, where one trades off the accuracy of the approximation for the number of parameters in the model (and inherent complexity of the Radon transform). The table also points out how each model deals with the three properties of the pixelated line that have the most relevance for line detection applications: *support* (pixelated lines are defined on images, which are regions of bounded support), *width* (pixelated lines have non-zero width), and *pixelization* (pixelated lines are pixelated functions, i.e. functions supported on sets of pixels). As can be seen from the table, only the *pixelated line* model of (2.31) accounts for the three attributes correctly.

| model | Radon transform | support | width | pixelization |
|---|---|---|---|---|
| *line* | (2.14) | unbounded | null | no |
| *segment* | (2.17) | bounded | null | no |
| *strip* | (2.22) | unbounded | positive | no |
| *strip segment* | - | bounded | positive | no |
| *pixelated line* | (2.31) | bounded | positive | yes |

Table 5.1: Models that can be used to represent a pixelated line. The Radon transform of the strip segment is discussed in this chapter. See Lemma 5.3 and ensuing discussion.

In the context of image-based applications such as line detection, it is important to understand how the assumptions behind each model may affect the model's performance.

### 5.1.1 The line model

We start by the line which, assuming unbounded support, null width, and no pixelization, appears to be a reasonable approximation when the image size is many orders of magnitude

larger than the pixel size. The main appeal of the line model is the simplicity of its Radon transform which consists of a delta function centered on the line parameters. This suggests a very simple and popular line detection algorithm.

**Algorithm 5.1.** *Given the Radon transform of the pixelated edge map of an edge indicator function $\mathcal{E}$,*

$$r_{i,j} = \mathcal{R}\{\mathcal{E}\mathcal{M}[\mathcal{E}](\boldsymbol{x})\}(b_i, \theta_j),$$

*declare an edge with parameters $(b_i, \theta_j)$ if*

$$r_{i,j} \geq T, \tag{5.1}$$

*where $T$ is an appropriate threshold.*

There are various ways to select the best value for the threshold $T$, the simplest of which is brute-force, i.e. try various values and select the one that leads to best results. The problem, however, is that there are many situations where it is impossible to find a threshold that leads to perfect detection. This is due to the fact that the Radon transform of the line is not a reasonable approximation to that of the pixelated line, even when the image size is large relatively to the pixel size. An example is given in Figure 5.1 which presents an image of size $512 \times 512$ pixels containing three lines $\boldsymbol{l}_1 = \left(-3, \frac{3\pi}{4}\right)$, $\boldsymbol{l}_2 = \left(3, \frac{3\pi}{4}\right)$, and $\boldsymbol{l}_3 = \left(300, \frac{3\pi}{4}\right)$, the contours of its Radon transform, those of the Radon transform predicted by the line model (three delta functions represented as circles) and the lines recovered by the algorithm above with a threshold equal to 15, 20, or 60% of the maximum amplitude of the Radon transform. Notice that the Radon transform of the image is quite different from that predicted by the model. In particular it is difficult to distinguish the individual contributions of $\boldsymbol{l}_1$ and $\boldsymbol{l}_2$. This, and the different lengths of the segments $\boldsymbol{g}_i = \left(\boldsymbol{l}_i, \mathcal{I}_{w,h}^{M,N}\right), i = 1, \ldots, 3$, make it impossible to find one threshold that will detect all lines without generating false positives. At 15%, all lines are recovered, but multiple spurious lines with parameters similar to those $\boldsymbol{l}_1$ and $\boldsymbol{l}_2$ are detected. At 20%, even though many of the spurious lines continue to be detected, $\boldsymbol{l}_3$ is missed. At 60%, the spurious lines are no longer detected but the same holds for $\boldsymbol{l}_3$. Notice that, for lower values of the threshold, it is quite difficult to tell if the original lines were parallel or not, or even if they crossed each other. Depending on the application, this can be quite problematic.

### 5.1.2 The segment model

The fact that the line model fails to account for the different lengths of the segments generated by restricting each line to $\mathcal{I}_{w,h}^{M,N}$ is a major limitation for line detection. This

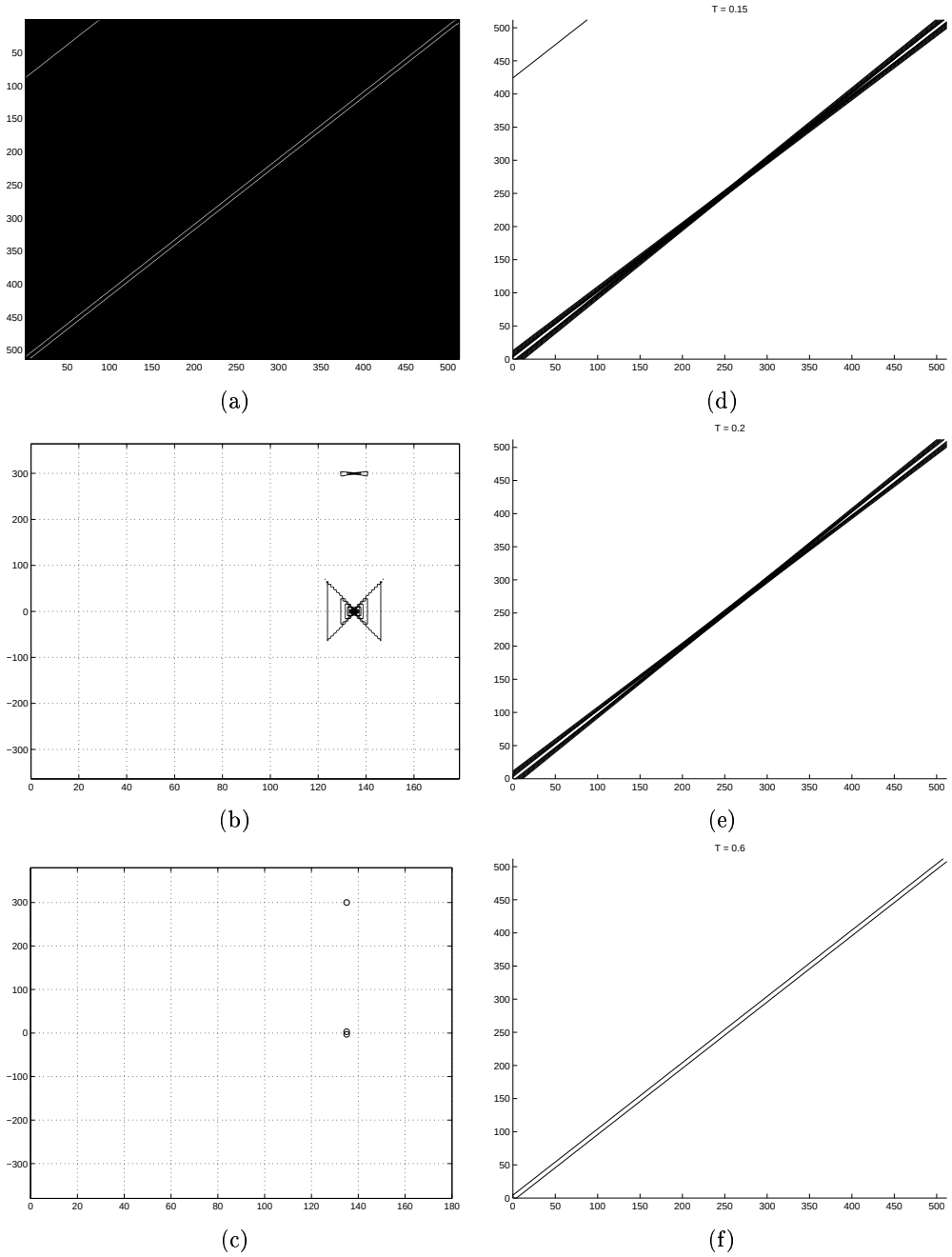


Figure 5.1: Left: (a) an edge map with three lines, (b) its Radon transform, and (c) Radon transform predicted by the line model. Right: recovered lines with thresholds of (d) 15, (e) 20, and (f) 60% of the maximum amplitude.

limitation is abbreviated by the subsequent model in Table 5.1: the segment. As can be seen by comparing (2.14) and (2.17), the only difference between the Radon transform of a line and that of one of its segments is the replacement of the Dirac delta function by the Kronecker delta function, scaled by the segment length. This suggests that a better thresholding method would be one where the threshold is adapted to the length of each segment. The following theorem derives a closed form expression for this length.

**Theorem 5.1.** *Consider a line* $\boldsymbol{l} = (b_l, \theta_l)$ *and the segment* $\boldsymbol{g} = \left(b_l, \theta_l, \mathcal{I}_{w,h}^{M,N}\right)$. *The length of* $\boldsymbol{g}$ *is*

$$\mathfrak{L}(\boldsymbol{g}) = \begin{cases} 2\frac{x_{max}}{|\sin\theta_l|} & \text{if } \boldsymbol{l} \in \mathcal{R}_{\mathsf{I}} \\ 2\frac{y_{max}}{|\cos\theta_l|} & \text{if } \boldsymbol{l} \in \mathcal{R}_{\mathsf{II}} \\ \frac{x_{max}}{|\sin\theta_l|} + \frac{y_{max}}{|\cos\theta_l|} - \frac{2|b_l|}{|\sin(2\theta_l)|} & \text{if } \boldsymbol{l} \in \mathcal{R}_{\mathsf{III}}. \end{cases} \tag{5.2}$$

*where the regions* $\mathcal{R}_{\mathsf{I}}, \mathcal{R}_{\mathsf{II}}$, *and* $\mathcal{R}_{\mathsf{III}}$ *are as defined in Lemma 4.2.*

*Proof:* From the definition of length of $\boldsymbol{g}$ in (2.18),

$$\begin{aligned} \mathfrak{L}(\boldsymbol{g}) &= \int_{\mathcal{I}_{w,h}^{M,N} \cap \mathcal{S}(\boldsymbol{g})} d\boldsymbol{x} \\ &= \int \mathbf{1}_{\left\{\mathcal{I}_{w,h}^{M,N} \cap \mathcal{S}(\boldsymbol{g})\right\}}(\boldsymbol{x})\, d\boldsymbol{x} \\ &= \int \mathbf{1}_{\left\{\mathcal{I}_{w,h}^{M,N}\right\}}(\boldsymbol{x})\, \delta(b_l - \boldsymbol{\xi}_l \cdot \boldsymbol{x})\, d\boldsymbol{x}. \end{aligned}$$

From (2.23) and (4.2),

$$\mathcal{I}_{w,h}^{M,N} = \mathcal{S}(\boldsymbol{p})$$

where $\boldsymbol{p}$ is the pixel $\boldsymbol{p} = (0, 0, 2x_{\max}, 2y_{\max})$ and, using (2.24), the integral above is simply the Radon transform of $\mathcal{P}[\boldsymbol{p}](\boldsymbol{x})$. The theorem follows from Lemma 2.6. ∎

Figure 5.2 presents a contour plot for the length of all segments supported by $\mathcal{I}_{1,1}^{512,512}$ (as a function of $b_l$ and $\theta_l$) as computed by (5.2). Notice the similarities between the surface represented in this plot and that of the Radon transform of the pixel centered at the origin, shown in Figure 2.2. The shape of this surface suggests that Algorithm 5.1 can be improved by adapting the threshold to the length of each segment.

**Algorithm 5.2.** *Given the Radon transform of the pixelated edge map of an edge indicator function* $\mathcal{E}$,

$$r_{i,j} = \mathcal{R}\{\mathcal{EM}[\mathcal{E}](\boldsymbol{x})\}(b_i, \theta_j),$$

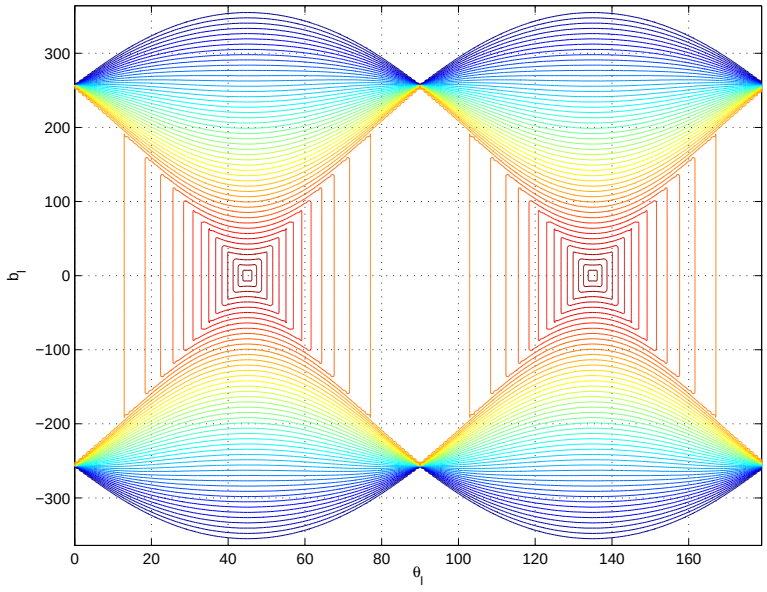


Figure 5.2: Contour plot of the length of the segments $\left(b_l, \theta_l, \mathcal{I}_{1,1}^{512,512}\right)$ as a function of the parameters $b_l$ and $\theta_l$.

*declare an edge with parameters* $(b_i, \theta_j)$ *if*

$$r_{i,j} \geq T \frac{r^* \mathfrak{L}(\boldsymbol{g}_{i,j})}{l^*}. \tag{5.3}$$

*where* $T \in [0,1]$ *is a scaling factor,* $r^* = \max_{k,l} r_{k,l}$, $l^* = \max_{k,l} \mathfrak{L}(\boldsymbol{g}_{k,l})$, *and* $\boldsymbol{g}_{i,j} = \left(b_i, \theta_j, \mathcal{I}_{w,h}^{M,N}\right)$.

Notice that the ratio $\frac{\mathfrak{L}(\boldsymbol{g}_{i,j})}{l^*}$ adapts the threshold to the length of segment $\boldsymbol{g}_{i,j}$. Figure 5.3 presents the results obtained with this algorithm for the edge map of Figure 5.1. It is clear that, while care must be taken in the selection of an appropriate value for $T$, the introduction of the adaptive threshold makes it possible to detect the three lines without any false positives.

While this is encouraging, the next example shows that the segment model is not sufficient to handle all the problems posed by line detection. In this example, the edge map of Figure 5.1(a) is augmented with the segment $\boldsymbol{g}\left(0, \frac{\pi}{4}, \mathcal{I}_{1,1}^{140,140}\right)$, as shown in Figure 5.4(a). The figure also presents the Radon transform of the new edge map, and the lines recovered by Algorithm 5.2 for two values of $T$. It illustrates two shortcomings of Algorithm 5.2. First, while for both values of $T$ various spurious lines are detected in the neighborhood of $\boldsymbol{l}_1$, $\boldsymbol{l}_2$, and $\boldsymbol{l}_3$, for $T = 0.3$ it is already impossible to detect the extra segment $\boldsymbol{g}$. This is due

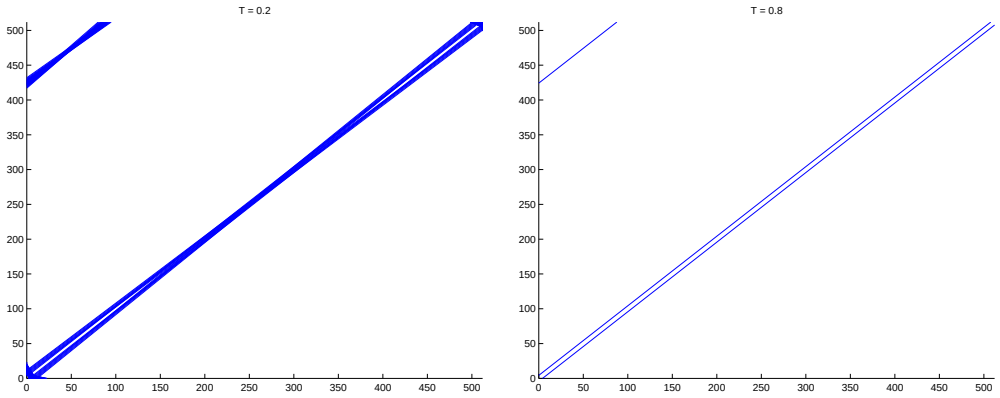


Figure 5.3: Lines recovered by applying Algorithm 5.3 to the edge map of Figure 5.1 with $T$ set to (a) 0.15, and (b) 0.8.

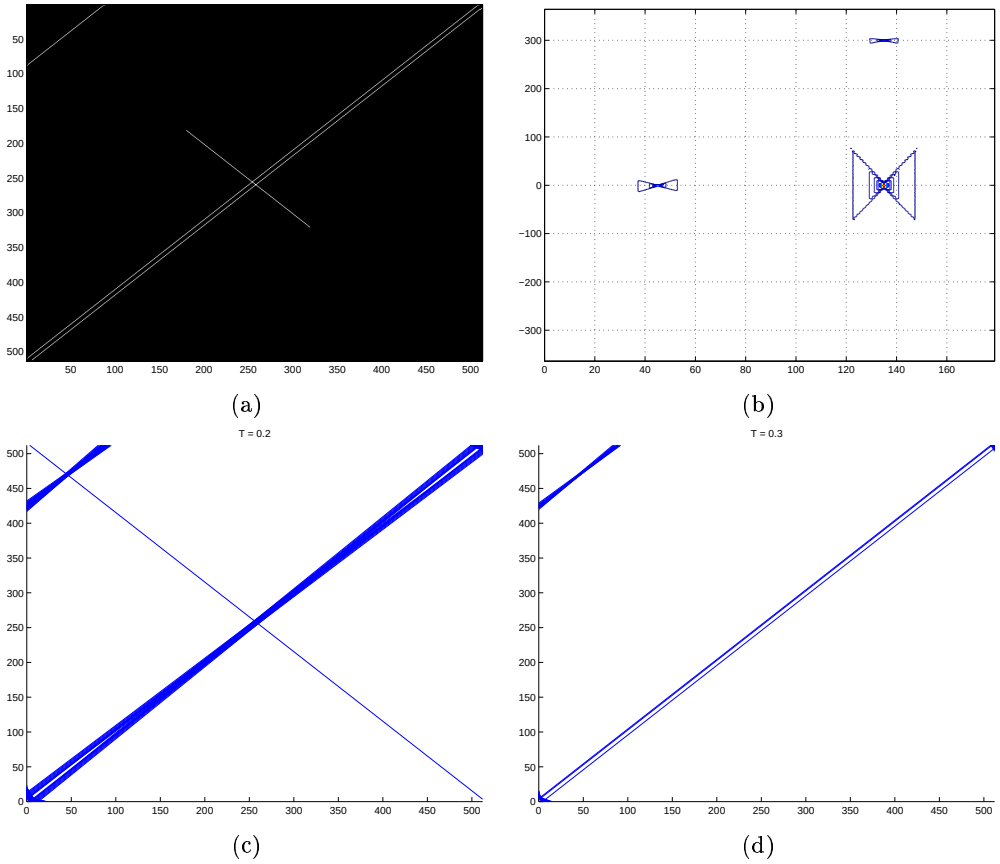


Figure 5.4: Top: (a) Edge map with four segments and (b) its Radon transform. Bottom: Lines recovered by Algorithm 5.3 with $T$ set to (c) 0.2 and (d) 0.3.

to the fact that the length of the latter is not well predicted by (5.2), which assumes that segments span the entire image $\mathcal{I}_{w,h}^{M,N}$. It is not clear how the thresholding approach could be extended to avoid this problem, since such extension would require the knowledge of the endpoints of the segment and these are part of what needs to be determined. Second, even for the values of $T$ in which $\boldsymbol{g}$ is detected, it is impossible to recover the segment accurately from the amplitude of the peaks of the Radon transform. While these carry information about the segment's length, they provide no information about its start- or end-points. In fact, due to the additive property of the Radon transform, and the fact that the Radon transform of a pixelated line has a region of support which is non-negligible, each peak will receive contributions from various lines. Hence, for non-trivial edge maps, the amplitude of a peak can only be taken as a very rough estimate of the length of the associated segments.

The two problems, inability to detect segments that do not span the entire image and localization of endpoints, can be better addressed by localizing the computation of the Radon transform.

**Algorithm 5.3.** *Given the pixelated edge map of an edge indicator function $\mathcal{E}$,*

- *define a sequence of subimages*

$$\left(\mathcal{W}_{w,h}^{L,C}\right)_{i,j} = \mathcal{E}(\boldsymbol{x}) \times \mathbf{1}_{\{x_i \le x \le x_{i+1}, y_j \le y \le y_{j+1}\}}(\boldsymbol{x}), \tag{5.4}$$

  *where*

$$\begin{aligned} x_i &= -x_{\max} + iC,\ i \in 0, \ldots, \left\lfloor \frac{2x_{max}}{C} \right\rfloor - 1 \\ y_j &= -y_{\max} + jL,\ j \in 0, \ldots, \left\lfloor \frac{2y_{max}}{L} \right\rfloor - 1; \end{aligned}$$

- *apply Algorithm 5.2 to each of the subimages $\left(\mathcal{W}_{w,h}^{L,C}\right)_{i,j}$ to obtain a sequence of edge segments $\mathcal{G}_{i,j} = \left(\boldsymbol{g}_1, \ldots, \boldsymbol{g}_{S_{i,j}}\right)_{i,j}$, where $S_{i,j}$ is the number of segments in subimage $(i,j)$;*

- *combine the segments extracted from the subimages into a set of image edges.*

This algorithm requires requires procedures for 1) determining the best value of the window size $(L, C)$, and 2) combining local segments into global edges. We assume that such procedures are available and concentrate on the advantages of localizing the Radon transform for the purposes of recovering image segments.

Figure 5.5 presents the subimage of the edge map of Figure 5.4 which contains the segment $\boldsymbol{g}$ (a) and its Radon transform (b). Comparing the latter with that of Figure 5.4(b), it is possible to notice two major differences. First, it is now much more clear that there are two different lines contributing to the overall shape of the Radon transform in the neighborhood of $\boldsymbol{l} = \left(0, \frac{3\pi}{4}\right)$. Second, these two contributions are similar, in terms of shape and amplitude, to that of the segment $\boldsymbol{g}$. This means that, when the Radon transform is localized, it becomes easier 1) to make fine distinctions between lines with similar parameterizations, and 2) to detect segments whose length is much smaller than the image size. This, however, does not mean that line detection is trivial once the Radon transform

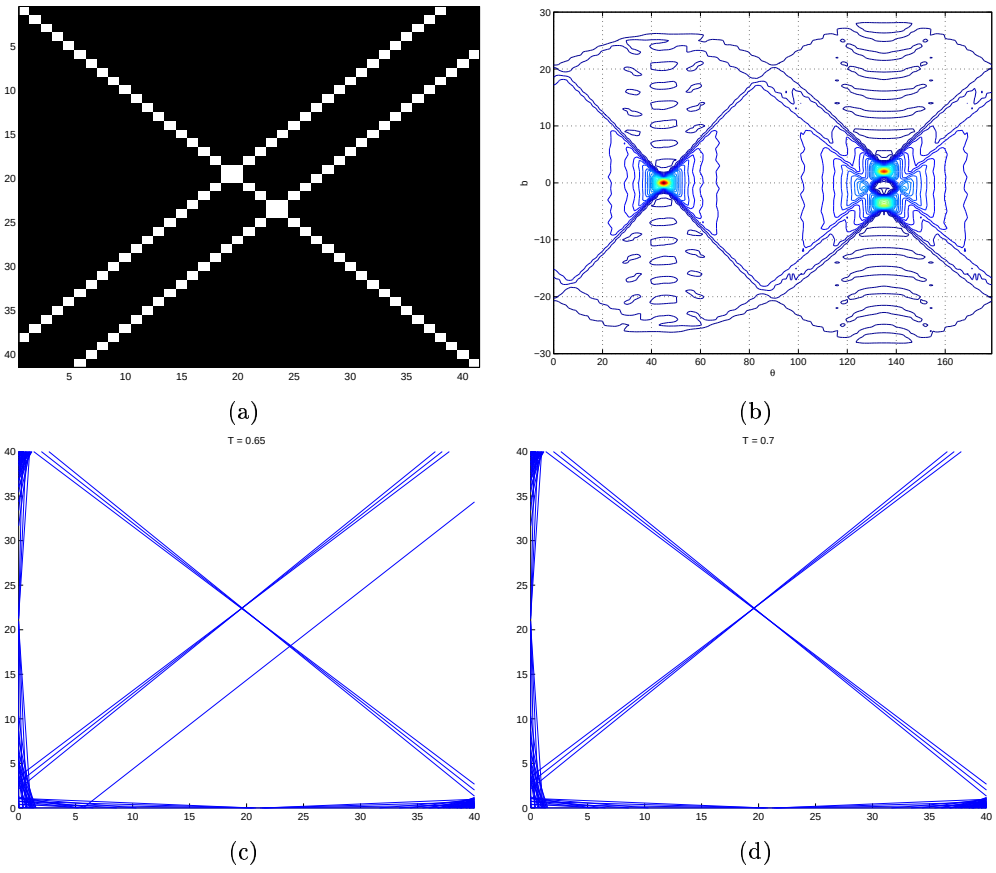


Figure 5.5: Top: (a) Subimage of the edge map of Figure 5.4 and (b) its Radon transform. Bottom: Lines recovered by Algorithm 5.2 with $T$ set to (c) 0.65 and (d) 0.7.

is localized. In fact, the localization exacerbates the limitations of the segment model, as illustrated in plots (c) and (d) of the figure. These plots are the result of applying Algo-

rithm 5.2 to the edge map (of the window) shown in 5.5(a) for two values of $T$. While, in both cases, various spurious lines are detected in the neighborhood of $\boldsymbol{g}$ and $\boldsymbol{l}_2$, for $T = 0.7$ it is already impossible to $\boldsymbol{l}_1$. Note that the performance of the segment model is significantly worse than in Figure 5.3(b) where it was possible to detect segments spanning the entire image ($\boldsymbol{l}_1$, $\boldsymbol{l}_2$, and $\boldsymbol{l}_3$) without false positives. For the edge map of Figure 5.5, the segment model is clearly unable to do so. The problem is that, because the segments are now significantly smaller, the same holds for the peak amplitudes of the Radon transform. Hence, what happens in the neighborhoods of these peaks becomes significantly more relevant. This can be seen by comparing the Radon transforms of Figures 5.4 and 5.5, and noticing that the relatively narrow bowtie patterns of the former have been replaced by a set of sinusoidal patterns of significantly larger support and magnitude in the latter. To address this problem, we need to consider the remaining models in Table 5.1.

### 5.1.3 The strip model

The novelty introduced by the strip model, over its line and segment counterparts, is to account for the fact that pixelated lines have non-zero width. While the width of a pixelated line is usually quite small when compared to quantities such as the image or window size, it turns out that it plays a major role in the number of false positives generated by methods that threshold the amplitude of the Radon transform.

**Lemma 5.1.** *Let $r_s(b,\theta)$ denote the Radon transform of the indicator function of a strip $\boldsymbol{s} = (b_s, \theta_s, w_s)$, as given by (2.22), and let*

$$\bar{r}_s(b,\theta,r_{max}) = \min\left[r_s(b,\theta), r_{max}\right]. \tag{5.5}$$

*Assume that $\bar{r}_s(b,\theta,r_{max})$ is known for all $(b,\theta)$. If $\bar{r}_s(b,\theta,r_{max}) = a$, then*

$$\theta_s = \begin{cases} \theta & \text{if } a = 0 \\ \theta \pm \arcsin\left(\frac{w_s}{a}\right) & \text{if } 0 < a < r_{max} \end{cases} \tag{5.6}$$

*and, if $a = r_{max}$, either*

$$\theta_s \in \left[\theta, \theta + \arcsin\left(\frac{w_s}{a}\right)\right] \tag{5.7}$$

*or*

$$\theta_s \in \left[\theta - \arcsin\left(\frac{w_s}{a}\right), \theta\right]. \tag{5.8}$$

*Furthermore, for all $a$, it is possible to determine if the '$\pm$' in (5.6) is a '$+$' or a '$-$' and which of (5.7) or (5.8) holds.*

*Proof:* The lemma is a simple consequence of (2.22). If $0 \leq a < r_{max}$, it follows, from (5.5), that $r_s(b,\theta) = a$ and, from (2.22), we have

$$\theta_s = \begin{cases} \theta & \text{if } a = 0 \\ \theta \pm \arcsin\left(\frac{w_s}{a}\right) & \text{otherwise.} \end{cases} \tag{5.9}$$

Still from (2.22), if $r_s(b,\theta) = a$ and $a > 0$, there exists $\theta'$, $\theta' = 2\theta_s - \theta$, such that $r_s(b,\theta') = a$. Hence, from the observation of $\bar{r}_s(b,\theta',r_{max})$, it is possible to determine $\theta_s$ unambiguously (set $\theta_s = \theta + \arcsin\left(\frac{w_s}{a}\right)$, if $\theta < \theta'$ and $\theta_s = \theta - \arcsin\left(\frac{w_s}{a}\right)$, otherwise). When $a = r_{max}$, it follows from (5.5) that $r_s(b,\theta) \geq r_{max}$ and from (2.22) that

$$|\theta_s - \theta| \leq \arcsin\left(\frac{w_s}{r_{max}}\right).$$

Repeating the argument above, there exists $\theta' = 2\theta_s - \theta$ such that

$$|\theta_s - \theta'| \leq \arcsin\left(\frac{w_s}{r_{max}}\right)$$

and it is possible to say which of (5.7) and (5.8) holds. ∎

This lemma provides the insight needed to understand the trade-offs between the limit $r_{max}$ and the accuracy with which line parameters can be recovered.

**Theorem 5.2.** *Let $r_s(b,\theta)$ denote the Radon transform of the indicator function of a strip $\boldsymbol{s} = (b_s, \theta_s, w_s)$, as given by (2.22), and let*

$$\bar{r}_s(b,\theta,r_{max}) = \min\left[r_s(b,\theta), r_{max}\right]. \tag{5.10}$$

*Then, from the observation of $\bar{r}_s(b,\theta,r_{max})$, it is possible to recover the angle $\theta_s$ unequivocally if and only if $\bar{r}_s(b,\theta,r_{max}) < r_{max}$. For $\bar{r}_s(b,\theta,r_{max}) = r_{max}$, it is impossible to recover $\theta_s$ with an error inferior to*

$$\epsilon_s(r_{max}) = \arcsin\left(\frac{w_s}{r_{max}}\right). \tag{5.11}$$

*Furthermore, if $\boldsymbol{S} = \{\boldsymbol{s}_1, \ldots, \boldsymbol{s}_n\}$ is a sequence of distinct strips ($\boldsymbol{s}_i \neq \boldsymbol{s}_j, \forall i \neq j$) such that*

$$\bar{r}_{s_i}(b_j,\theta_j,r_i) \leq \delta,\ \forall i, j \neq i, \delta > 0, \tag{5.12}$$

*$R(b,\theta)$ is defined as*

$$R(b,\theta) = \sum_{i=1}^{n} \bar{r}_{s_i}(b,\theta,r_i), \tag{5.13}$$

*$\{r_1, \ldots, r_n\}$ is an arbitrary sequence ordered in a way such that*

$$j < i \Leftrightarrow R(b_j, \theta_j) > R(b_i, \theta_i) \tag{5.14}$$

*and*

$$\mathcal{B}[\boldsymbol{S}](b, \theta, r^*) = \mathbf{1}_{\{R(b,\theta) \geq r^*\}}(b, \theta), \tag{5.15}$$

*then*

$$\mathcal{B}[\boldsymbol{S}](b_i, \theta_i, r^*) = 1 \Rightarrow \mathcal{B}[\boldsymbol{S}](b_j, \theta, r^*) = 1, \; \forall j \leq i, |\theta - \theta_j| \leq \epsilon_j, \tag{5.16}$$

*where*

$$\epsilon_j \leq \arcsin\left(\frac{w_{s_j}}{r^* - (n-1)\delta}\right). \tag{5.17}$$

*Proof:* The first part of the theorem is a straightforward consequence of Lemma 5.1. To prove (5.16), we start by assuming that $\mathcal{B}[\boldsymbol{S}](b_i, \theta_i, r^*) = 1$. Then, from (5.15), $R(b_i, \theta_i) \geq r^*$ and , from (5.14), $R(b_j, \theta_j) \geq r^*, \forall j < i$. It follows that $\mathcal{B}[\boldsymbol{S}](b_j, \theta_j, r^*) = 1, \forall j < i$. Furthermore, from

$$\mathbf{1}_{\{R(b,\theta) \geq r^*\}}(b, \theta) = \mathbf{1}_{\left\{r^* - \sum_{i \neq j} \bar{r}_{s_i}(b,\theta,r_i) \leq \bar{r}_{s_j}(b,\theta,r_j)\right\}}(b, \theta),$$

it follows that $\mathcal{B}[\boldsymbol{S}](b_j, \theta, r^*) = 1$ for all pairs $(b_j, \theta)$ such that

$$\bar{r}_{s_j}(b_j, \theta, r_j) \geq r^* - \sum_{i \neq j} \bar{r}_{s_i}(b_j, \theta, r_i)$$

or, from (5.10) and (5.12),

$$r_s(b_j, \theta) \geq r^* - \sum_{i \neq j} \bar{r}_{s_i}(b_j, \theta, r_i) \geq r^* - (n-1)\,\delta.$$

Since these are the pairs where

$$\bar{r}_s(b_j, \theta, r^* - (n-1)\,\delta) = r^* - (n-1)\,\delta,$$

(5.16) follows from the first part of the theorem. ∎

It is useful to analyze the conditions under which the theorem holds. We start by considering the various quantities involved. From (5.10), $\bar{r}_s(b, \theta, r_{max})$ is the result of limiting the Radon transform of the strip $\boldsymbol{s}$ to the value $r_{max}$. While we have so far introduced no motivation for such a limitation, we will see in Lemma 5.5 that it is one of the consequences of working with the Radon transform of the restriction of the indicator function of $\boldsymbol{s}$ to a

bounded image. From (5.13), $R(b,\theta)$ is the Radon transform of a collection of such indicator functions, i.e. the Radon transform of the pixelated edge map containing the lines $\{(b_1,\theta_1),\ldots,(b_n,\theta_n)\}$, under the strip model. Finally, $\mathcal{B}[\boldsymbol{S}](b_i,\theta_i,r^*)$ is the result of thresholding $R(b,\theta)$ at the level $r^*$. We next look at the conditions themselves. Condition (5.14) is really not required for (5.16) and (5.17) to hold, but simplifies the expression of (5.16). It simply reorders the $r_i$ so that the peaks of $R(b,\theta)$ are ordered by decreasing magnitude and therefore implies no loss of generality. Condition (5.12) is also not necessary, but simplifies the expression of $\epsilon_j$ which would otherwise be

$$\epsilon_j \leq \arcsin\left(\frac{w_{s_j}}{r^* - \sum_{i\neq j}\bar{r}_{s_i}(b,\theta,r_i)}\right). \tag{5.18}$$

It holds with small values of $\delta$ when $\frac{1}{|\sin(\theta_i-\theta_j)|} << \min[R(b_i,\theta_i),R(b_j,\theta_j)]$, $\forall i,j\neq i$. Given the fast decay of the function $\frac{1}{|\sin(x)|}$, this is a reasonable assumption in most practical situations.

Theorem 5.2 exposes a fundamental limitation of thresholding algorithms for line detection. On one hand, the parameters of the strip associated with each peak of the Radon transform of a pixelated edge map can only be recovered uniquely by a threshold smaller than the amplitude of the peak. On the other, thresholding a peak at a given amplitude will originate many false positives for all peaks of larger magnitude, namely all lines with the correct $b$ but $\theta$ in the range determined by (5.16) and (5.17). Hence, the $i^{th}$ strip $\boldsymbol{s}_i$ can be detected if and only if, for $j<i$, the angle of the $j^{th}$ strip is determined with an error of at least $\epsilon_j$. The following corollary establishes a connection between this error and the image size.

**Corollary 5.1.** *Consider the collection of strips $\boldsymbol{S}$ of Theorem 5.2, where all strips have the same width $w_s$ and assume that*

$$r_n \leq D \tag{5.19}$$

*where $D$ is a constant. Then, if $r^*$ is such that all lines are detected, it is impossible to recover $\theta_j$ with an error smaller than*

$$\epsilon^* = \arcsin\left(\frac{w}{D}\right), \tag{5.20}$$

*for any $j<n$.*

*Proof:* From (5.16), given that the $n^{th}$ line is detected,

$$\mathcal{B}[\boldsymbol{S}](b_j,\theta,r^*) = 1,\ \forall j\leq n,\ |\theta-\theta_j| \leq \arcsin\left(\frac{w}{r^*-(n-1)\delta}\right). \tag{5.21}$$

On the other hand, combining (5.10), (5.12), (5.13), and (5.19),

$$\begin{aligned} R(b_n,\theta_n) - (n-1)\delta &\leq R(b_n,\theta_n) - \sum_{i<n} \bar{r}_{s_i}(b_n,\theta_n,dr_i) && (5.22)\\ &= \bar{r}(b_n,\theta_n,r_n) && (5.23)\\ &\leq r_n \leq D. && (5.24) \end{aligned}$$

Since, from (5.15), the $n^{th}$ line is detected if and only if $r^* \leq R(b_n,\theta_n)$, it follows that $D \geq r^* - (n-1)\delta$ and consequently

$$\arcsin\left(\frac{w}{D}\right) \leq \arcsin\left(\frac{w}{r^* - (n-1)\delta}\right).$$

Hence, for $j < n$, any line $(b_j,\theta)$ such that

$$|\theta - \theta_j| \leq \arcsin\left(\frac{w}{D}\right)$$

will satisfy (5.21) and will therefore also be detected. ∎

This corollary is interesting in light of results of the following sections, where we will see (Lemma 5.5) that when one considers the restriction of the strips in $\boldsymbol{S}$ to the image $\mathcal{I}_{w,h}^{M,N}$, (5.19) holds with $D$ as defined in (4.13). This means that the uncertainty with which the angles of the lines associated with the strips in $\boldsymbol{S}$ can be recovered is intrinsically dependent on the image size. Figure 5.6 shows how $\epsilon^*$ varies with $D$, suggesting three main conclusions. The first is that $\epsilon^*$ is a monotonically decreasing function of $D$, i.e. (5.20) establishes a dependence akin to the uncertainty principle of sampling theory: the smaller the image size, the larger the angular uncertainty of the recovered line parameters. Second, the angular error can be significant for most values of $D$ that would seem sensible as window sizes in the context of Algorithm 5.3, e.g. the error is greater than $3^o$ for $D \leq 20$ and greater that $1^o$ for $D \leq 60$. Finally, a comparison with Figure 5.5(c) suggests that the lower bound $\epsilon^*$ is tight. In the figure, $D = 20\sqrt{2} \approx 28.2$ and the angular error is between $1^o$ and $2^o$ (the Radon transform was computed with an angular step of $1^o$ and only one spurious line appears on each size of the true one). This is compatible with the lower bound $\epsilon^*$ which, from Figure 5.6, is somewhere between $1.5^o$ and $2^o$.

Overall, the analysis based on the strip model, enables significant insight on the fundamental limitation of thresholding algorithms: the fact they must satisfy conflicting constraints. On one hand, from (5.20), it is important that the image size $D$ be large in order to reduce the angular uncertainty of the recovered lines. On the other, when $D$ is large it is likely that the image (or window) will contain line segments of significantly different sizes.

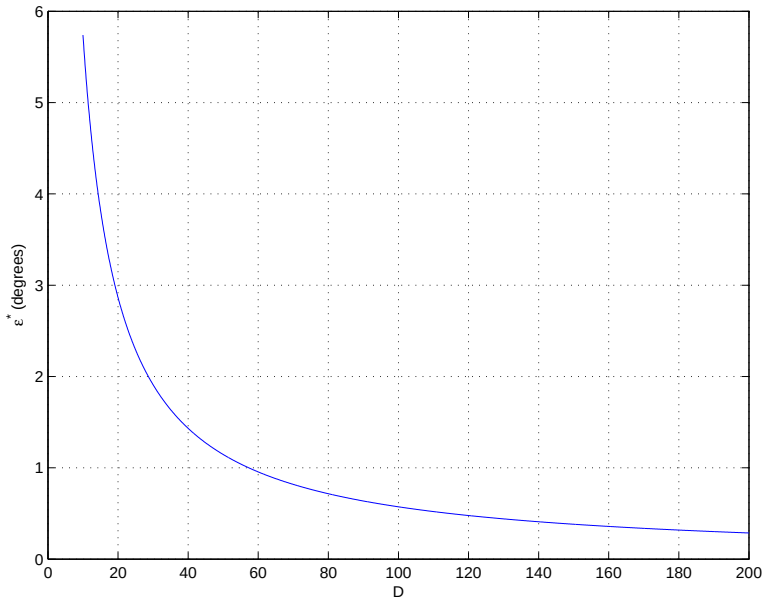


Figure 5.6: Dependence of the lower bound of angular error $\epsilon^*$ (in degrees) on the image size $D$ for a unit strip (width $w = 1$).

In this case, from (5.17), the recovery of the smaller ones requires sacrificing the angular accuracy with which the larger ones are recovered. Hence, for both small and large $D$, there will be a significant subset of lines whose parameters cannot be detected accurately. As we have seen in section 5.1.2, one possibility to overcome this fundamental limitation is to rely on an adaptive threshold. However, we have also seen that this alternative is not easy to implement. In particular, properly adapting the threshold would require some knowledge of the peak locations, which are exactly what needs to be determined. For these reasons, we next seek alternatives to the thresholding paradigm.

## 5.2 Line detection by matched filtering in Radon space

From the discussion of the previous section, it is clear that the Radon transform of a collection of strips exhibits two characteristics that present great challenges to the thresholding model. The first, is that the strip associated with line $(b_l, \theta_l)$ will originate not only a peak of $R(b, \theta)$ at $b = b_l$, $\theta = \theta_l$, but also a tail that decays with $\frac{1}{|\sin(\theta_l - \theta)|}$. As is visible in Figure 5.6, under the thresholding model, this decay is not fast enough to guarantee an acceptable angular accuracy of the recovered lines when the Radon transform is spatially localized (i.e. computed over a relatively small window). The second, visible in (5.13), is

that when the image (or window) contains multiple strips, all of them contribute to the Radon transform at any given $(b, \theta)$. Hence, by evaluating the magnitude of a given peak, it is impossible to make any inferences regarding properties of the associated line, e.g. its length. In this section, we argue that these problems can be significantly smaller when the Radon transform is replaced by its partial derivative with respect to $\theta$. We start by computing this partial derivative for the Radon transform of a strip.

**Lemma 5.2.** *Let $\mathcal{R}[\mathcal{B}(\boldsymbol{s})](b, \theta)$ be the Radon transform of the indicator function of strip $\boldsymbol{s} = (b_s, \theta_s, w_s)$, as given by (2.22). Then,*

$$\frac{\partial \mathcal{R}[\mathcal{B}(\boldsymbol{s})]}{\partial \theta}(b, \theta) = \frac{w_s}{|\sin(\theta_l - \theta)|} \cot(\theta_l - \theta), \quad \text{if } \theta \neq \theta_l. \tag{5.25}$$

*Proof:* Follows by differentiating (2.22) with respect to $\theta$. ∎

For $\theta = \theta_s$, the partial derivative above is not defined. However, as we have seen in the previous section, one never really deals with $\mathcal{R}[\mathcal{B}(\boldsymbol{s})](b, \theta)$ in practical applications. Instead, one has to deal with an upper bounded function, which is constant in the neighborhood of $\theta_s$. For compatibility with this practical scenario, we adopt the convention that

$$\frac{\partial \mathcal{R}[\mathcal{B}(\boldsymbol{s})]}{\partial \theta}(b, \theta_s) = 0. \tag{5.26}$$

Figure 5.7(a) shows a plot of (5.25) for $\boldsymbol{s} = \boldsymbol{s}_0 = (0, 0, 1)$ normalized by the value at $\theta = 1^o$. It can be seen from the figure that the derivative $\frac{\partial \mathcal{R}[\mathcal{B}(\boldsymbol{s})]}{\partial \theta}(b, \theta)$ has two main properties of interest. First, it decays fairly quickly, being approximately zero for $\theta$ such that $|\theta| \geq 20^o$. A comparison of the absolute value of (5.25) with $\mathcal{R}[\mathcal{B}(\boldsymbol{s})](b, \theta)$ (also normalized by its value at $\theta = 1^o$) is shown in (b). Notice how the derivative decays much faster than the Radon transform. This means that simply replacing the latter by the absolute value of the derivative would significantly reduce the two main problems for thresholding. The second property of interest is that (5.25) is a high-pass filter, i.e. a filter that will respond strongly to signals containing fast transitions and weakly to smooth signals. Due to this, using the interpretation of the autocorrelation function

$$\mathcal{AC}\{f(\theta)\} = \int f(\theta) f(\theta - \tau)\, d\tau \tag{5.27}$$

as the convolution of $f(\theta)$ with $f(-\theta)$, one would expect $\mathcal{AC}\{\frac{\partial \mathcal{R}[\mathcal{B}(\boldsymbol{s})]}{\partial \theta}(b, \theta)\}$ to have even faster decay than $\frac{\partial \mathcal{R}[\mathcal{B}(\boldsymbol{s})]}{\partial \theta}(b, \theta)$. This is indeed the case, as can be seen from Figure 5.8, where the autocorrelation function is compared to the Radon transform. Notice that the peak centered at $\theta = 0$ is narrower than that of Figure 5.7(b) and the side-lobes, having

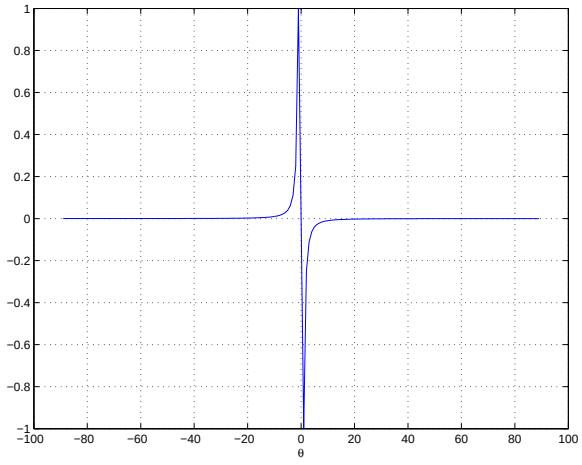


(a)

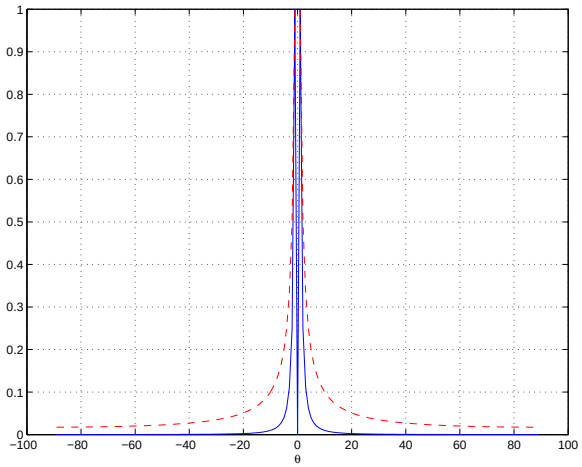


(b)

Figure 5.7: (a) Partial derivative of the Radon transform of the strip indicator function (5.25) with respect to $\theta$, as a function of $\theta$. (b) Comparison of the Radon transform of the strip indicator function (dashed) with the absolute value of its partial derivative with respect to $\theta$ (solid). Both curves are normalized by their value at $\theta = 1^o$.

negative amplitude, do not pose any problems for thresholding. In fact, given an edge map with multiple pixelated lines, the side-lobes of the peak associated with one line will suppress the contributions of peaks associated with other lines in that peak's neighborhood. This is both desirable and consistent with what is known about the human visual system.

These observations suggest the adoption of the following algorithm for line detection.

**Algorithm 5.4.** *Given the Radon transform of the pixelated edge map of an edge indicator function* $\mathcal{E}$*,*

$$r_{i,j} = \mathcal{R}\{\mathcal{E}\mathcal{M}[\mathcal{E}](\boldsymbol{x})\}(b_i, \theta_j),$$

*perform the following steps:*

1. *let*

$$h_k = \frac{\partial \mathcal{R}[\mathcal{B}(\boldsymbol{s})]}{\partial \theta}(0, \theta_k) \tag{5.28}$$

*where* $\theta_k = k\theta_s$*,* $\theta_s$ *is as defined in (4.4), and* $-\frac{Q}{9} \leq k \leq \frac{Q}{9}$*;*

2. *compute the correlation function*

$$c_{i,j} = \sum_{k=-\lfloor Q/9 \rfloor}^{\lfloor Q/9 \rfloor} r_{i,j+k} h_k; \tag{5.29}$$

3. *declare an edge with parameters* $(b_i, \theta_j)$ *if*

$$c_{i,j} \geq T \frac{c^* \mathfrak{L}(\boldsymbol{g}_{i,j})}{l^*}, \tag{5.30}$$

*where* $T \in [0, 1]$ *is a scaling factor,* $c^* = \max_{k,l} c_{k,l}$*,* $l^* = \max_{k,l} \mathfrak{L}(\boldsymbol{g}_{k,l})$*, and* $\boldsymbol{g}_{i,j} = \left(b_i, \theta_j, \mathcal{I}_{w,h}^{M,N}\right)$*.*

Two points are worth noting. The first is that this algorithm can be seen as a form of matched filtering. This is a technique widely used in digital communications to recover waveforms that have been corrupted by noise (e.g. due to transmitted over a communications channel). It can be shown that, under some generic assumptions on the signal and the noise, matched filtering is the optimal detection technique in the least-squares sense (VAN TREES (1968)). While we do not pursue here this alternative view of the edge detection problem, it indicates that the algorithm above should have some resilience against noisy edge maps. The second is that this algorithm can be combined with Algorithm 5.3 to achieve spatial localization (simply substitute "Algorithm 5.2" by "Algorithm 5.4" in the second step of Algorithm 5.3).

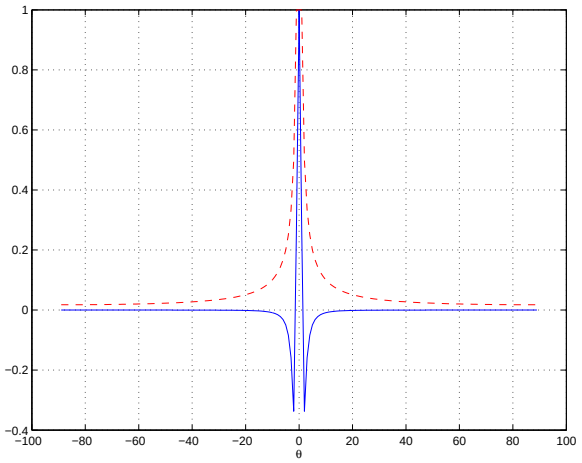


Figure 5.8: Comparison of the Radon transform of the strip indicator function (dashed) with the autocorrelation function of its partial derivative with respect to $\theta$ (solid). Both curves are normalized by their value at $\theta = 1^o$.

In spite of all the theoretical arguments in favor of thresholding the correlation function instead of the Radon transform itself, it turns out that the practical outcome is not very different. An example is shown in Figure 5.9 which presents the recovered lines when the algorithm is applied to the pixelated edge map of Figure 5.5(a), for two values of $T$. Notice that, in both cases, spurious lines are detected in the neighborhood of $\boldsymbol{l}_2$ or $\boldsymbol{g}$, but, for $T = 0.3$, it is already impossible to detect $\boldsymbol{l}_1$ and, for $T = 0.9$, both $\boldsymbol{l}_1$ and $\boldsymbol{g}$ are missed.

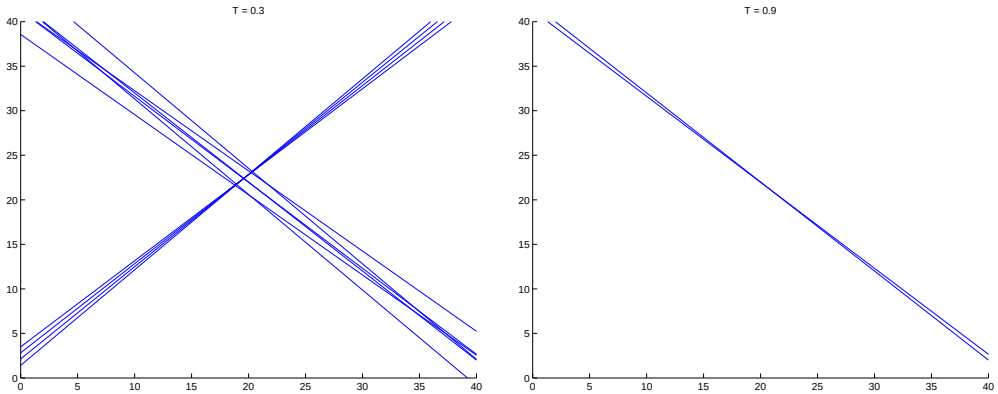


Figure 5.9: Lines recovered by Algorithm 5.4 with $T$ set to (a) 0.3 and (b) 0.9 when applied to the edge map of Figure 5.5.

The problem is that the actual Radon transform of the pixelated edge map (see Figure 5.5(b)) does not fully comply with the model derived from the strip. Notice, for example, that while (2.22) does not depend on $b$ when $\theta \neq \theta_s$ the same does not hold for the functions associated with each of the three peaks in Figure 5.5(b). In fact, for each $b$, these functions are null for certain intervals of $\theta$ and suddenly transition (at the extremes of these intervals) to the values predicted by (2.22). Given that, as discussed above, the filter $h_k$ is a high-pass filter, these transitions appear as peaks in the correlation function $c_{i,j}$, as can be seen from the contour plot shown in Figure 5.10. These peaks are responsible for the thresholding errors and, to account for them, we need to consider the model of the strip segment.

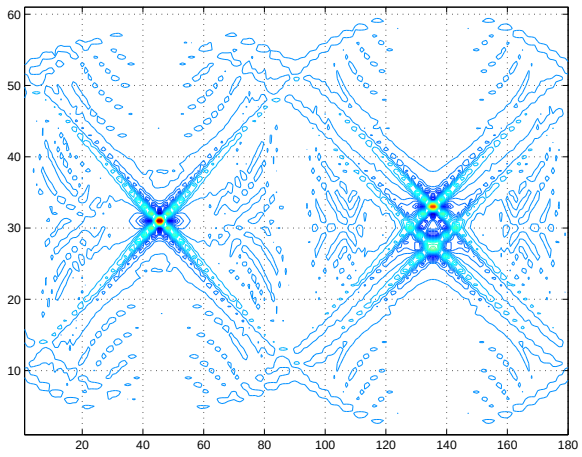


Figure 5.10: Contour plot of the correlation function produced by the application of Algorithm 5.4 to the edge map of Figure 5.5.

## 5.3 The strip segment model

The main limitation of the strip model for line detection is that it does not account for strips of bounded length. Since images are bounded sets, this is always the case in image analysis applications. The following lemma relates the Radon transforms of the strip and strip segment.

**Lemma 5.3.** *The Radon transform of the strip indicator function of the strip segment* $\boldsymbol{s}\big|_{\mathcal{I}_{w,h}^{M,N}}$, *where* $\boldsymbol{s} = (b_s, \theta_s, w_s)$, *satisfies the following conditions*

1. $\mathcal{R}\left\{\mathcal{B}\left[\boldsymbol{s}\big|_{\mathcal{I}_{w,h}^{M,N}}\right]\right\}(b,\theta) = \mathcal{R}\left\{\mathcal{B}[\boldsymbol{s}]\right\}(b,\theta)$, *if* $(b,\theta) \in \mathcal{FIS}\left(\boldsymbol{s}\big|_{\mathcal{I}_{w,h}^{M,N}}\right)$;

2. $\mathcal{R}\left\{\mathcal{B}\left[\boldsymbol{s}_{\left|\mathcal{I}_{w,h}^{M,N}\right.}\right]\right\}(b,\theta) \leq \mathcal{R}\left\{\mathcal{B}[\boldsymbol{s}]\right\}(b,\theta)$, *if* $(b,\theta) \in \mathcal{PIS}\left(\boldsymbol{s}_{\left|\mathcal{I}_{w,h}^{M,N}\right.}\right)$;

3. $\mathcal{R}\left\{\mathcal{B}\left[\boldsymbol{s}_{\left|\mathcal{I}_{w,h}^{M,N}\right.}\right]\right\}(b,\theta) = 0$, *if* $(b,\theta) \notin \mathcal{IS}\left(\boldsymbol{s}_{\left|\mathcal{I}_{w,h}^{M,N}\right.}\right)$;

*where* $\mathcal{R}\{\mathcal{B}[\boldsymbol{s}]\}(\cdot,\cdot)$ *is the Radon transform of the indicator function of strip* $\boldsymbol{s}$*, as given by (2.22), and* $\mathcal{IS}\left(\boldsymbol{s}_{\left|\mathcal{I}_{w,h}^{M,N}\right.}\right)$, $\mathcal{FIS}\left(\boldsymbol{s}_{\left|\mathcal{I}_{w,h}^{M,N}\right.}\right)$, *and* $\mathcal{PIS}\left(\boldsymbol{s}_{\left|\mathcal{I}_{w,h}^{M,N}\right.}\right)$ *are as in Definition 4.10.*

*Proof:* Since $\boldsymbol{s}_{\left|\mathcal{I}_{w,h}^{M,N}\right.} \subset \boldsymbol{s}$, it follows from Lemma 3.2 that

$$\mathcal{R}\left\{\mathcal{B}\left[\boldsymbol{s}_{\left|\mathcal{I}_{w,h}^{M,N}\right.}\right]\right\}(b,\theta) \leq \mathcal{R}\{\mathcal{B}[\boldsymbol{s}]\}(b,\theta), \forall (b,\theta).$$

This proves condition 2. The other two conditions follow from the definition of the Radon transform of $\mathcal{B}\left[\boldsymbol{s}_{\left|\mathcal{I}_{w,h}^{M,N}\right.}\right]$

$$\begin{aligned}
\mathcal{R}\left\{\mathcal{B}\left[\boldsymbol{s}_{\left|\mathcal{I}_{w,h}^{M,N}\right.}\right]\right\}(b,\theta) &= \int_{\mathbb{R}^2} \mathcal{B}\left[\boldsymbol{s}_{\left|\mathcal{I}_{w,h}^{M,N}\right.}\right] \delta(b - \boldsymbol{\xi}\cdot\boldsymbol{x})\, d\boldsymbol{x} \\
&= \int_{\mathcal{S}\left(\boldsymbol{s}_{\left|\mathcal{I}_{w,h}^{M,N}\right.}\right)} \delta(b - \boldsymbol{\xi}\cdot\boldsymbol{x})\, d\boldsymbol{x} \\
&= \int_{\mathcal{S}(\boldsymbol{s})\cap\mathcal{I}_{w,h}^{M,N}} \delta(b - \boldsymbol{\xi}\cdot\boldsymbol{x})\, d\boldsymbol{x}.
\end{aligned}$$

¿From Definition 4.9, when $\boldsymbol{l} = (b,\theta) \notin \mathcal{IS}\left(\boldsymbol{s}_{\left|\mathcal{I}_{w,h}^{M,N}\right.}\right)$, $\mathcal{S}(\boldsymbol{l}) \cap \mathcal{S}\left(\boldsymbol{s}_{\left|\mathcal{I}_{w,h}^{M,N}\right.}\right) = \emptyset$ and the integral is therefore zero. This leads to condition 3. From Definition 4.10, when $\boldsymbol{l} \in \mathcal{FIS}\left(\boldsymbol{s}_{\left|\mathcal{I}_{w,h}^{M,N}\right.}\right)$, $\mathcal{S}(\boldsymbol{l}) \cap \mathcal{S}(\boldsymbol{s}) \subset \mathcal{I}_{w,h}^{M,N}$, from which $\mathcal{S}(\boldsymbol{l}) \cap \mathcal{S}(\boldsymbol{s}) = \mathcal{S}(\boldsymbol{l}) \cap \mathcal{S}(\boldsymbol{s}) \cap \mathcal{I}_{w,h}^{M,N}$. It follows that

$$\begin{aligned}
\mathcal{R}\left\{\mathcal{B}\left[\boldsymbol{s}_{\left|\mathcal{I}_{w,h}^{M,N}\right.}\right]\right\}(b,\theta) &= \int_{\mathcal{S}(\boldsymbol{s})\cap\mathcal{I}_{w,h}^{M,N}} \delta(b - \boldsymbol{\xi}\cdot\boldsymbol{x})\, d\boldsymbol{x} \\
&= \int_{\mathcal{S}(\boldsymbol{s})} \delta(b - \boldsymbol{\xi}\cdot\boldsymbol{x})\, d\boldsymbol{x} \\
&= \mathcal{R}\{\mathcal{B}[\boldsymbol{s}]\}(b,\theta).
\end{aligned}$$

This leads to condition 1. ∎

The lemma provides an upper-bound to the Radon transform of the strip segment. While the bound is obviously tight outside the partially intersecting set, it can be quite loose inside this set. In particular, from (2.22), it goes to infinity as $\theta \to \theta_s$ and $|b - b_s| \leq \frac{w_s}{2}$.

This is clearly not the case for the Radon transform of the strip segment since the strip segment has bounded support. To derive a tighter bound, we start by considering the Radon transform of the indicator function of a rectangle.

**Lemma 5.4.** *Consider a rectangle $\boldsymbol{r}_{w\times h}$ with sides of length $w$ and $h$, its support set*

$$\mathcal{S}(\boldsymbol{r}_{w\times h}) = \{\boldsymbol{x} | \boldsymbol{x} \in \boldsymbol{r}_{w\times h}\},$$

*and the indicator function*

$$\mathbf{1}_{\mathcal{S}(\boldsymbol{r}_{w\times h})}(\boldsymbol{x}) = \begin{cases} 1 & \text{if } \boldsymbol{x} \in \mathcal{S}(\boldsymbol{r}_{w\times h}), \\ 0 & \text{otherwise.} \end{cases}$$

*The maximum value of the Radon transform of this indicator function, $\mathcal{R}\{\mathbf{1}_{\mathcal{S}(\boldsymbol{r}_{w\times h})}(\boldsymbol{x})\}$ is $\sqrt{w^2+h^2}$.*

*Proof:* Any rectangle $\boldsymbol{r}_{w\times h}$ can be transformed into the pixel $\boldsymbol{p}_0 = (0,0,w,h)$ by the application of a translation and a rotation. Since, from (2.7), this operation does not change the relative amplitudes of the Radon transform, the maximum of $\mathcal{R}\{\mathbf{1}_{\mathcal{S}(\boldsymbol{r}_{w\times h})}\}(b,\theta)$ is equal to that of $\mathcal{R}\{\mathcal{P}[\boldsymbol{p}_0]\}(b,\theta)$. From (2.27), and due to the symmetry of $\mathcal{R}\{\mathcal{P}[\boldsymbol{p}_0]\}(b,\theta)$, it suffices to consider values of $(b,\theta) \in [0,\infty] \times [0,\frac{\pi}{2}]$. To determine the maximum, it is necessary to consider the three equations of (2.27).

The first, $\frac{h}{\cos\theta}$, holds in a region where $\tan\theta \leq \frac{w}{h}$. In this region, it is a monotonically increasing function of $\theta$ and therefore reaches its maximum when $\tan\theta = \frac{w}{h}$ (since the tangent is a monotonically increasing function of $\theta$ in $[0,\frac{\pi}{2}]$). Using the equality

$$\cos\theta = \sqrt{\frac{1}{1+\tan^2\theta}},$$

it follows that the function is maximum when $\theta = \arctan\frac{w}{h}$ and the maximum is $\sqrt{w^2+h^2}$. The third, $\frac{w}{\sin\theta}$, holds in a region where $\tan\theta \geq \frac{w}{h}$. In this region, it is a monotonically decreasing function of $\theta$ and therefore also maximum when $\tan\theta = \frac{w}{h}$. Using

$$\sin\theta = \sqrt{\frac{\tan^2\theta}{1+\tan^2\theta}},$$

we, once again, obtain a maximum value of $\sqrt{w^2+h^2}$. The second, $\frac{1}{2}\frac{w\cos\theta+h\sin\theta-b}{\cos\theta\sin\theta}$, is a monotonically decreasing function of $b$, therefore maximum when $b=0$, in which case it becomes the average of the other two functions. Hence, it has maximum value $\sqrt{w^2+h^2}$, and this is also the overall maximum. ∎

We next use this result to derive an upper bound on the Radon transform of the indicator function of the strip segment.

**Lemma 5.5.** *If $\boldsymbol{s}$ is the strip $(b_s, \theta_s, w_s)$, then the Radon transform of the indicator function of the strip segment $\boldsymbol{s}\big|_{\mathcal{I}_{w,h}^{M,N}}$ is bounded by*

$$\mathcal{R}\left\{\mathcal{B}[\boldsymbol{s}|_{\mathcal{I}_{w,h}^{M,N}}]\right\}(b,\theta) \leq r_{max}\left(\boldsymbol{s}, \mathcal{I}_{w,h}^{M,N}\right), \tag{5.31}$$

*where*

$$r_{max}\left(\boldsymbol{s}, \mathcal{I}_{w,h}^{M,N}\right) = \begin{cases} \min\left(D, \sqrt{w_s^2 + \left(\mathcal{L}(b_s, \theta_s, \mathcal{I}_{w,s}^{M,N}) + w_s \tan\theta_s\right)^2}\right), \\ \qquad\qquad \textit{if } (b_s, \theta_s) \in \mathcal{R}_{\mathrm{I}} \\ \min\left(D, \sqrt{w_s^2 + \left(\mathcal{L}(b_s, \theta_s, \mathcal{I}_{w,s}^{M,N}) + w_s \cot\theta_s\right)^2}\right), \\ \qquad\qquad \textit{if } (b_s, \theta_s) \in \mathcal{R}_{\mathrm{II}} \\ \min\left(D, \sqrt{w_s^2 + \left(\mathcal{L}(b_s, \theta_s, \mathcal{I}_{w,s}^{M,N}) + \frac{w_s}{2}(\cot\theta_s + \tan\theta_s)\right)^2}\right), \\ \qquad\qquad \textit{if } (b_s, \theta_s) \in \mathcal{R}_{\mathrm{III}}, \end{cases}$$

*$\mathcal{L}(\cdot)$ is as defined in Theorem 5.1, $D$ as in (4.13), and $\mathcal{R}_{\mathrm{I}}, \mathcal{R}_{\mathrm{II}}$, and $\mathcal{R}_{\mathrm{III}}$ as defined in (4.7) - (4.9).*

*Proof:* Since $\boldsymbol{s}\big|_{\mathcal{I}_{w,h}^{M,N}} \subset \mathcal{I}_{w,h}^{M,N}$, it follows, from Lemma 3.2, that $\mathcal{R}\left\{\mathcal{B}\left[\boldsymbol{s}|_{\mathcal{I}_{w,h}^{M,N}}\right]\right\}(b,\theta) \leq \mathcal{R}\left[\mathbf{1}_{\{\mathcal{I}_{w,h}^{M,N}\}}\right](b,\theta)$. Hence, using the fact that $\mathcal{I}_{w,h}^{M,N}$ is a rectangle of dimensions $x_{max} \times y_{max}$ and applying Lemma 5.4, $\mathcal{R}\left\{\mathcal{B}\left[\boldsymbol{s}|_{\mathcal{I}_{w,h}^{M,N}}\right]\right\}(b,\theta) \leq D$. To prove the second component of the bound, consider $(b_s, \theta_s) \in \mathcal{R}_{\mathrm{III}}$, as illustrated in Figure 5.11. Then, there is a rectangle $\boldsymbol{r}$ with sides of length $w_s$ and $h + \frac{w_s}{2}\tan\theta_s + \frac{w_s}{2}\cot\theta_s$ such that $\boldsymbol{s}\big|_{\mathcal{I}_{w,h}^{M,N}} \subset \boldsymbol{r}$. From Lemma 3.2, it follows that $\mathcal{R}\left\{\mathcal{B}\left[\boldsymbol{s}|_{\mathcal{I}_{w,h}^{M,N}}\right]\right\}(b,\theta) \leq \mathcal{R}\left\{\mathcal{B}\left[\mathbf{1}_{\mathcal{S}(\boldsymbol{r})}\right]\right\}$ and, from Lemma 5.4, that $\mathcal{R}\left\{\mathcal{B}\left[\boldsymbol{s}|_{\mathcal{I}_{w,h}^{M,N}}\right]\right\}(b,\theta) \leq \sqrt{w_s^2 + (h + \frac{w_s}{2}\tan\theta_s + \frac{w_s}{2}\cot\theta_s)^2}$. Since $h$ is the length of the line segment $\left(b_s, \theta_s, I_{w,h}^{M,N}\right)$, (5.31) follows by application of Theorem 5.1. The proofs for the cases $(b_s, \theta_s) \in \mathcal{R}_{\mathrm{I}}$ and $(b_s, \theta_s) \in \mathcal{R}_{\mathrm{II}}$ are similar and omitted for brevity. ∎

The combination of Lemmas 5.3 and 5.5 leads to the following upper-bound for the Radon transform of the indicator function of the strip segment.

**Theorem 5.3.** *The Radon transform of the indicator function of the strip segment $\boldsymbol{s}\big|_{\mathcal{I}_{w,h}^{M,N}}$,*

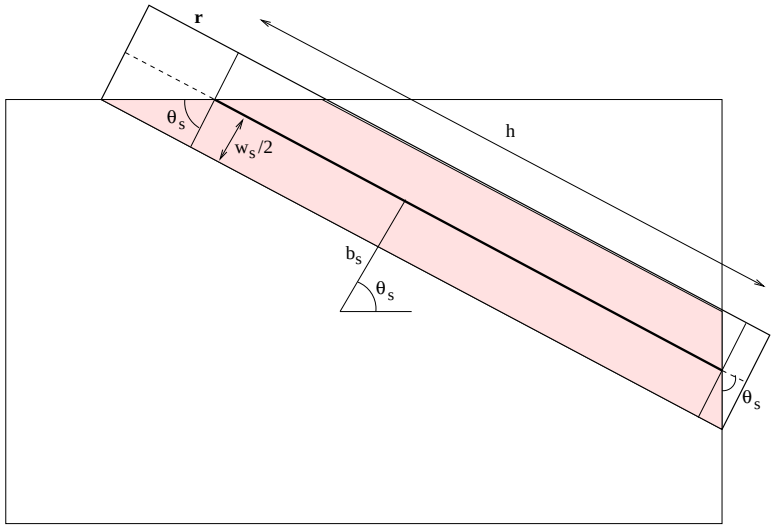


Figure 5.11: A strip segment in $\mathcal{R}_{III}$, and the bounding rectangle $\boldsymbol{r}$ used in the proof of Lemma 5.5.

*where* $\boldsymbol{s} = (b_s, \theta_s, w_s)$, *satisfies the following conditions*

1. $\mathcal{R}\left\{\mathcal{B}\left[\boldsymbol{s}\big|_{\mathcal{I}_{w,h}^{M,N}}\right]\right\}(b,\theta) = \frac{w_s}{|\sin(\theta-\theta_s)|}$, *if* $(b,\theta) \in \mathcal{FIS}\left(\boldsymbol{s}\big|_{\mathcal{I}_{w,h}^{M,N}}\right)$;
2. $\mathcal{R}\left\{\mathcal{B}\left[\boldsymbol{s}\big|_{\mathcal{I}_{w,h}^{M,N}}\right]\right\}(b,\theta) \le \frac{w_s}{|\sin(\theta-\theta_s)|}$, *if* $(b,\theta) \in \mathcal{PIS}\left(\boldsymbol{s}\big|_{\mathcal{I}_{w,h}^{M,N}}\right)$ *and* $|\theta-\theta_s| \ge \arcsin\frac{w_s}{r_{max}\left(\boldsymbol{s}, I_{w,h}^{M,N}\right)}$;
3. $\mathcal{R}\left\{\mathcal{B}\left[\boldsymbol{s}\big|_{\mathcal{I}_{w,h}^{M,N}}\right]\right\}(b,\theta) \le r_{max}\left(\boldsymbol{s}, I_{w,h}^{M,N}\right)$, *if* $(b,\theta) \in \mathcal{PIS}\left(\boldsymbol{s}\big|_{\mathcal{I}_{w,h}^{M,N}}\right)$ *and* $|\theta-\theta_s| < \arcsin\frac{w_s}{r_{max}\left(\boldsymbol{s}, I_{w,h}^{M,N}\right)}$;
4. $\mathcal{R}\left\{\mathcal{B}\left[\boldsymbol{s}\big|_{\mathcal{I}_{w,h}^{M,N}}\right]\right\}(b,\theta) = 0$, *if* $(b,\theta) \notin \mathcal{IS}\left(\boldsymbol{s}\big|_{\mathcal{I}_{w,h}^{M,N}}\right)$;

*where* $\mathcal{IS}\left(\boldsymbol{s}\big|_{\mathcal{I}_{w,h}^{M,N}}\right), \mathcal{FIS}\left(\boldsymbol{s}\big|_{\mathcal{I}_{w,h}^{M,N}}\right)$, *and* $\mathcal{PIS}\left(\boldsymbol{s}\big|_{\mathcal{I}_{w,h}^{M,N}}\right)$ *are as in Definition 4.10, and* $r_{max}\left(\boldsymbol{s}, I_{w,h}^{M,N}\right)$ *as in (5.31).*

*Proof:* Condition 4 follows from Lemma 5.3. To prove the remaining conditions, we start by noticing that for $(b,\theta) \in \mathcal{IS}\left(\boldsymbol{s}\big|_{\mathcal{I}_{w,h}^{M,N}}\right)$, it is never true that $\theta = \theta_s$ and $|b - b_s| > \frac{w_s}{2}$. Hence, from (2.22), if $(b,\theta) \in \mathcal{PIS}\left(\boldsymbol{s}\big|_{\mathcal{I}_{w,h}^{M,N}}\right)$ or $(b,\theta) \in \mathcal{FIS}\left(\boldsymbol{s}\big|_{\mathcal{I}_{w,h}^{M,N}}\right)$, then

$$\mathcal{R}\{\mathcal{B}[\boldsymbol{s}]\}(b,\theta) = \frac{w_s}{|\sin(\theta-\theta_s)|}. \tag{5.32}$$

This and condition 1 of Lemma 5.3 lead to condition 1 of the theorem. Furthermore, when $(b,\theta) \in \mathcal{PIS}\left(\boldsymbol{s}_{\left|\mathcal{I}_{w,h}^{M,N}\right.}\right)$, combining condition 2 of Lemma 5.3 with Lemma 5.5 leads to

$$\mathcal{R}\left\{\mathcal{B}\left[\boldsymbol{s}_{\left|\mathcal{I}_{w,h}^{M,N}\right.}\right]\right\}(b,\theta) \leq \min\left[\mathcal{R}\{\mathcal{B}[\boldsymbol{s}]\}(b,\theta), r_{max}\left(\boldsymbol{s}, I_{w,h}^{M,N}\right)\right].$$

But, from (5.32), $\mathcal{R}\{\mathcal{B}[\boldsymbol{s}]\}(b,\theta)$ is greater than $r_{max}\left(\boldsymbol{s}, I_{w,h}^{M,N}\right)$ if and only if

$$|\theta - \theta_s| < \arcsin \frac{w_s}{r_{max}\left(\boldsymbol{s}, I_{w,h}^{M,N}\right)}$$

and the theorem follows. ∎

It is interesting to analyze the conditions under which the bound above is not exact. Both conditions correspond to lines in $\mathcal{PIS}\left(\boldsymbol{s}_{\left|\mathcal{I}_{w,h}^{M,N}\right.}\right)$: while condition 3 applies to lines of angle close to $\theta_s$, condition 2 applies to lines whose angles are substantially different from $\theta_s$. In Lemmas 4.3 to 4.5 and Theorem 4.3, we have seen that

- the set $\mathcal{PIS}\left(\boldsymbol{s}_{\left|\mathcal{I}_{w,h}^{M,N}\right.}\right)$ is a band that extends the intersecting set of the line $\boldsymbol{l} = (b_s, \theta_s)$ along the $b$ dimension;
- the ratio of the width of this band to the width of $\mathcal{IS}\left(\boldsymbol{l}_{\left|\mathcal{I}_{w,h}^{M,N}\right.}\right)$ decays quickly as $\theta$ deviates from $\theta_s$.

Hence, condition 2 only really holds in a small sub-region of the region of support of $\mathcal{R}\left\{\mathcal{B}\left[\boldsymbol{s}_{\left|\mathcal{I}_{w,h}^{M,N}\right.}\right]\right\}(b,\theta)$. In that region, the Radon transform quickly decreases from $\frac{w_s}{|\sin(\theta-\theta_s)|}$ to zero. Furthermore, given the quick decay of $w_s|\sin(\theta-\theta_s)|$, condition 3 only holds for a small range of values of $\theta$ and, within this range, there is at least one point - $(b_s,\theta_s)$ - for which the Radon transform has amplitude $\mathcal{L}\left(b_s, \theta_s, \mathcal{I}_{w,h}^{M,N}\right)$. Since, from Lemma 5.5 and under the assumption that $w_s$ is significantly smaller than the image dimensions $(M,N)$, $r_{max}\left(\boldsymbol{s}, I_{w,h}^{M,N}\right)$ is also only slightly larger than this value, it follows that the bound above is tight. This implies that, for narrow strips, the Radon transform of the strip segment can be well approximated by the following function.

**Definition 5.1.** The *narrow strip approximation* (NSA) to the Radon transform of the

indicator function of the strip segment $\boldsymbol{s}\big|_{\mathcal{I}_{w,h}^{M,N}}$, where $\boldsymbol{s} = (b_s, \theta_s, w_s)$, is

$$\mathcal{NSA}\left\{\mathcal{B}\left[\boldsymbol{s}\big|_{\mathcal{I}_{w,h}^{M,N}}\right]\right\}(b,\theta) = \begin{cases} 0, & \text{if } (b,\theta) \notin \mathcal{IS}\left(\boldsymbol{l}\big|_{\mathcal{I}_{w,h}^{M,N}}\right) \\ \frac{w_s}{|\sin(\theta-\theta_s)|}, & \text{if } (b,\theta) \in \mathcal{IS}\left(\boldsymbol{l}\big|_{\mathcal{I}_{w,h}^{M,N}}\right) \\ & \text{and } |\theta-\theta_s| \geq \arcsin \frac{w_s}{r_{max}\left(\boldsymbol{s}, I_{w,h}^{M,N}\right)} \\ r_{\max}\left(\boldsymbol{s}, I_{w,h}^{M,N}\right), & \text{if } (b,\theta) \in \mathcal{IS}\left(\boldsymbol{l}\big|_{\mathcal{I}_{w,h}^{M,N}}\right) \\ & \text{and } |\theta-\theta_s| \leq \arcsin \frac{w_s}{r_{max}\left(\boldsymbol{s}, I_{w,h}^{M,N}\right)} \end{cases}$$

where $\mathcal{IS}\left(\boldsymbol{s}\big|_{\mathcal{I}_{w,h}^{M,N}}\right)$ is as in Definition 4.10, and $r_{max}\left(\boldsymbol{s}, I_{w,h}^{M,N}\right)$ as in (5.31).

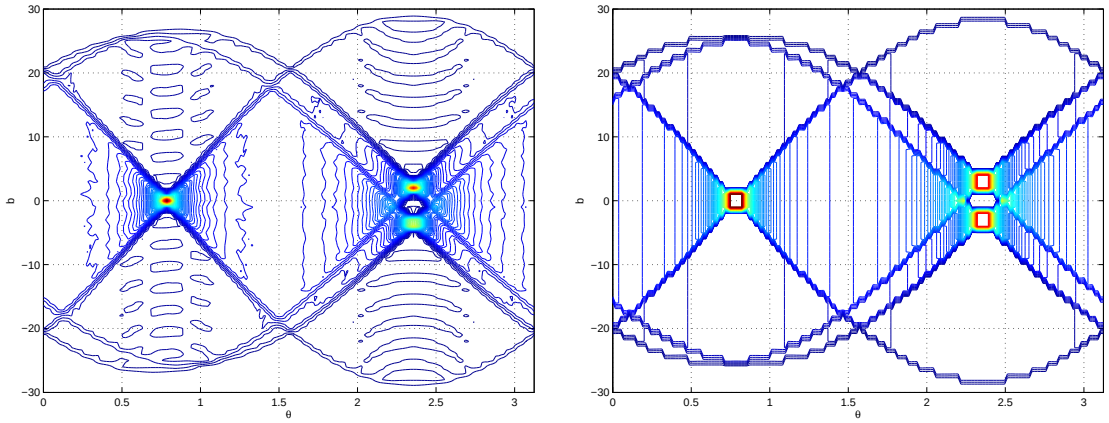


Figure 5.12: Left: Radon transform of the image shown in Figure 5.5 (a). Right: its NSA. Notice that, for each pixelated line, the NSA is very close to the Radon transform everywhere but in its tails, where the amplitude of the Radon transform is quite small.

In fact, as illustrated by Figure 5.12, the NSA is a close approximation to the Radon transform of the pixelated line. The goodness of this approximation suggests the following algorithm for line detection.

**Algorithm 5.5.** *Given the Radon transform of the pixelated edge map of an edge indicator function $\mathcal{E}$,*

$$r_{i,j} = \mathcal{R}\{\mathcal{EM}[\mathcal{E}](\boldsymbol{x})\}(b_i, \theta_j),$$

*and the number of pixelated lines $N$ that it contains, perform the following steps:*

1. *set $k = 0, \mathcal{RP}_{i,j} = 0, \forall(i,j).$;*

2. *while* $k < N$

   - *compute* $\Delta r_{i,j} = r_{i,j} - \mathcal{RP}_{i,j}$
   - *let* $(i^*, j^*) = \arg\max_{i,j} \Delta r_{i,j}$
   - *let* $(b_k^*, \theta_k^*) = (b_{i^*}, \theta_{j^*})$
   - $\mathcal{RP}_{i,j} = \sum_{m=1}^{k} \mathcal{NSA}\left\{\mathcal{B}\left[\boldsymbol{s}\big|_{\mathcal{I}_{w,h}^{M,N}}\right]\right\}(b_m^*, \theta_m^*), \forall(i,j);$

3. *return the parameters* $(b_k^*, \theta_k^*), k = 1, \ldots, N.$

This algorithm implements an *analysis-by-synthesis* (ABS) procedure. A new line is detected at each iteration of loop 2 by locating the largest peak of the difference Radon transform $\Delta r_{i,j}$ (analysis step). The latter is the difference between the Radon transform and its current best estimate, $\mathcal{RP}_{i,j}$, and is initially equal to the Radon transform. The NSA is then synthesized according to the parameters of this line (synthesis step) and added to $\mathcal{RP}_{i,j}$. The new estimate is subtracted to the original Radon transform to obtain an updated $\Delta r_{i,j}$ and the process is iterated until $N$ lines are detected. Note that each time a new line NSA is added to the current best estimate and the updated estimate subtracted from the Radon transform, the contributions to the latter from all previously detected lines are canceled and do not appear in $\Delta r_{i,j}$. Hence, the application of the maximum operator is sufficient to detect the next largest line not yet uncounted for. This is drastically different from the thresholding algorithms where the tails of the Radon transform are never explicitly modeled nor suppressed and, therefore, originate spurious detections. Trying to eliminate those spurious detections is usually not easy, and even quite involved heuristics can lead to poor performance. In the following section, we present experimental evidence supporting this claim.

## 5.4 Experimental procedure

We conducted a series of experiments to compare the performance of the various line detection algorithms discussed so far. In order to have unambiguous ground truth about how many lines were present in a given test image and what their parameters were, we relied on synthetically generated edge maps. The procedure used to generate these images was the following.

1. An image size of $40 \times 40$ pixels was selected.

2. The admissible set computed according to (4.6) and a set of $k$ line parameter vectors $(b_i, \theta_i), i = 1, \ldots, k$, drawn independently with uniform probability over this admissible set.

3. An image was created containing the $k$ pixelated lines defined by the parameters above.

4. Salt-and-pepper noise was added by randomly reversing the state of each image pixel with a given probability $p$.

5. A line detection algorithm was applied to the image, and $k$ line parameter vectors recovered. Each line was classified as correctly detected if

$$||(b, \theta) - (\hat{b}, \hat{\theta})|| \leq 2,$$

where $(b, \theta)$ are the true line parameters and $(\hat{b}, \hat{\theta})$ the recovered ones. Otherwise, it was classified as an error.

6. Steps 1-5 were repeated 500 times for each of the possible combinations of $k \in \{2, \ldots, 5\}$ and $p \in \{0, 0.01, 0.02, 0.03, 0.04, 0.05\}$.

Figure 5.13 presents some example synthetic images obtained with $k = 2$ for the different values of $p$ considered. Various line detectors were evaluated. Preliminary results showed that the straightforward implementation of the thresholding methods (Algorithms 5.2 and 5.4) does not reach acceptable levels of detection error. The typical problem is that the largest line originates various false-positives at locations where the amplitude of the Radon transform is stronger than that of the peaks associated with the remaining lines. For this reason we have implemented various heuristics, commonly used in the image processing literature, to clean up the thresholding results.

The first was the use of morphological operators, namely the *thinning operator* (JAIN (1989)). Since the Radon transform gradually decreases from the maximum value associated with the correct parameters, thresholding always leads to a cluster of false positives around the location of the maximum. Thinning is an operator that removes pixels from a set until only a narrow subset remains. It is commonly used, in shape analysis, to obtain the so-called skeleton of a binary shape and, in edge detection, to clean the edge map by reducing all lines to single pixel thickness. In the context of line detection, it can be used to eliminate false-positives by reducing the size of the cluster of detections around the maximum location. This is illustrated in Figure 5.14 where we show the clusters formed

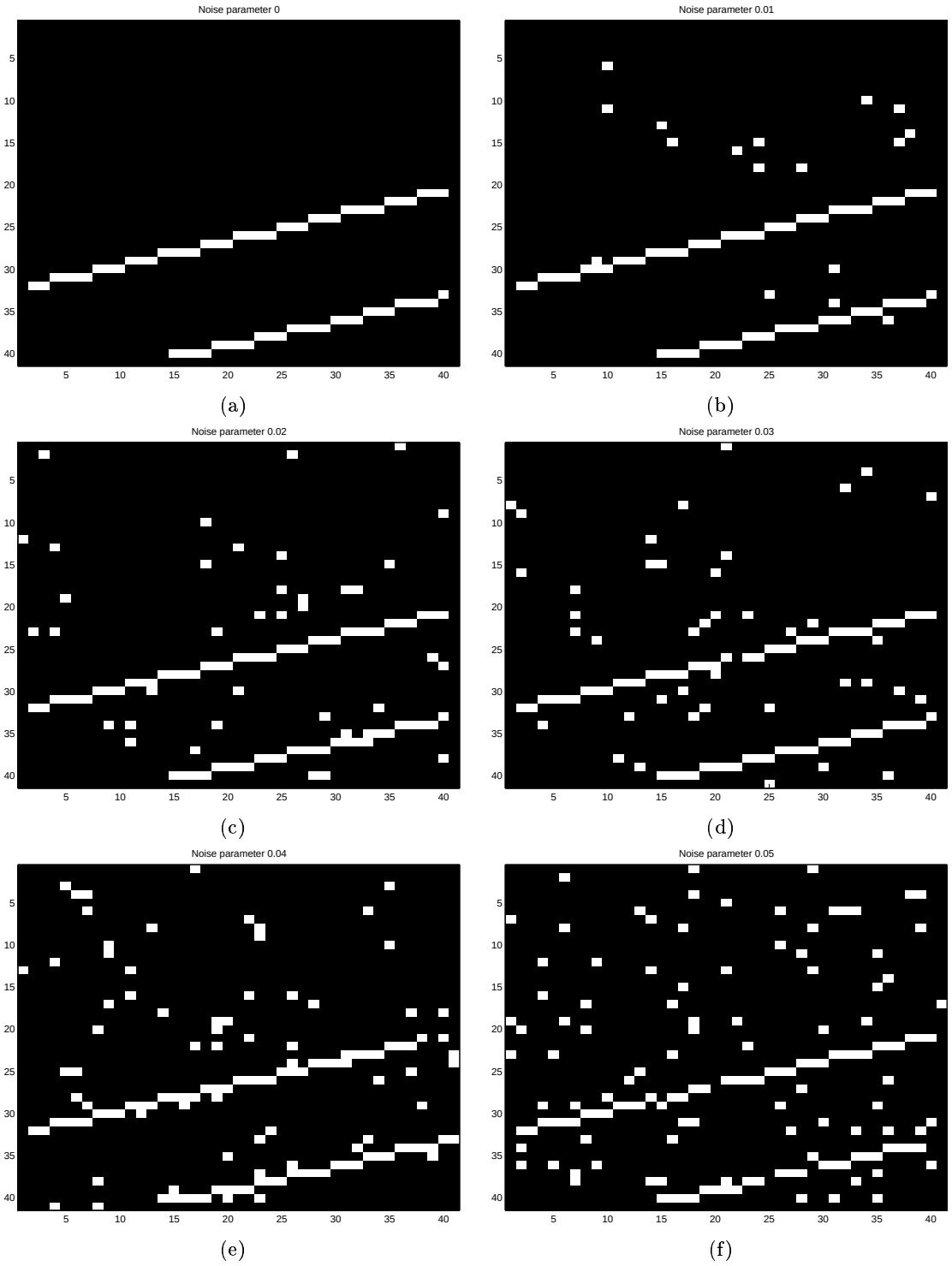


Figure 5.13: Synthetic images with two pixelated lines and salt-and-pepper noise. Probabilities of state reversal: (a) 0, (b) 0.01, (c) 0.02, (d) 0.03, (e) 0.04, and (f) 0.05.

by thresholding the Radon transform of Figure 5.12 (left) and the result of the thinning operation. Thinning reduces the number of false positives, but there are no guarantees that they will be completly eliminated.

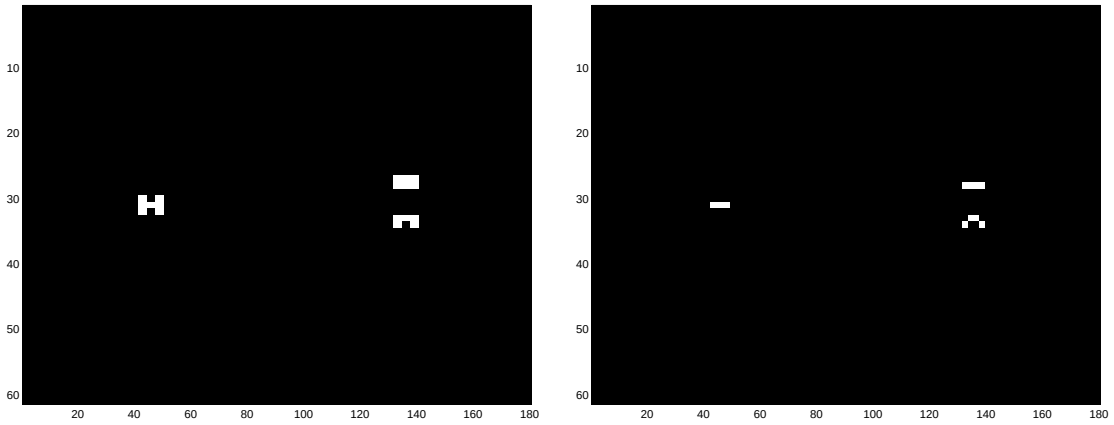


Figure 5.14: Left: binary map originated by tresholding the Radon transform shown in the left of Figure 5.12. Right: corresponding map after thinning.

The second was the combination of a *maximum detector* with the thresholding process. This consisted of centering a $3 \times 3$ pixel window on each location of the $(b, \theta)$ plane where a line was detected (Radon transform above the threshold) and accepting the detection only if the amplitude of the Radon transform at the central location was the largest in the window. Once again, the goal was to eliminate the clusters of false positives that thresholding originates in the neighborhood of the maximum. Figure 5.15 illustrates the results of this procedure on the Radon transform of Figure 5.14 (left).

Finally, we experimented with various statistical clustering methods. Since image lines are points in $(b, \theta)$-space and the false positives are mostly created by clusters around each true maximum, a statistical clustering procedure such as the *k-means* algorithm (DUDA AND HART (1973)) should be able to identify the cluster centers. This turned out, however, to be quite problematic. In images containing man-made structure (e.g. buildings or other objects), lines tend to concentrate in a few directions (e.g. horizontal and vertical) and it is common to find many parallel lines separated by a small distance along the $b$ dimension (especially when the objects are distant from the camera). In these cases, the clusters tend to be elongated and each line contributes to the value of the Radon transform at the locations of other lines by a non-negligible amount. Hence, there can be significant cluster overlap and the cluster structure can be difficult to infer. This leads to poor performance by

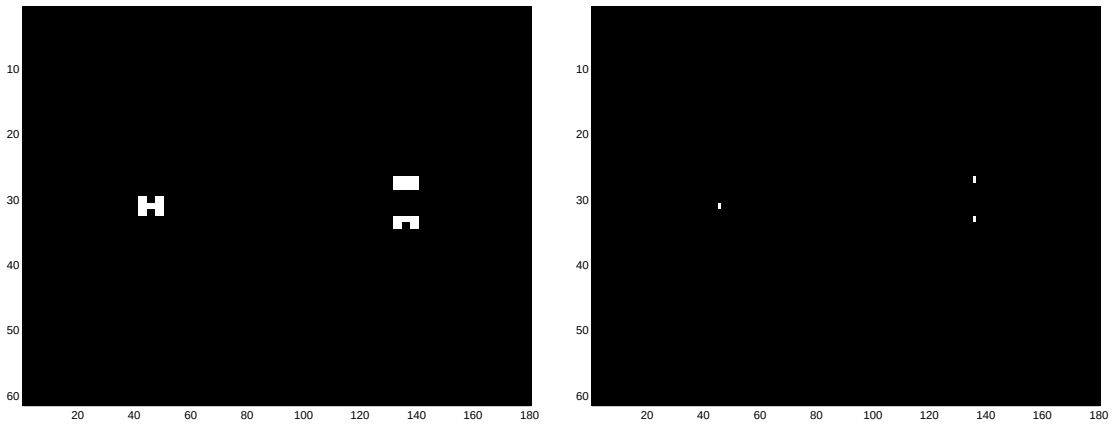


Figure 5.15: Left: binary map originated by tresholding the Radon transform shown in the left of Figure 5.12. Right: corresponding map after maximum detection.

standard clustering algorithms. We have tried several variants but never with satisfactory results or even results comparable to those of the two heuristics described above. Since clustering methods are also much more expensive from a computational point of view, we will not consider them in what follows.

## 5.5 Experimental results

In this section, we report the results of a study comparing the performance of six line detection procedures based on: 1) Algorithm 5.5, which we will refer to as analysis-by-synthesis (ABS), 2) Algorithm 5.2, which we denote by thresholding (TH), and 3) Algorithm 5.4 which will be denoted by matched filtering followed by thresholding (MF+TH). The six procedures were obtained by combining these base algorithms with the post-processing heuristics discussed above:

1. plain ABS;
2. plain TH;
3. TH + Thin;
4. MF + TH;
5. MF + TH + Thin;
6. MF + TH + MX;

where Thin means morphological thinning, and MX means maximum detection. Figure 5.16 presents a comparison of the performance of the six procedures, in terms of the probability of line detection error as a function of the salt-and-pepper noise probability $p$ for images containing 2 to 5 pixelated lines. Four interesting observations can be made from the figure.

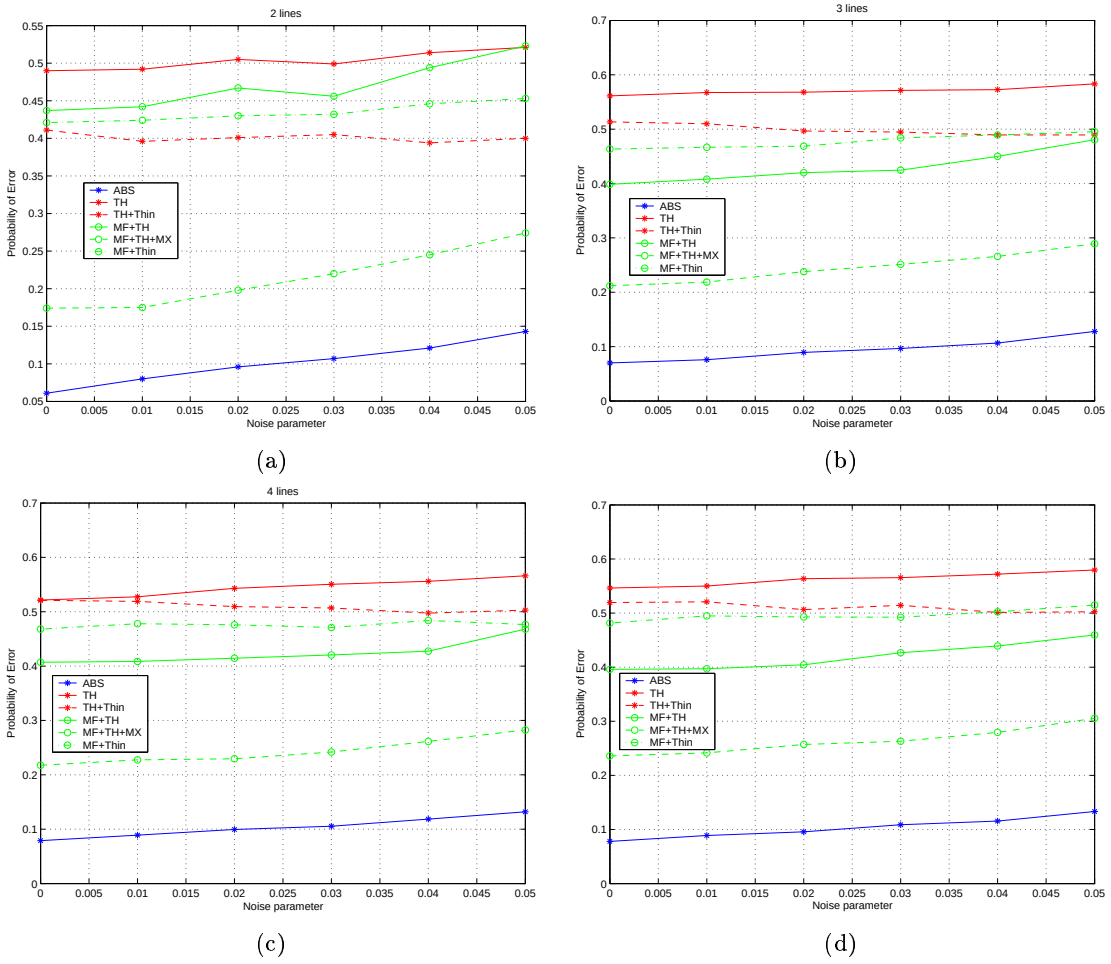


Figure 5.16: Probability of error as a function of change of state probability due to noise for the six line detection procedures discussed in the text. Results are shown for images with 2 (a), 3 (b), 4 (c), and 5 (d) pixelated lines.

The first is that the ABS algorithm clearly outperforms all combinations of thresholding plus heuristics. The performance improvements of the former can be very significant: up to a 10-fold decrease in probability of error over the remaining techniques. The second is that the probability of error achieved by the ABS algorithm is quite insensitive to the noise level $p$ and the number of pixelated lines in the edge map. This indicates that

the ABS algorithm is robust to variations in these parameters. The third is that, of the heuristic solutions, the only that performs close to ABS is procedure 6 (MF+TH+MX). Nevertheless, the probability of error of this procedure is still about twice that of ABS. For the remaining heuristic solutions, the probability of error is usually more than four times that of ABS. The fourth observation is that the procedures using matched filtering tend to do better than those based in straightforward thresholding. This is due to the faster decay of the filtered Radon transform that leads to smaller tails and less interference between the contributions from the different lines. However, as the figure clearly shows, matched filtering does not completely eliminate the problem, which can only be fully addressed by the explicit modeling of the Radon transform, as is done (through the NSA) in the ABS procedure.

## 5.6 Line detection examples

We finalize this chapter with some line detection examples using the ABS algorithm. Figure 5.17 presents three images containing both significant line structure and richly textured areas and the associated edge maps (computed by the Canny edge detector (CANNY (1986))). Textured areas usually pose problems to line detection algorithms since edge detectors tend to produce many false positives in textured regions. The resulting spurious edge pixels can lead to false positives for line detection. Figure 5.18 presents the first $N$ lines detected by the ABS algorithm when $N \in \{25, 50\}$. While we lack absolute ground truth for the evaluation of line detection in these images, it is clear that the number of false positives is quite small even when $N = 50$.

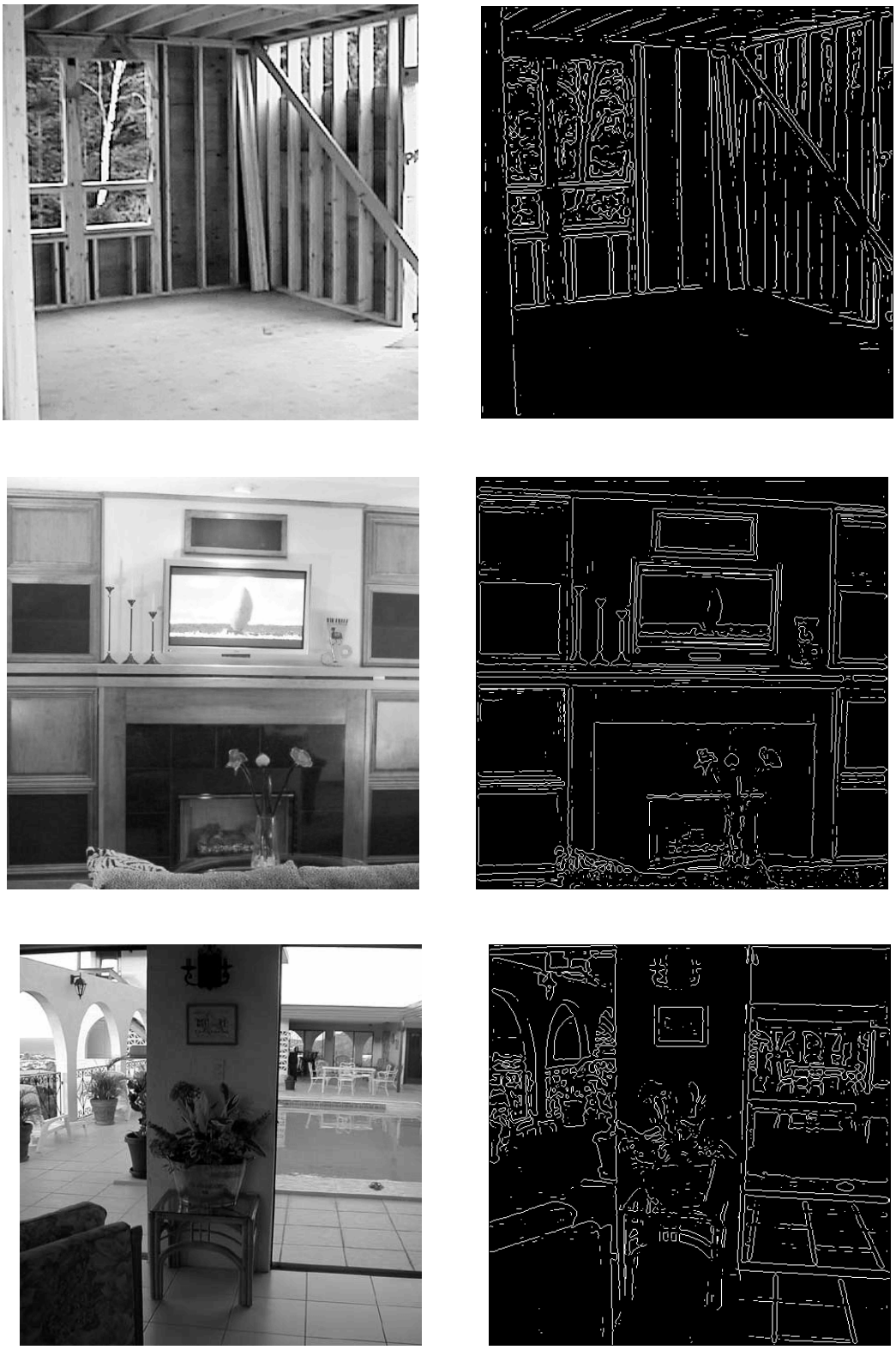

Figure 5.17: Three images (left column) and associated edge maps (right).

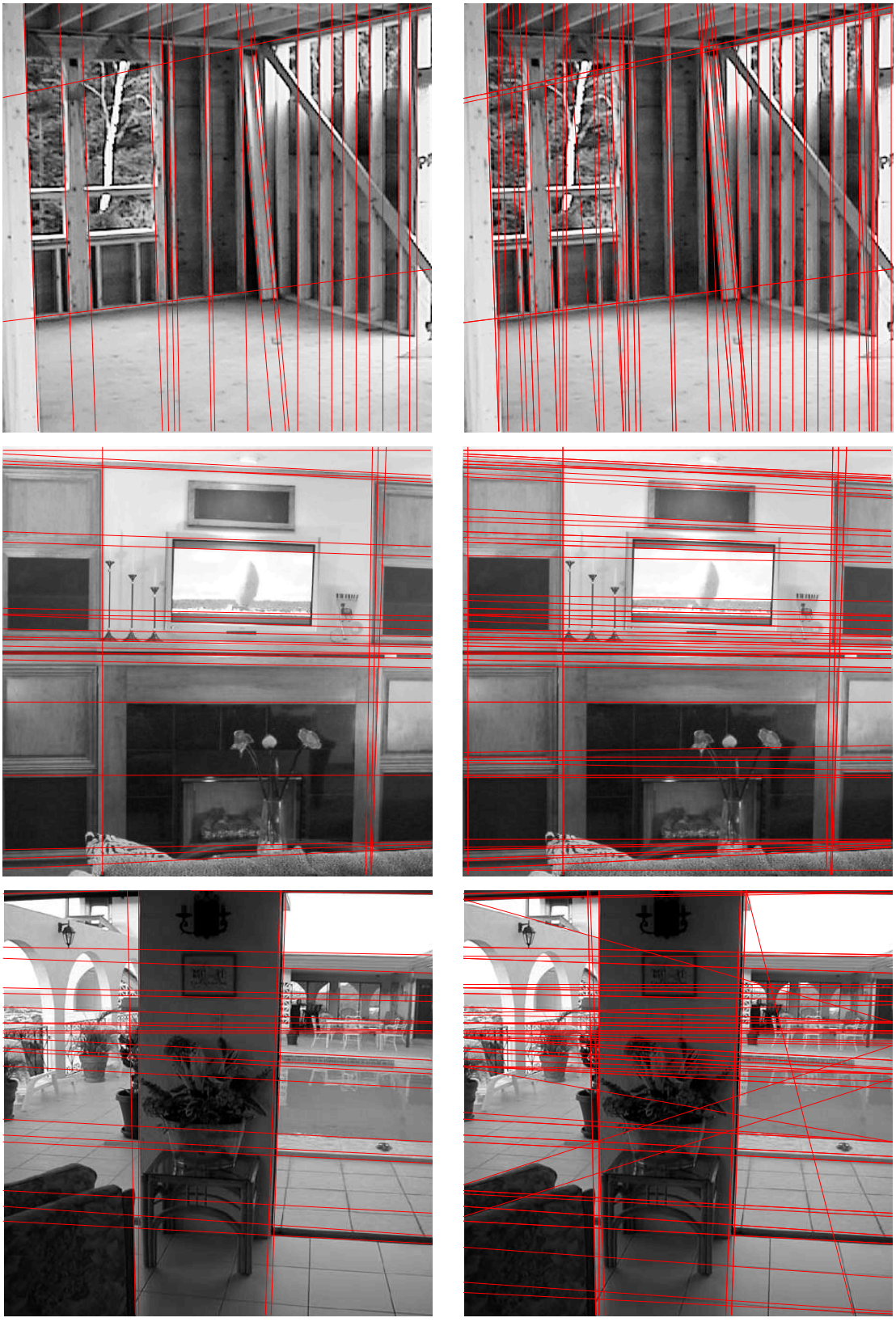

Figure 5.18: Line detection with the ABS algorithm on the three images of Figure 5.17. Left column: first 25 recovered lines are shown superimposed on the image. Right column: same for 50 lines.

# Chapter 6

# Probabilistic models for the Radon transform of pixelated lines

In the previous chapter, we have characterized analytically the Radon transform of a pixelated edge map given an edge indicator function. However, for most uses of the Radon transform in computer vision, the edge indicator function is not known and has to be itself determined from the observed images. This is an inference problem and, since there are usually various source of uncertainty (e.g. unknown number of lines, unknown line parameters) and noise (sensor noise, edge detection noise, image regions without edges but strongly textured), is naturally formulated as a problem of statistical inference. Such formulation involves assigning a measure to the space of edge indicator functions, and deriving statistically optimal procedures for determining the various unknowns.

In this chapter, we start from the simplest measure on the space of indicator functions (a uniform distribution that makes all lines equally likely) and derive closed-form expressions for various statistics of the Radon transform of pixelated edge maps: its probability density function, first- and second-order moments, and the probability density function of its sample mean. This statistical characterization is a significant result in the sense that it proves the existence of a statistical law which governs the amplitudes of the range function of the Radon transform. The existence of such laws, for many transforms commonly used in vision, has been argued by various authors in the recent past (Huang and Mumford (1999); Portilla and Simoncelli (2000); Grenander and Srivastava (2001)). We present a derivation from first principles that, to the best of our knowledge, was previously unavailable for the Radon transform.

As in the previous chapter, the existence of a sound characterization of the (statistical)

properties of the Radon transform enables the design of sophisticated inference algorithms. We illustrate this point by picking up where we left off in the previous chapter: an optimal algorithm, in the minimum probability of error sense, to determine the number of pixelated lines in a given edge map. This allows the application of the ABS line detection algorithm of the previous chapter to local image neighborhoods. The result of integrating the two algorithms is a line detection procedure that is capable of providing spatially localized line estimates.

## 6.1 A probability density function for the Radon transform

To achieve a statistical characterization of the Radon transform, we restrict our attention to the simplest possible measure, or *prior*, for edge indicator functions: the one which assumes that all lines are drawn independently.

**Definition 6.1.** Consider the edge map $\mathcal{EM}[\mathcal{E}](\mathbf{x})$ associated with an edge indicator function $\mathcal{E}$ defined on $\mathcal{I}_{w,h}^{M,N}$. $\mathcal{E}$ is denoted as an *independent and identically distributed (iid) edge indicator function* when, for any line $n$-tupple $\boldsymbol{l} = \{\boldsymbol{l}_1, \ldots, \boldsymbol{l}_n \,|\, \boldsymbol{l}_i \in \mathcal{A}(x_{max}, y_{max})\}$, the probability density function of $\boldsymbol{l}$ satisfies the following condition

$$p_{\boldsymbol{l}_1,\ldots,\boldsymbol{l}_n}[\mathcal{E}(\boldsymbol{l}_1, \ldots, \boldsymbol{l}_n) = \prod_{i=1}^{n} p_{\boldsymbol{l}}[\mathcal{E}(\boldsymbol{l}_i)]. \tag{6.1}$$

If $p_{\boldsymbol{l}}[\mathcal{E}(\boldsymbol{l}_i)] = \kappa, \forall \boldsymbol{l}_i \in \mathcal{A}(x_{max}, y_{max})$, where $\kappa$ is a constant, the edge indicator function is *uniformly distributed*.

We acknowledge that the assumptions of independence and uniformity may not always be appropriate. In fact, most images tend to exhibit geometric structure in the form of mostly parallel or perpendicular line arrangements, as well as dominant line orientations. In these cases, both the independence and uniformity assumptions will be unrealistic. Nevertheless, these assumptions can be quite useful because they simplify the problem considerably and allow insights that would otherwise be difficult to attain. For this reason, we restrict our attention to the set of edge indicator functions that are uniform and iid (uiid). We start by deriving the value of the constant $\kappa$.

**Lemma 6.1.** *Let $\mathcal{E}$ be a uiid edge indicator function according to Definition 6.1. Then,*

$$p_{\boldsymbol{l}}(b, \theta) = \begin{cases} \kappa & \text{if } (b, \theta) \in \mathcal{A}(x_{max}, y_{max}) \\ 0 & \text{otherwise,} \end{cases} \tag{6.2}$$

*where* $\mathcal{A}(x_{max}, y_{max})$ *is as given by Definition 4.3,*

$$\kappa = \frac{1}{4\sqrt{2}D\cos\left(\frac{\pi}{4} - \phi\right)}, \tag{6.3}$$

*and* $D$, $\phi$ *as in (4.13).*

*Proof:* Consider a line $\boldsymbol{l} = (b, \theta)$. If $\boldsymbol{l} \notin \mathcal{A}(x_{max}, y_{max})$, then $p_{\boldsymbol{l}}(b, \theta) = 0$. Now, if $\boldsymbol{l} \in \mathcal{A}(x_{max}, y_{max})$,

$$\begin{aligned}
p_{\boldsymbol{l}}(b,\theta) &= \frac{1}{\int_0^{\pi}\int_{(b,\theta)\in\mathcal{A}(x_{max},y_{max})} dbd\theta} \\
&= \frac{1}{2\int_0^{\pi}(x_{max}|\cos\theta| + y_{max}|\sin\theta|)d\theta} \\
&= \frac{1}{2\int_0^{\pi/2}(y_{max}\sin\theta + x_{max}\cos\theta)d\theta \;+\; 2\int_{\pi/2}^{\pi}(y_{max}\sin\theta - x_{max}\cos\theta)d\theta} \\
&= \frac{1}{2D\int_0^{\pi/2}(\sin\phi\sin\theta + \cos\phi\cos\theta)d\theta \;+\; 2D\int_{\pi/2}^{\pi}(\sin\phi\sin\theta - \cos\phi\cos\theta)d\theta} \\
&= \frac{1}{2D\left[\int_0^{\pi/2}\cos(\phi-\theta)d\theta \;-\; \int_{\pi/2}^{\pi}\cos(\phi+\theta)d\theta\right]},
\end{aligned}$$

with $D$ and $\phi$ as in (4.13). The lemma follows after some algebraic manipulation. ∎

Since the Radon transform of a pixelated edge map is a deterministic function of the associated set, $\mathcal{E}^{-1}(1)$, of edges, a measure on the space of edge indicator functions induces a measure on the range space of the Radon transform. We next derive the probability density function associated with the latter when that associated with the former is (6.2). For this, we need some intermediate definitions and results.

**Definition 6.2.** The *width of the intersecting set* $\mathcal{IS}\left(\boldsymbol{l}, \mathcal{I}_{w,h}^{M,N}\right)$ of the line $\boldsymbol{l} = (b_l, \theta_l)$ at $\theta$ is

$$\mathfrak{w}_{\boldsymbol{l}}(\theta) = b_{sup}(\theta, b_l, \theta_l) - b_{inf}(\theta, b_l, \theta_l) \tag{6.4}$$

where $b_{sup}(\cdot)$ and $b_{inf}(\cdot)$ are as defined in Theorem 4.1.

The following lemma shows that the width of the intersecting set of a line is determined by a simple function of its length and direction.

**Lemma 6.2.** *The width of the intersecting set of line* $\boldsymbol{l} = (b_l, \theta_l)$ *is*

$$\mathfrak{w}_{\boldsymbol{l}}(\theta) = \mathfrak{L}(b_l, \theta_l)\,|\sin(\theta_l - \theta)|, \tag{6.5}$$

*where* $\mathcal{L}(\cdot)$ *is defined in Theorem 5.1.*

*Proof:* Consider the four different cases in the proof of Theorem 4.1. For cases **i)** and **ii)**, i.e. when $|b_l| \leq \left| y_{max}|\sin\theta_l| - x_{max}|\cos\theta_l| \right|$, the results are straightforward. Consider now the remaining two cases. For case **iii)**,

$$\begin{aligned} b_{sup} - b_{inf} &= |\sin(\theta_l - \theta)| \left( \frac{x_{max}}{|\sin(\theta_l)|} + \frac{y_{max}}{|\cos(\theta_l)|} \right) + |b_l| \left( \frac{\sin\theta}{|\sin(\theta_l)|} + \frac{\cos\theta}{|\cos(\theta_l)|} \right) \\ &= |\sin(\theta_l - \theta)| \left( \frac{x_{max}}{|\sin(\theta_l)|} + \frac{y_{max}}{|\cos(\theta_l)|} \right) - 2|b_l| \frac{\sin(\theta_l - \theta)}{\sin(2\theta_l)}. \end{aligned}$$

Since $\text{sign}[\sin(\theta_l - \theta)] = \text{sign}[\sin(2\theta_l)]$, then

$$b_{sup} - b_{inf} = |\sin(\theta_l - \theta)| \left( \frac{x_{max}}{|\sin(\theta_l)|} + \frac{y_{max}}{|\cos(\theta_l)|} \right) - 2|b_l| \left| \frac{\sin(\theta_l - \theta)}{\sin(2\theta_l)} \right|.$$

Similarly, for case **iv)**, and since $\text{sign}[\sin(\theta_l - \theta)] = -\text{sign}[\sin(2\theta_l)]$,

$$\begin{aligned} b_{sup} - b_{inf} &= |\sin(\theta_l - \theta)| \left( \frac{x_{max}}{|\sin(\theta_l)|} + \frac{y_{max}}{|\cos(\theta_l)|} \right) + 2|b_l| \frac{\sin(\theta_l - \theta)}{\sin(2\theta_l)} \\ &= |\sin(\theta_l - \theta)| \left( \frac{x_{max}}{|\sin(\theta_l)|} + \frac{y_{max}}{|\cos(\theta_l)|} \right) - 2|b_l| \left| \frac{\sin(\theta_l - \theta)}{\sin(2\theta_l)} \right|, \end{aligned}$$

and the lemma follows. ∎

One interesting consequence of this lemma is that, given a line $\boldsymbol{l}$, the probability that a line $\boldsymbol{l}'$ will belong to its intersecting set is proportional to its length.

**Lemma 6.3.** *Consider a line $\boldsymbol{l} = (b_l, \theta_l) \in \mathcal{A}(x_{max}, y_{max})$. The probability that a line $\boldsymbol{l}'$ drawn randomly according to (6.2) will belong to $\mathcal{IS}\left(\boldsymbol{l}, \mathcal{I}_{w,h}^{M,N}\right)$ is*

$$P\left[\boldsymbol{l}' \in \mathcal{IS}\left(\boldsymbol{l}, \mathcal{I}_{w,h}^{M,N}\right)\right] = 2\, p_{\boldsymbol{l}}(\boldsymbol{l}')\, \mathfrak{L}(b_l, \theta_l), \tag{6.6}$$

*where $p_{\boldsymbol{l}}(\boldsymbol{l}')$ is given by (6.2).*

*Proof:*

$$\begin{aligned} P\left[\boldsymbol{l}' \in \mathcal{IS}\left(\boldsymbol{l}, \mathcal{I}_{w,h}^{M,N}\right)\right] &= \int_{(b,\theta)\in\mathcal{IS}(\boldsymbol{l})} p_{\boldsymbol{l}}(\boldsymbol{l}')\, db\, d\theta \\ &= p_{\boldsymbol{l}}(\boldsymbol{l}') \int_0^{\pi} \mathfrak{w}_{\boldsymbol{l}}(\theta)\, d\theta \\ &= p_{\boldsymbol{l}}(\boldsymbol{l}')\, \mathfrak{L}(b_l, \theta_l) \int_0^{\pi} |\sin(\theta_l - \theta)|\, d\theta \end{aligned}$$

and the lemma follows. ∎

The following theorem relies on these results, and the NSA approximation, to obtain an expression for the probability density of the Radon transform of a given line $\boldsymbol{l}$.

**Theorem 6.1.** *Consider a line $\boldsymbol{l}$ and denote by $r(\boldsymbol{l}')$ the value of the NSA to the Radon transform of $\boldsymbol{l}$ (Definition 5.1) at a parameterization $\boldsymbol{l}'$ drawn, independently of $\boldsymbol{l}$, according to (6.2). Then, $r(\boldsymbol{l}')$ is distributed according to*

$$\begin{aligned} & P[r(\boldsymbol{l}') = a \,|\, \boldsymbol{l} = (b_l, \theta_l)] \qquad (6.7) \\ &= P\left[\boldsymbol{l}' \in \mathcal{IS}\left(\boldsymbol{l}, \mathcal{I}_{w,h}^{M,N}\right)\right] \left( \frac{1}{\sqrt{1-\left(\frac{w}{a}\right)^2}} \frac{w^2}{a^3} \mathbf{1}_{\{w \le a \le r_{max}\}}(a) \right. \\ &+ \left. \left[1 - \sqrt{1-\left(\frac{w}{a}\right)^2}\right] \delta(a - r_{max}) \right) + \left(1 - P\left[\boldsymbol{l}' \in \mathcal{IS}\left(\boldsymbol{l}, \mathcal{I}_{w,h}^{M,N}\right)\right]\right) \delta(a), \qquad (6.8) \end{aligned}$$

*where $r_{max}$ is given by Lemma 5.5.*

*Proof:* Since $\boldsymbol{l}'$ is drawn independently of $\boldsymbol{l}$, $P[\boldsymbol{l}' = (b,\theta)|\boldsymbol{l}] = P[\boldsymbol{l}' = (b,\theta)]$ and

$$\begin{aligned} & P[r(\boldsymbol{l}') = a \,|\, \boldsymbol{l} = (b_l, \theta_l)] = \\ & \quad \int_{(b,\theta)\in\mathcal{A}(x_{max}, y_{max})} P[r(\boldsymbol{l}') = a \,|\, \boldsymbol{l} = (b_l,\theta_l), \boldsymbol{l}' = (b,\theta)]\, P[\boldsymbol{l}' = (b,\theta)]\, db\, d\theta \\ &= \int_{(b,\theta)\in\mathcal{IS}(\boldsymbol{l})} P[r = a \,|\, \boldsymbol{l}, \boldsymbol{l}']\, p_{\boldsymbol{l}}(\boldsymbol{l}')\, db\, d\theta + \int_{(b,\theta)\notin\mathcal{IS}(\boldsymbol{l})} P[r = a \,|\, \boldsymbol{l}, \boldsymbol{l}']\, p_{\boldsymbol{l}}(\boldsymbol{l}')\, db\, d\theta \qquad (6.9) \end{aligned}$$

where we omit the conditioning parameters $\boldsymbol{l} = (b_l, \theta_l)$ and $\boldsymbol{l}' = (b,\theta)$ for brevity. We start by considering $(b,\theta) \in \mathcal{IS}(\boldsymbol{l})$, in which case it follows from Definition 5.1 that

$$P[r(\boldsymbol{l}') = a \,|\, \boldsymbol{l}, \boldsymbol{l}'] = \delta\left(\min\left[r_{max}, \frac{w}{|\sin(\theta_l - \theta)|}\right] - a\right).$$

Hence,

$$\begin{aligned} & \int_{(b,\theta)\in\mathcal{IS}(\boldsymbol{l})} P[r(\boldsymbol{l}') = a \,|\, \boldsymbol{l}, \boldsymbol{l}']\, p_{\boldsymbol{l}}(\boldsymbol{l}')\, db\, d\theta \\ &= \kappa \int_0^\pi \mathfrak{w}_{\boldsymbol{l}}(\theta)\, \delta\left(\min\left[r_{max}, \frac{w}{|\sin(\theta_l - \theta)|}\right] - a\right) d\theta \\ &= \kappa\, \mathfrak{L}(b_l, \theta_l) \int_0^\pi |\sin(\theta_l - \theta)|\, \delta\left(\min\left[r_{max}, \frac{w}{|\sin(\theta_l - \theta)|}\right] - a\right) d\theta \\ &= \frac{1}{2} P\left[\boldsymbol{l}' \in \mathcal{IS}\left(\boldsymbol{l}, \mathcal{I}_{w,h}^{M,N}\right)\right] \\ &\qquad \int_0^\pi |\sin(\theta_l - \theta)|\, \delta\left(\min\left[r_{max}, \frac{w}{|\sin(\theta_l - \theta)|}\right] - a\right) d\theta. \qquad (6.10) \end{aligned}$$

Assuming, without loss of generality, that $\theta_l > \frac{\pi}{2}$ and exploiting the symmetries of the functions $|\sin(\theta_l - \theta)|$ and $\frac{1}{|\sin(\theta_l - \theta)|}$ (see Figure 6.1), the integral in (6.10) can be rewritten

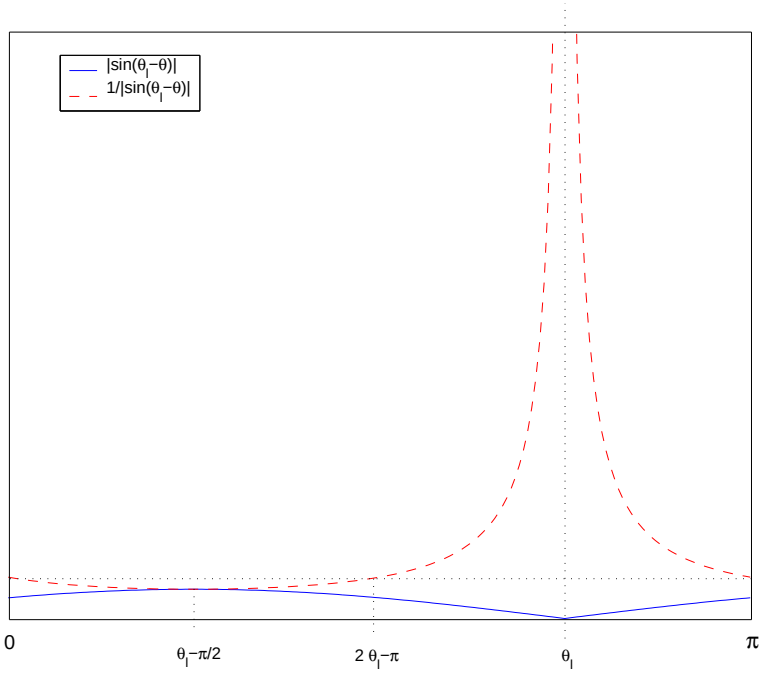


Figure 6.1: $|\sin(\theta_l - \theta)|$ and $\frac{1}{|\sin(\theta_l - \theta)|}$ as functions of $\theta$.

as

$$
\begin{aligned}
&\int_0^{\pi} |\sin(\theta_l - \theta)|\, \delta\left(\min\left[r_{max}, \frac{w}{|\sin(\theta_l - \theta)|}\right] - a\right)\, d\theta \\
&= \int_0^{\theta_l - \arcsin\left(\frac{w}{r_{max}}\right)} |\sin(\theta_l - \theta)|\, \delta\left(\frac{w}{|\sin(\theta_l - \theta)|} - a\right)\, d\theta \\
&+ \int_{\theta_l - \arcsin\left(\frac{w}{r_{max}}\right)}^{\theta_l + \arcsin\left(\frac{w}{r_{max}}\right)} |\sin(\theta_l - \theta)|\, \delta(r_{max} - a)\, d\theta \\
&+ \int_{\theta_l + \arcsin\left(\frac{w}{r_{max}}\right)}^{\pi} |\sin(\theta_l - \theta)|\, \delta\left(\frac{w}{|\sin(\theta_l - \theta)|} - a\right)\, d\theta \\
&= 2\int_{\theta_l - \left(\frac{\pi}{2}\right)}^{2\theta_l - \pi} \sin(\theta_l - \theta)\, \delta\left(\frac{w}{\sin(\theta_l - \theta)} - a\right)\, d\theta \\
&+ 2\int_{2\theta_l - \pi}^{\theta_l - \arcsin\left(\frac{w}{r_{max}}\right)} \sin(\theta_l - \theta)\, \delta\left(\frac{w}{\sin(\theta_l - \theta)} - a\right)\, d\theta \\
&+ 2\int_{\theta_l - \arcsin\left(\frac{w}{r_{max}}\right)}^{\theta_l} \sin(\theta_l - \theta)\, \delta(r_{max} - a)\, d\theta
\end{aligned}
$$

and, using the change of variable $\alpha = \frac{w}{\sin(\theta_l - \theta)}$ $\left(\theta = \theta_l - \arcsin\left(\frac{w}{\alpha}\right), d\theta = \frac{1}{\sqrt{1-\left(\frac{w}{\alpha}\right)^2}} \frac{w}{\alpha^2} d\alpha\right)$,

$$\begin{aligned}
&\int_0^{\pi} |\sin(\theta_l - \theta)|\, \delta\left(\min\left[r_{max}, \frac{w}{|\sin(\theta_l - \theta)|}\right] - a\right) d\theta \\
&= 2\int_w^{\frac{w}{\sin\theta_l}} \frac{w}{\alpha}\, \delta(\alpha - a)\, \frac{1}{\sqrt{1-\left(\frac{w}{\alpha}\right)^2}} \frac{w}{\alpha^2}\, d\alpha + 2\int_{\frac{w}{\sin\theta_l}}^{r_{max}} \frac{w}{\alpha}\, \delta(\alpha - a)\, \frac{1}{\sqrt{1-\left(\frac{w}{\alpha}\right)^2}} \frac{w}{\alpha^2}\, d\alpha \\
&+ 2\,\delta(a - r_{max}) \int_{\theta_l - \arcsin\left(\frac{w}{r_{max}}\right)}^{\theta_l} \sin(\theta_l - \theta)\, d\theta \\
&= 2\frac{w^2}{a^3} \frac{1}{\sqrt{1-\left(\frac{w}{a}\right)^2}} \mathbf{1}_{\left\{w \le a \le \frac{w}{\sin\theta_l}\right\}}(a) + 2\frac{w^2}{a^3} \frac{1}{\sqrt{1-\left(\frac{w}{a}\right)^2}} \mathbf{1}_{\left\{\frac{w}{\sin\theta_l} \le a \le r_{max}\right\}}(a) \\
&+ 2\left[1 - \sqrt{1-\left(\frac{w}{a}\right)^2}\right] \delta(a - r_{max}). \qquad (6.11)
\end{aligned}$$

We next consider the case in which $\boldsymbol{l}' = (b, \theta) \notin \mathcal{IS}(\boldsymbol{l})$. Since, in this case,

$$P[r(\boldsymbol{l}') = a \,|\, \boldsymbol{l}, \boldsymbol{l}' = (b, \theta)] = \delta(a),$$

it follows that

$$\begin{aligned}
\int_{(b,\theta)\notin\mathcal{IS}(\boldsymbol{l})} P[r(\boldsymbol{l}') = a \,|\, \boldsymbol{l}, \boldsymbol{l}']\, P(\boldsymbol{l}')\, db\, d\theta &= \delta(a) \int_{(b,\theta)\notin\mathcal{IS}(\boldsymbol{l})} p_{\boldsymbol{l}}(\boldsymbol{l}')\, db\, d\theta \\
&= \delta(a)\left(1 - \int_{(b,\theta)\in\mathcal{IS}(\boldsymbol{l})} p_{\boldsymbol{l}}(\boldsymbol{l}')\, db\, d\theta\right) \\
&= \delta(a)\left(1 - P\left[\boldsymbol{l}' \in \mathcal{IS}\left(\boldsymbol{l}, \mathcal{I}_{w,h}^{M,N}\right)\right]\right). \qquad (6.12)
\end{aligned}$$

The theorem follows by substituting (6.11) in (6.10), and combining this with (6.12). ∎

The theorem shows that, under the NSA, the probability density function for the amplitude of the Radon transform of a line $\boldsymbol{l}$ is a mixture of three components: two delta functions located at the extreme values ($a = 0$ and $a = r_{max}$) and a component that continuously decays from its maximum at $a = 1$ to its minimum at $a = r_{\max}$. Figure 6.2 presents the fit provided by (6.7) to the actual histogram of the Radon transform of the pixelated line with $\boldsymbol{l} = (0, 0)$ (the delta function located at $a = 0$ is omitted to improve the clarity of the figure). The fit can be considered very good everywhere except in the region $0 < a < 1$. This region corresponds to the values of the Radon transform which are smaller than one, i.e. values associated with the parameterizations of lines whose intersection with the pixelated line $\boldsymbol{l}_p$ is shorter than one pixel. Such lines can only be members of the

partially intersecting set of $\boldsymbol{l}$ and, since the partially intersecting set is not accounted for by the NSA (which accounts for the lines as if they were members of the fully intersecting set), the mismatch was expected. Notice, however, that the probability mass in the region $0 < a < 1$, and therefore in the partially intersecting set, is only a small fraction of the entire probability. This confirms the previous claims that the NSA provides a close approximation to the true Radon transform.

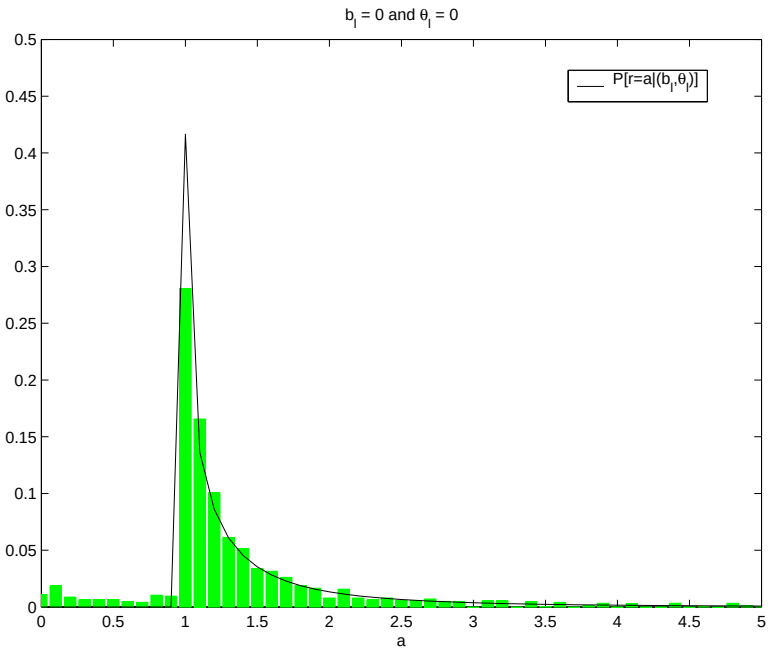


Figure 6.2: Histogram of the Radon transform of the pixelated line with $\boldsymbol{l} = (0, 0)$ and the fit by (6.7). The probability at $a = 0$ is omitted to improved the clarity of the figure.

Theorem 6.1 is interesting in various ways. On one hand, it provides an explicit statistical characterization of the Radon transform of a pixelated line. The study of the statistics of various kernel transformations has been a topic of great activity in the recent past, both in the computer and biological vision literatures (Bell and Sejnowski (1995); Olshausen and Field (1996); Huang and Mumford (1999); Portilla and Simoncelli (2000); Grenander and Srivastava (2001)). It has been postulated that there are universal laws which govern the statistics of these transformations, and a fair amount of experimental evidence has been presented to this effect. To the best of our knowledge, the theorem above and the work of (Grenander and Srivastava (2001)) are the only available proofs of existence of such laws. In addition to this, the theorem is interesting in the sense that it

establishes a basis for the design of sophisticated algorithms. One obvious area of application is the use of (6.7) as a prior for Bayesian inference procedures. While the major goal of the thesis is not the development of these algorithms per se, we will consider in the next section the application of (6.7) to the line detection problem.

## 6.2 Statistics of the Radon transform

There are various statistical quantities of interest to applications of the Radon transform in vision that can be derived from Theorem 6.1. The following corollary provides closed-form expressions for the first- and second-moments of the Radon transform of a pixelated line.

**Corollary 6.1.** *Consider a pixelated line $\boldsymbol{l}$ and denote by $r(\boldsymbol{l}')$ the value of the NSA to the Radon transform of $\boldsymbol{l}$ (Definition 5.1) at a parameterization $\boldsymbol{l}'$ drawn, independently of $\boldsymbol{l}$, according to (6.2). Then, $r(\boldsymbol{l}')$ has the following first- and second-order moments.*

$$\begin{aligned} & E[r(\boldsymbol{l}') \,|\, \boldsymbol{l} = (b_l, \theta_l)] \\ &= 2\,\kappa\,\mathfrak{L}\left( w\left[\frac{\pi}{2} - \arcsin\left(\frac{w}{r_{max}}\right)\right] + r_{max}\left[1 - \sqrt{1 - \left(\frac{w}{r_{max}}\right)^2}\right]\right) \end{aligned} \tag{6.13}$$

$$\begin{aligned} & E[r(\boldsymbol{l}')^2 \,|\, \boldsymbol{l} = (b_l, \theta_l)] \\ &= 2\,\kappa\,\mathfrak{L}\left( w^2 \ln\frac{r_{max} + \sqrt{r_{max}^2 - w^2}}{w} + r_{max}^2\left[1 - \sqrt{1 - \left(\frac{w}{r_{max}}\right)^2}\right]\right) \end{aligned} \tag{6.14}$$

*where $\mathfrak{L}$ is given by (5.2), $\kappa$ by (6.3), and $r_{max}$ by Lemma 5.5.*

*Proof:* The corollary follows from the definition of first- and second-moments

$$\begin{aligned} E[r(\boldsymbol{l}') \,|\, \boldsymbol{l} = (b_l, \theta_l)] &= \int_a a\, P[r(\boldsymbol{l}') = a \,|\, \boldsymbol{l} = (b_l, \theta_l)]\, da \\ E[r(\boldsymbol{l}')^2 \,|\, \boldsymbol{l} = (b_l, \theta_l)] &= \int_a a^2\, P[r(\boldsymbol{l}') = a \,|\, \boldsymbol{l} = (b_l, \theta_l)]\, da. \end{aligned}$$

■

The following corollary builds on these results to determine the probability of the Radon amplitude in the case where it is known that there is one pixelated line in the edge map, but not what its parameters are.

**Corollary 6.2.** *Consider an edge map $\mathcal{EM}[\mathcal{E}](\boldsymbol{x})$ associated with the image $\mathcal{I}_{w,h}^{M,N}$ and denote the number of pixelated lines in it by $T$, i.e.*

$$T = \left|\{\boldsymbol{l}_i \in \mathcal{SL}_{w,h} \,|\, \mathcal{E}(\boldsymbol{l}_i) = 1\}\right|. \tag{6.15}$$

*Then, if $r(\boldsymbol{l}')$ is the value of the NSA to the Radon transform of the edge map at a parameterization $\boldsymbol{l}'$ drawn according to (6.2),*

$$E[r(\boldsymbol{l}') \,|\, T=1] = 2\,\kappa\, E_{\boldsymbol{l}}\left[\mathfrak{L}\left(w\left[\frac{\pi}{2} - \arcsin\left(\frac{w}{r_{max}}\right)\right] + r_{max}\left[1 - \sqrt{1-\left(\frac{w}{r_{max}}\right)^2}\right]\right)\right] \quad (6.16)$$

$$E[r(\boldsymbol{l}')^2 \,|\, T=1] = 2\,\kappa\, E_{\boldsymbol{l}}\left[\mathfrak{L}\left(w^2\,\ln\frac{r_{max}+\sqrt{r_{max}^2-w^2}}{w} + r_{max}^2\left[1 - \sqrt{1-\left(\frac{w}{r_{max}}\right)^2}\right]\right)\right] \quad (6.17)$$

*where $\mathfrak{L}$ is given by (5.2), $\kappa$ by (6.3), $r_{max}$ by Lemma 5.5, and $E_{\boldsymbol{l}}[\cdot]$ is the expectation with respect to $\boldsymbol{l}$.*

*Proof:* Since there is only one line in the edge map, the NSA to the Radon transform of the latter is simply the NSA to the Radon transform of the former. The corollary then follows from Corollary 6.1 by marginalizing over the line parameters,

$$E[r(\boldsymbol{l}')^k \,|\, T=1] = \int E[r(\boldsymbol{l}')^k \,|\, \boldsymbol{l}=(b_l,\theta_l), T=1]\, P[\boldsymbol{l}=(b_l,\theta_l) \,|\, T=1]\, db_l\, d\theta_l \quad (6.18)$$

$$= \int E[r(\boldsymbol{l}')^k \,|\, \boldsymbol{l}=(b_l,\theta_l)]\, p_{\boldsymbol{l}}(b_l,\theta_l)\, db_l\, d\theta_l \quad (6.19)$$

and applying (6.13) and (6.14). ∎

The corollary is interesting in the sense that it shows that, once a measure is assigned to the space of edge indicator functions, the expected value of the Radon transform of an edge map containing a single pixelated line can be predicted in closed-form. This immediately leads to the following theorem.

**Theorem 6.2.** *Consider an edge map $\mathcal{EM}[\mathcal{E}](\boldsymbol{x})$ associated with the image $\mathcal{I}_{w,h}^{M,N}$ and containing $t$ pixelated lines drawn independently according to (6.2). Then, if $r(\boldsymbol{l}')$ is the value of the NSA to the Radon transform of the edge map at a parameterization $\boldsymbol{l}'$ also drawn according to (6.2),*

$$E[r(\boldsymbol{l}') \,|\, T=t] = t\, E[r(\boldsymbol{l}') \,|\, T=1] \quad (6.20)$$

$$var[r(\boldsymbol{l}') \,|\, T=t] = t\,\left\{E[r^2(\boldsymbol{l}') \,|\, T=1] - (E[r(\boldsymbol{l}') \,|\, T=1])^2\right\}, \quad (6.21)$$

*where $var(\cdot)$ means variance and $E[r^k(\boldsymbol{l}') \,|\, T=1], k=1,2$ are as given in Corollary 6.2.*

*Proof:* Consider the parameterization $\boldsymbol{l}'$. Since the edge map of the $t$ lines is the sum of the edge maps originated by each of the lines, by the linearity property of the Radon transform it follows that $r(\boldsymbol{l}') = \sum_{i=1}^{t} r_i(\boldsymbol{l}')$, where $r_i(\boldsymbol{l}')$ is the Radon transform at $\boldsymbol{l}'$ of the $i^{th}$ pixelated line. Hence,

$$\begin{aligned} E[r(\boldsymbol{l}') \,|\, T = t] &= \int E[r(\boldsymbol{l}') \,|\, \boldsymbol{l}_1 = l_1, \ldots, \boldsymbol{l}_t = l_t, T = t]\, p_{\boldsymbol{l}_1,\ldots,\boldsymbol{l}_t|T}(l_1, \ldots, l_t|t)\, dl_1 \ldots dl_t \\ &= \int \sum_i E[r_i(\boldsymbol{l}') \,|\, \boldsymbol{l}_i = l_i] \prod_i p_{\boldsymbol{l}}(l_i)\, dl_1 \ldots dl_t \\ &= \sum_i \int E[r_i(\boldsymbol{l}') \,|\, \boldsymbol{l}_i = l_i]\, p_{\boldsymbol{l}}(l_i)\, dl_i \\ &= t\, E[r(\boldsymbol{l}') \,|\, T = 1]. \end{aligned}$$

The derivation of the expression for the variance is similar. Because the $t$ lines are drawn independently, the $r_i(\boldsymbol{l}')$ are independent random variables and, therefore, the variance of the sum is equal to the sum of the variances. Marginalizing over the $\boldsymbol{l}_i$ as above leads to

$$var[r(\boldsymbol{l}') \,|\, T = t] = t\, var[r(\boldsymbol{l}') \,|\, T = 1]$$

and (6.21) follows from the well know relationship between the variance and the first- and second-order moments of a random variable $var(r) = E(r^2) - [E(r)]^2$. ∎

From the point of view of applications, the significance of this theorem is that, once a measure is assigned to the space of line indicator functions, the terms $E[r^k(\boldsymbol{l}') \,|\, T = 1], k = 1, 2$ are completely determined by the image size - which determines $\mathfrak{L}$ through (5.2), $r_{max}$ through Lemma 5.5, and $\kappa$ through (6.3). Hence, given the measure and the image dimensions it is possible to pre-compute $E[r^k(\boldsymbol{l}') \,|\, T = 1], k = 1, 2$, and therefore $E[r(\boldsymbol{l}') \,|\, T = t]$ and $var[r(\boldsymbol{l}') \,|\, T = t]$ for all values of $t$ of interest. Indeed, this operation only has to be performed once, independently of whether the Radon transform is applied to the entire image or to local neighborhoods, or even independently of the pixel intensities of the image. Table 6.1 presents the values of the coefficients $E[r(\boldsymbol{l}') \,|\, T = 1]$ and $var[r(\boldsymbol{l}') \,|\, T = 1]$ for an example set of neighborhood sizes ranging from $20 \times 20$ to $100 \times 100$. Notice that the values of the coefficients are approximately constant and independent of the image size. This suggests that a good strategy to determine the number of lines $t$ in a given edge map would be to obtain an empirical estimate of the mean and variance of its Radon transform and select the $t$ that leads to the closest values of $E[r(\boldsymbol{l}') \,|\, T = t]$ and $var[r(\boldsymbol{l}') \,|\, T = t]$. We next formalize this intuition.

| Region Size | $E[r(\boldsymbol{l}') \mid T = 1]$ | $var[r(\boldsymbol{l}') \mid T = 1]$ |
|---|---|---|
| $20 \times 20$ | 0.6201 | 0.0042 |
| $40 \times 40$ | 0.6180 | 0.0052 |
| $60 \times 60$ | 0.6173 | 0.0058 |
| $80 \times 80$ | 0.6175 | 0.0062 |
| $100 \times 100$ | 0.6175 | 0.0066 |

Table 6.1: Coefficients of (6.20) and (6.21) for various region sizes.

## 6.3 Determining the number of lines

One possible way to estimate the mean and variance of a random variable is to obtain a sample of observations and compute its sample mean.

**Definition 6.3.** If $\boldsymbol{x}$ is a real valued random variable and $x_1, x_2, \ldots x_n$ a sample of observations of $\boldsymbol{x}$, the sample mean $< x >$ is

$$< x >= \frac{1}{n} \sum_{j=1}^{n} x_j. \tag{6.22}$$

It is well known that the sample mean satisfies the following properties.

**Lemma 6.4.** *Let $< x >$ be the sample mean of a sample of observations from a random variable $\boldsymbol{x}$. Then*

$$E[< x >] = E[\boldsymbol{x}]. \tag{6.23}$$

*Furthermore, if the observations are drawn independently,*

$$var(< x >) = \frac{1}{n} var(\boldsymbol{x}). \tag{6.24}$$

*Finally, for large $n$, the probability density function of $< x >$ converges to a Gaussian distribution of mean $E[< x >]$ and variance $var(< x >)$.*

*Proof:* The first two results are straightforward, the third is known as the central limit theorem. See any text on elementary probability, e.g. (DRAKE (1987); PAPOULIS (1991)), for proofs. ∎

Since the Radon transform of a pixelated edge map is a sample of observations from $r(\boldsymbol{l}')$, this lemma suggests the following approximation to its probability density.

**Definition 6.4.** The *asymptotic independent sample approximation* (AISA) to the probability density of the NSA to the Radon transform $r(\boldsymbol{l}')$ of a pixelated edge map containing $t$ lines is

$$P(< r > | T = t) = \frac{PQ}{\sqrt{2\pi}\, var[r(\boldsymbol{l}')|T=t]} \exp\left\{ -\frac{PQ}{2\, var[r(\boldsymbol{l}')|T=t]} \left(< r > - E[r(\boldsymbol{l}') \mid T = t]\right)^2 \right\} \quad (6.25)$$

where $PQ$ is the cardinality of the sample (number of parameterizations on the grid $\mathcal{L}^{PQ}_{b_s,\theta_s}$ used to compute the Radon transform).

There are two reasons why (6.25) is an approximation. The first is the assumption that the central limit theorem holds. This is a reasonable assumption since, even relatively small image neighborhoods by image analysis standards (e.g. $M, N = 40$), will generate a large number of observations (1600). The second is the assumption that the observations of $r(\boldsymbol{l}')$ are drawn independently, inherent to (6.24). Notice that while the parameterizations $\boldsymbol{l}'$ are drawn independently, the values of the Radon transform at those parameterizations are not, since each pixelated line contributes to all of them. Due to this, and unlike the estimate of the mean, the estimate of the variance given by (6.25) is usually incorrect. Nevertheless, we will see that the AISA can lead to effective algorithms for determining the number of lines in the edge map.

We start by proposing an algorithm based on the principles of decision theory. It is well known (BERGER (1985) that, given the observation of a random variable $A$, the minimum probability of error estimate of a random variable $B$ is the *maximum a posteriori* (MAP) estimate

$$b_{MAP} = \arg\max_b P(B = b | A = a) \quad (6.26)$$

$$= \arg\max_b P(A = a | B = b)\, P(B = b). \quad (6.27)$$

The density $P(B = b)$ is referred to as the *prior density*, and $P(A = a|B = b)$ as the *conditional likelihood* function. In the line detection context, the variable to estimate is the number of lines $T$, and the observed random variable the sample mean of the Radon transform of the pixelated edge map. The AISA provides an approximation to the (unknown) conditional likelihood function of the latter given the former, enabling the estimation of the number of lines through the following algorithm.

**Algorithm 6.1.** *Given an edge map $\mathcal{EM}[\mathcal{E}](\boldsymbol{x})$, a parameter lattice $\mathcal{L}^{P,Q}_{b_s,\theta_s}$, and a prior probability for the number of pixelated lines $P(T = t)$, perform the following steps to estimate the number of pixelated lines that it contains:*

1. *compute the Radon transform* $\mathcal{R}\{\mathcal{EM}[\mathcal{E}](\boldsymbol{x})\}(b_i,\theta_i), \forall (b_i,\theta_i) \in \mathcal{L}^{P,Q}_{b_s,\theta_s}$;

2. *compute the sample mean* $< \mathcal{R}\{\mathcal{EM}[\mathcal{E}]\}(b_i,\theta_i) >$;

3. *compute the maximum a posteriori probability estimate for the number of lines under the AISA*

$$t_{MAP} = \arg\max_t P\left[< \mathcal{R}\{\mathcal{EM}[\mathcal{E}]\}(b_i,\theta_i) > \mid T = t\right] P(T = t), \tag{6.28}$$

*where* $P\left[< \mathcal{R}\{\mathcal{EM}[\mathcal{E}]\}(b_i,\theta_i) > \mid T = t\right]$ *is obtained by using* $< \mathcal{R}\{\mathcal{EM}[\mathcal{E}]\}(b_i,\theta_i) >$ *as* $< r >$ *in (6.25).*

Figure 6.3 presents the Gaussian densities described by (6.25) for a region size of $40 \times 40$ and $t \in \{1,\ldots,10\}$. Notice that these densities are clearly separated, indicating that the probability of error of the MAP decisions should be very small. However, due to the

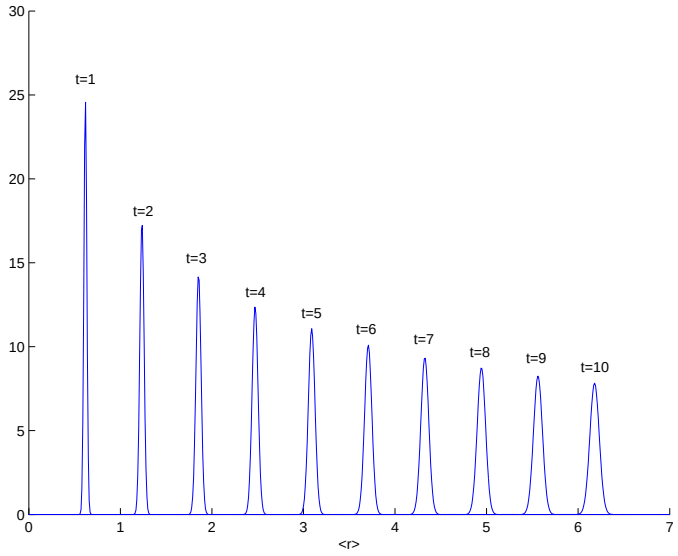


Figure 6.3: Gaussian densities characterizing the AISA to the likelihood of the sample mean of the Radon transform of a $40 \times 40$ pixelated edge map, given the number of pixelated lines.

independence assumption inherent to the AISA, the true variances can be much larger than those suggested by the figure and the probability of error could therefore be much larger as well. In order to evaluate how this problem may affect the accuracy of Algorithm 6.1, we conducted the following Monte Carlo experiment:

- one thousand trial edge maps containing $t$ pixelated lines were independently drawn according to (6.2);
- the estimate $t_{MAP}$ was computed for each edge map, according to Algorithm 6.1, and the number of trials in which $t_{MAP}$ was different than $t$ was recorded.

The experiment was repeated for images sizes ranging from $40 \times 40$ to $100 \times 100$ and $t$ ranging from 1 to 5. Table 6.2 presents the percentage of the estimates that were wrong for each image size. Clearly, the possible variance mismatch does not seem to be a reason for much concern. In the image sizes and number of lines considered, the error rarely exceeded 1%, suggesting that the AISA is a good model for determining the number of pixelated lines in a given edge map.

| Region Size | 1 line | 2 lines | 3 lines | 4 lines | 5 lines |
|---|---|---|---|---|---|
| $40 \times 40$ | 0% | 0.4% | 0.6% | 2.2% | 6.3% |
| $60 \times 60$ | 0% | 0% | 0.1% | 0.3% | 0.4% |
| $80 \times 80$ | 0% | 0% | 0.1% | 0.4% | 0.2% |
| $100 \times 100$ | 0% | 0% | 0.2% | 0.1% | 0% |

Table 6.2: Error rate for the estimate of the number of lines for the Monte Carlo experiment described in the text.

## 6.4 Line detection examples

The main limitation of the line detection examples of chapter 5 was the absence of localization. While satisfactory at the whole image level, the strategy of pre-defining the number of lines does not really generalize to the case in which the Radon transform is computed over spatially localized neighborhoods. The problem is that different neighborhood will typically contain different numbers of lines and the estimate of this number must, therefore, be adaptive. This is impossible when the number of lines is pre-set, in which case it is impossible to recover the image lines with any degree of confidence in what regards to their spatial localization (e.g. start- and end-points).

The statistical characterization developed in this chapter makes it possible to find the optimal (in the minimum probability of error sense) estimate for the number of lines, therefore enabling the computation of the Radon transform over localized neighborhoods. In this section, we finalize the chapter with some examples of spatially localized line detection.

A collection of natural images containing lines was assembled, each image decomposed into a set of local neighborhoods, the number of lines in each neighborhood estimated with Algorithm 6.1 and the line parameters recovered with Algorithm 5.5. Figure 6.4 presents the images previously analyzed in Chapter 5, and the corresponding estimate of the number of lines in each image region (activity map). Figure 6.5 presents the recovered lines. We emphasize that these results are the output of the straightforward combination of the two algorithms. No post-processing steps were included to try to improve in any way the line detection results. Comparing with Figure 5.18, it is clear that the spatial localization of the recovered lines is now significantly higher. Figures 6.6 to 6.8 present a set of additional images of indoor and outdoor scenes, the associated edge maps, and the lines recovered with the combination of Algorithms 6.1 and 5.5.

From these examples it can be concluded that the lines that exist in the edge map tend to be recovered with fairly good accuracy. This is not to say that there are no problems. In particular, there are two major sources of error: 1) textured areas that lead to a significant number of false positives, and 2) edge detection omissions that lead to missed line segments. Finally, all the analysis is limited by the fact that, for each image, all neighborhoods are of the same size, and the size is currently pre-specified (to roughly $\frac{1}{10}$ of the image height). The solution of these problems will require additional modules, e.g. a texture detector that can automatically disable the line detection module in textured regions, and an algorithm to estimate the optimal neighborhood size at each image location. Finally, these results also raise the question of whether assuming the existence of a reliable edge map is feasible in practice. All these questions remain open for future work.

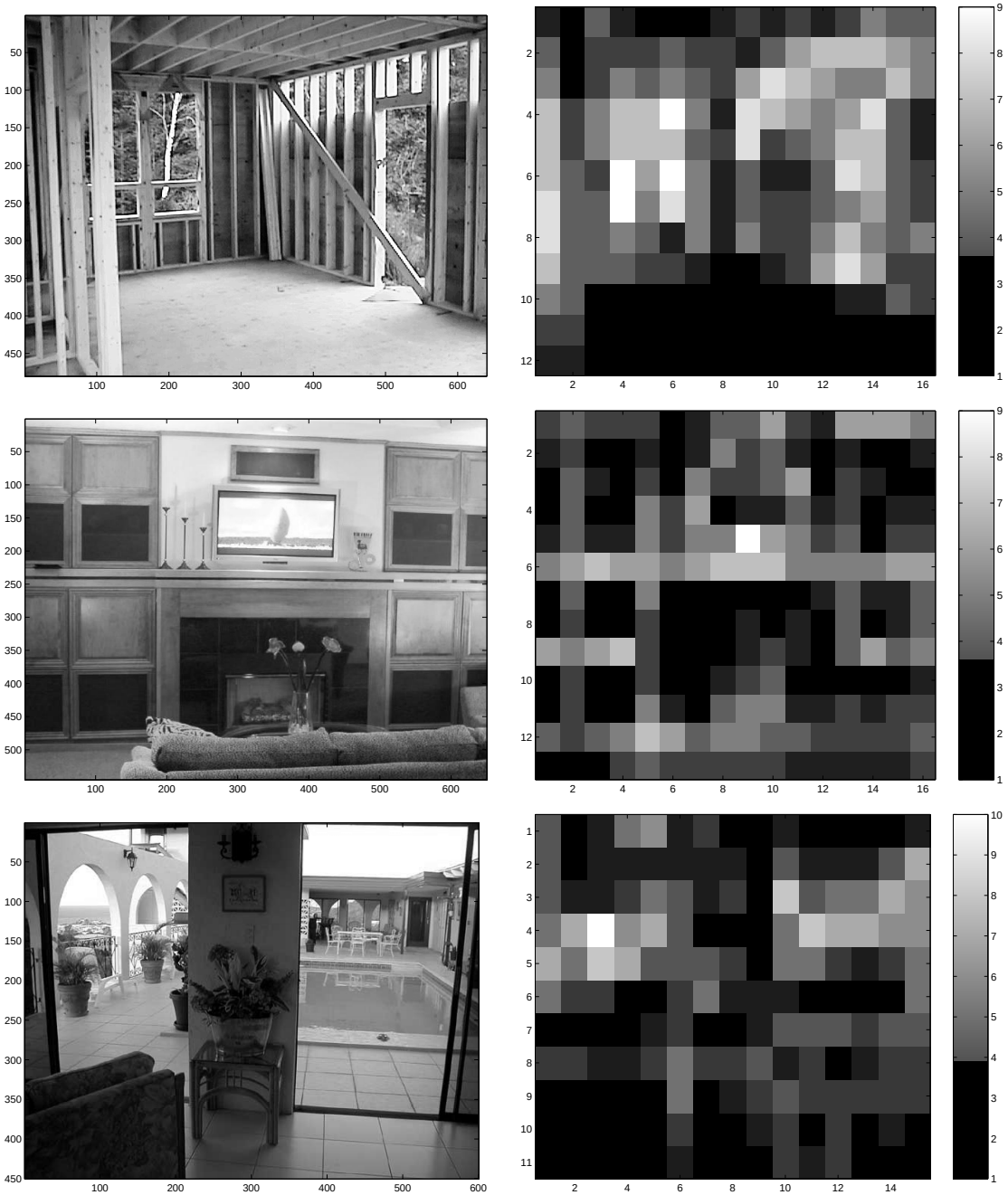

Figure 6.4: Left: images previously analyzed in Figure 5.18. Right: associated activity maps.

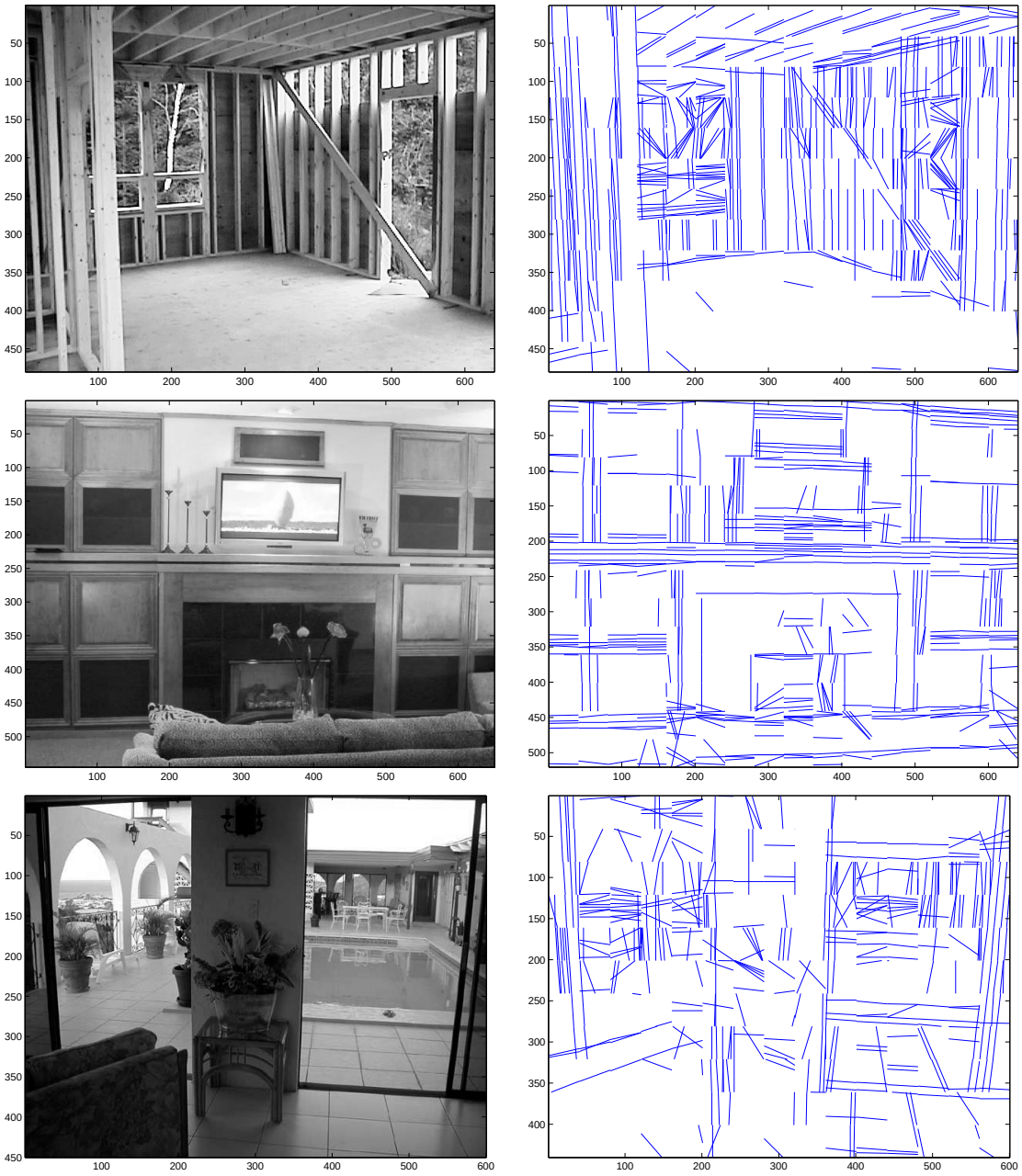

Figure 6.5: Left: images previously analyzed in Figure 5.18. Right: lines recovered with the combination of Algorithms 5.5 and 6.1.

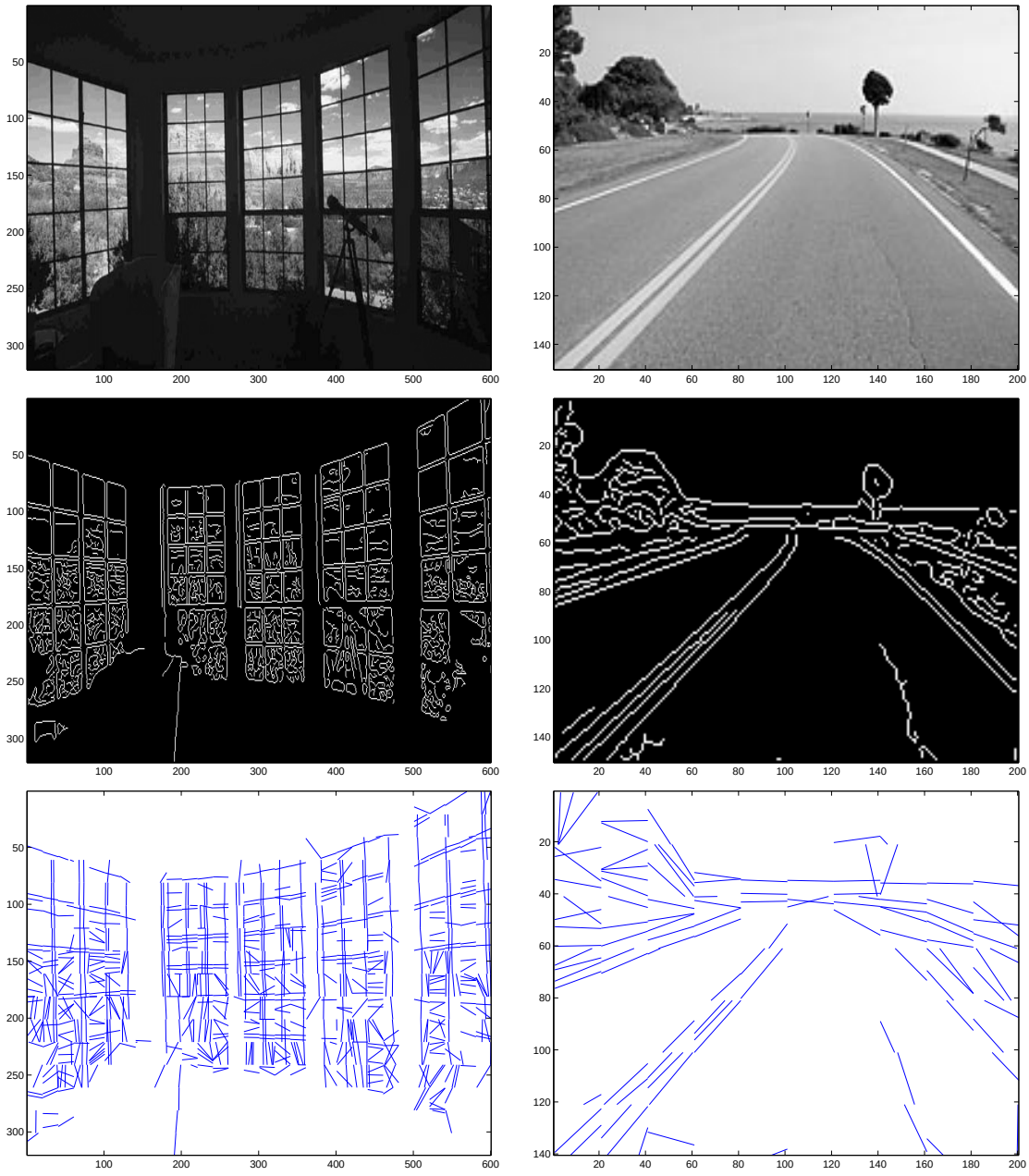

Figure 6.6: Two images (top), associated edge maps (middle row), and recovered lines (bottom).

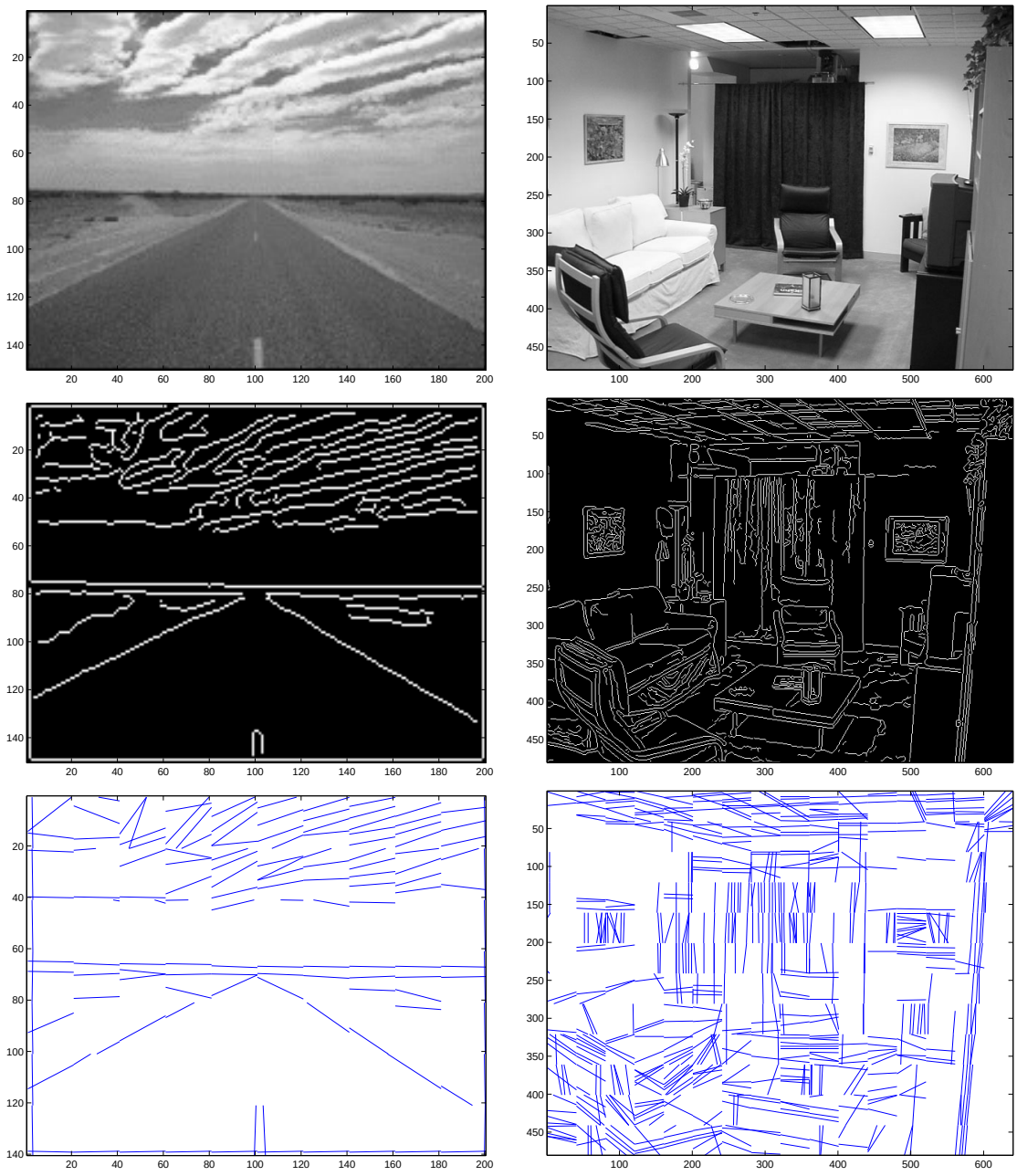

Figure 6.7: Two images (top), associated edge maps (middle row), and recovered lines (bottom).

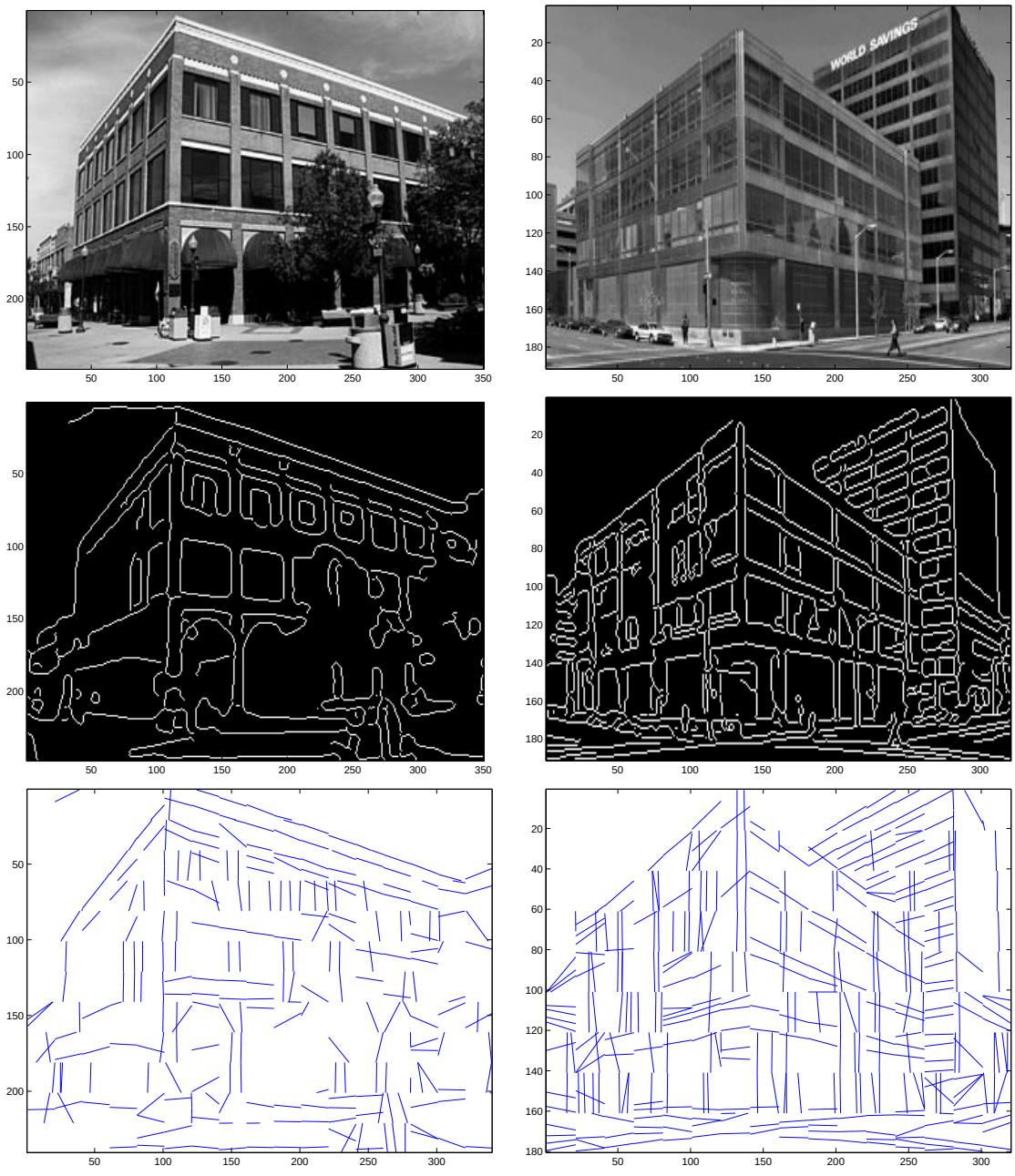


Figure 6.8: Two images (top), associated edge maps (middle row), and recovered lines (bottom).

# Chapter 7

# Conclusions

In this thesis, we have presented a detailed characterization of the Radon transform of pixelated functions. We believe that several contributions were derived that shed non-trivial insights on how the Radon transform of the ideal line compares with that of a pixelated approximation. These include: 1) a closed-form expression for the Radon transform of the pixelated line, 2) a precise understanding of how the various features of the pixelated line (bounded support, non-zero width, and pixelization) affect its Radon transform, 3) a parametric model for the latter that is quite easy to manipulate both analytically and computationally, 4) a characterization of various statistics of the Radon transform of the pixelated line, and 5) a proof of existence of a statistical law that governs the value of the Radon transform of probabilistically specified pixelated lines.

In the process of deriving these main contributions, various other interesting insights were obtained, namely 1) the decomposition of the range function of the Radon transform into its support set (the intersecting set of the pixelated line) and amplitude, 2) the realization that while the amplitude is significantly affected by pixelization the support set is basically unaltered by it, 3) the connection between several variations in the standard thresholding procedure for line detection and a taxonomy of models that approximate the Radon transform of the pixelated line with different levels of accuracy, and 4) a clear understanding of when the assumption that a line is ideal and not pixelated is acceptable.

The main theoretical contributions were also shown to be of practical impact by 1) exposing fundamental limitations of commonly used procedures, such as the detection of geometric structures by thresholding, and 2) establishing a principled basis for the derivation of new algorithms for various components of the line detection problem. These included an optimal (in the minimum probability of error sense) procedure for automatically

determining the number of lines in an image, and an analysis-by-synthesis algorithm for determining the parameters of those lines, that was shown to be significantly superior to currently used methods. The combination of the two algorithms enables spatially localized line detection without degradation of the detection accuracy, something that was shown not to be possible under thresholding strategies.

While this is a non-trivial set of insights and algorithmic contributions, it is really only a first step toward a complete understanding of the impact of pixelization on the Radon transform. In fact, there are many ways in which this work could be extended. In terms of deriving models that are suitable for line detection, it would be interesting to extend what was done for the line to other geometric objects. In principle, there is no reason why the analysis could not be extended to pixelated circles, rectangles, and so forth, but it remains to be determined what would be the equivalent expressions for quantities such as the intersecting set, the decay of the amplitude of their Radon transform, or statistical quantities such as the histogram and second-order moments.

Even for the pixelated line itself, there are various extensions that warrant further exploration. These include the extension of all statistical results to the case where more realistic measures are imposed on the space of edge indicator functions. While relaxing the assumption of a uniform prior distribution should not be too difficult (e.g. to account for images with a dominant orientation), relaxing the independence assumption is likely to be a source of greater difficulty. It would nevertheless be interesting to explore priors that can account for the known geometric structure of most scenes that contain lines (e.g. priors that favor parallelism) or even encode some well known properties of the human visual system, e.g. the so-called Gestalt principles of perceptual organization (PALMER (1999)).

Another interesting source of open questions is the issue of extending the results presented to non-binary pixelated functions. While an exact expression was derived for the Radon transform of any pixelated function, this expression suffers from the same limitation as the equivalent one for the pixelated line: it is quite complex. Even in the context of edge detection, it would be interesting to consider models for the line that apply directly to the image intensities. This would bypass the need for an edge detection step, that was shown to be the source of various problems.

In addition to this, and still in the context of vision applications and the edge detection problem, this work leaves various other questions unanswered. An issue that will require further investigation is that of how to automatically determine the optimal granularity for the Radon transform. It is likely that better performance can be achieved by adapting the

size of the local neighborhood to the local image statistics. This, however, will require some optimality criterion relating the neighborhood size and the accuracy of the line detection. At this point, it is not clear what this criteria might be. Another open issue is that of integrating the local estimates that are currently obtained into a set of coherent global line estimates. Ideally, this integration should be driven from line estimates derived at multiple image resolutions and neighborhood sizes. Once again, solving this problem will imply the derivation of probabilistic models for configurations of line segments.

# Bibliography


Bell, A., and Sejnowski, T. (1995). An information maximization approach to blind separation and blind deconvolution. *Neural Computation*, 7:1129–1159.

Berger, J. (1985). *Statistical decision theory and Bayesian analysis.* Springer-Verlag.

A. Blake and A. Yuille, editors (1992). *Active vision.* MIT Press.

Canny, J. (1986). A computational approach to edge detection. *IEEE Trans. on Pattern Analysis and Machine Intelligence*, 8:679–698.

Deans, S. (1983). *The Radon transform and some of its applications.* John Wiley.

Drake, A. (1987). *Fundamentals of applied probability theory.* McGraw-Hill.

Duda, R., and Hart, P. (1973). *Pattern classification and scene analysis.* John Wiley.

Faugeras, O. (1993). *Three-dimensional computer vision: a geometric viewpoint.* MIT Press.

Grenander, U., and Srivastava, A. (2001). Probability models for clutter in natural images. *IEEE Trans. on Pattern Analysis and Machine Intelligence*, 4:424–429.

Hallinam, P., Gordon, G., Yuille, A., and Mumford, D. (1999). *Two- and three-dimensional pattterns of faces.* A K Peters.

Hartley, R., and Zisserman, A. (2000). *Multiple view geometry in computer vision.* Cambridge University Press.

Heeger, D., and Bergen, J. (1995). Pyramid Based Texture Analysis/Synthesis. *Computer Graphics Proceedings*, pages 229–238.

Helgason, S. (1999). *The Radon transform.* Progress in mathematics. Birkhäuser Boston, second edition.

Hough, P. (1962). *Methods and means for recognizing complex patterns.* U.S. Patent 3 069 654.

Huang, J., and Mumford, D. (1999). Statistics of natural images and models. *IEEE Intl. Conf. on Computer Vision and Pattern Recognition*, pages 541–547.

ILLINGWORTH, J., and KITTLER, J. (1988). A survey of the Hough transform. *Computer Vision, Graphics, and Image Processing*, 44:87–116.

JAIN, A. K. (1989). *Fundamentals of digital image processing.* Prentice Hall.

KUMAR, R., ANANDAN, P., IRANI, M., BERGEN, J., and HANNA, K. (1995). Representation of scenes from collections of images. *IEEE Workshop on Representations of Visual Scenes.*

OLSHAUSEN, B., and FIELD, D. (1996). Emergence of simple-cell receptive field properties by learning a sparse code for natural images. *Nature*, 381:607–609.

PALMER, S. (1999). *Vision science: photons to phenomenology.* MIT Press.

PAPOULIS, A. (1991). *Probability, random variables, and stochastic processes.* McGraw-Hill.

PORTILLA, J., and SIMONCELLI, E. (2000). A parametric texture model based on joint statistics of complex wavelet coefficients. *Intl. Journal of Computer Vision*, 40:49–71.

RADON, J. (1917). Über die Bestimmung von Funktionen durch ihre Integralwerte längs gewisser Mannigfaltigkeiten (On the determination of functions from their integrals along certain manifolds). *Mathematish-Physikalishe Klasse*, 69:262–277. (English translation of the paper in DEANS (1983)).

SMEULDERS, A., WORRING, M., SANTINI, S., GUPTA, A., and JAIN, R. (2000). Content-based image retrieval: the end of the early years. *IEEE Trans. on Pattern Analysis and Machine Intelligence*, 22:1349–1380.

SOATTO, S., and BROCKETT, R. (1998). Optimal and suboptimal structure from motion. *IEEE Intl. Conf. on Computer Vision and Pattern Recognition*, pages 282–288.

TOMASI, C., and KANADE, T. (1992). Shape and motion from image streams under orthography - a factorization method. *International Journal in Computer Vision*, 9: 137–154.

ULLMAN, S. (2000). *High-level vision: object recognition and visual cognition.* MIT Press.

VAN TREES, H. (1968). *Detection, estimation, and modulation theory.* John Wiley.